Technische Universität München
TUM School of Natural Sciences

Linear and Nonlinear Chiroptical Spectroscopy with the Aim of Asymmetric Heterogeneous Catalysis

Natalie A. Fehn

Vollständiger Abdruck der von der TUM School of Natural Sciences der Technischen Universität München zur Erlangung des akademischen Grades einer **Doktorin der Naturwissenschaften** (Dr. rer. nat.) genehmigten Dissertation.

Vorsitz:	Prof. Dr. Dominik Bucher
Prüfer*innen der Dissertation:	1. Priv.-Doz. Dr. Aras Kartouzian
	2. apl. Prof. Dr. Hristo Iglev

Die Dissertation wurde am 23.03.2023 bei der Technischen Universiät München eingereicht und durch die TUM School of Natural Sciences am 17.04.2023 angenommen.

Abstract

Asymmetric heterogeneous catalysis is a concept that combines enantioselectivity with the advantages of heterogeneous catalysis. The majority of research on this topic concentrates on fixating an established asymmetric homogeneous catalyst onto a suitable surface. However, often a loss in activity and enantioselectivity of the catalyst is witnessed, caused by the fixation. In contrast, we aim for an alternative approach that includes the chirality transfer from a chiral inducer onto an established heterogeneous catalyst. For the study of such materials, the induced circular dichroism (ICD) between the two entities is of special interest. Therefore, both a suitable chiroptical method with high sensitivity to chirality and small changes of the catalyst structure, as well as an adequate model catalyst system with pronounced ICD are required. In this thesis, both aspects of spectroscopy for asymmetric heterogeneous catalysis are covered. The non-linear method of second harmonic generation circular dichroism (SHG-CD) is validated in terms of sensitivity to structural changes and chirality detection for the case of supported gold nanoparticles (Au NPs), and molecular thin films of Cysteine and Binol. Afterwards, the interactions between supported Au NPs with catalytic relevance and potential chiral inducers Cysteine and Binol are studied with special attention to ICD. Finally, an ICD between supported Au NPs and molecular adsorbates is unambiguously observed and analysed with SHG-CD, for the first time to the best of our knowledge. Additionally, the knowledge on ICD effects is complemented by investigations in a plethora of relevant systems such as transition metal complexes, crystallised molecular layers, gel structures with dye intercalation, and thin film perovskites.

Kurzzusammenfassung

Die asymmetrische heterogene Katalyse verbindet die Vorteile von enantioselektiven Reaktionen mit denen der heterogenen Katalyse. Der meistgebrauchte Ansatz zur Herstellung eines solchen Materials inkludiert die Fixierung eines bereits etablierten asymmetrischen homogenen Katalysators auf einer geeigneten Oberfläche, obwohl dies meist zu einer Reduktion in Enantioselektivität und Aktivität des Katalysators führt. Wir folgen einem alternativen Weg, der auf Chiralitätstransfer zwischen einer chiralitätsinduzierenden Entität und einem heterogenen Katalysator beruht. Für die Untersuchung dieses Effekts bedarf es sowohl einer leistungsstarken chiroptischen Spektroskopiemethode mit genügender Sensibilität auf Chiralität und strukturelle Details des Katalysators als auch passende Modellsysteme mit ausgeprägtem induziertem Zirkulardichroismus (ICD) und katalytischer Relevanz. Diese beiden Aspekte der Spektroskopie für asymmetrische heterogene Katalyse werden im Rahmen der vorliegenden Dissertationsarbeit behandelt. Zuerst wird die Eignung der nicht-linearen Methode der Frequenzverdopplung mit Zirkulardichroismus (SHG-CD) für dieses Unterfangen anhand von geträgerten Goldnanoteilchen (Au NPs) und molekularen Dünnfilmen aus Cystein und Binol bestätigt. Daraufhin werden die Wechselwirkungen zwischen geträgerten Au NPs mit den chiralitätsinduzierenden Molekülen Cystein und Binol untersucht, mit besonderem Augenmerk auf ICD. Dabei wird ein ICD zwischen den geträgerten Au NPs und chiralen Adsorbaten beobachtet, der erstmals eindeutig durch SHG-CD nachgewiesen werden konnte. Darüber hinaus werden weitere Einblicke in den ICD-Effekt durch Untersuchungen an diversen anderen Systemen mit Relevanz gewonnen: von Übergangsmetallkomplexen und Gel-Farbstoff-Strukturen über kristalline Molekülfilme hin zu Dünnfilm-Perovskiten.

Acknowledgements

First, I thank Aras Kartouzian for his guidance during the past years that was always based on trust and patience. He gave me large freedom to choose and explore our scientific projects on my own while always being ready for discussions and suggestions at the same time. I am deeply grateful for the inspiration and benefit I gained from his deep knowledge and broad field of vision. Also, I would like to express my gratitude to Ueli Heiz for accepting me into the chair and his guidance within the group. The time I spent at his chair was really enjoyable and I was able to grow a lot, both professionally and on a personal level, because of the scientific and cordial working climate he created.

In the first few weeks of my doctorate, my predecessors Matthias Jakob and Alexander von Weber gave me a thorough crash course of everything related to our experimental setup. I am very grateful for their efforts that helped me ease into our sophisticated research. Later-on, Viktoria Brandt and Kevin Liang joined our subgroup. I am grateful for the new perspectives the two brought, and also for the friendship that developed during our time together.

Of course, my work would not have been possible without the contributions of our collaborators. Especially, I am grateful to Melanie Strauss and Klaus Köhler that work just across the hallway; Markus Heindl and Shangpu Liu of the group of Felix Deschler as well as Florian Ristow and Hristo Iglev from across the street; Matthias Golibrzuch working in the group of Markus Becherer at the other side of Garching campus; as well as Ehsan Vahidzadeh and Harshitha Rajashekhar from the group of Karthik Shankar across the Atlantic ocean.

Similarly, the students I supervised in our labs each added to our research in their own ways during their research internships and Bachelor's and Master's theses. Thank you, Heike Plendl, Maria Lanzinger, Maryke Kouyate, Sofia Beliakova, Viktoria Brandt, Victor Chen, Max Beer, and Aaron Oechsle.

Contents

1. Introduction

Many fine and agrochemicals, aromas, but also drugs and pharmaceuticals are chiral meaning that there exist two enantiomers of the same molecule, whose structure represent an image–mirror image pair and which discriminate only by interaction with other chiral entities. While one enantiomer provides the desired properties such as being the remedy to an illness, the other brings no effect or may even cause harmful consequences. Currently, those compounds are produced industrially often as the racemic mixture, followed by enantioseparation. Since only one enantiomer is favoured in utilisation, accordingly there lies great potential of saving resources like starting materials, energy, and time with enantioselective or enantiopure production. Combined with heterogeneous catalysis, this brings additional advantages such as reusability of the catalyst, easier separation from products, and more.[1,2]

For the creation of an asymmetric heterogeneous catalyst, there are two main strategies discussed:[3] 1) fixation of a homogeneous catalyst, often in the form of a chiral transition metal complex, onto a suitable surface. This approach has been followed quite intensely due to the performance of the complexes as homogeneous catalysts. However, the fixated catalysts often show reduced (enantio-)selectivity and catalytic activity in comparison to their homogeneous counterparts. Furthermore, some systems are prone to the catalyst leaching off the surface, depending on the fixation protocol.[2] 2) The other approach is the asymmetrisation of a heterogeneous catalyst by interaction with a chiral inducer, such as chiral molecules staying out of the reaction or chiral support materials. While being the less pursued strategy, nevertheless there exist examples showing enantioselectivity and even improved catalytic activity.[4] Publications from the 2000s may give a broad overview,[1,2] while the developments

and endeavours on this topic with emphasis on the approach of chiral induction have been summarised more recently.[3]

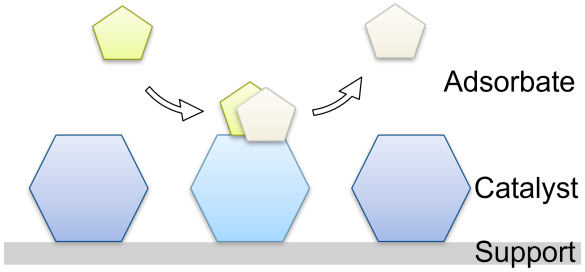

Figure 1.1.: Aspects of spectroscopy for asymmetric heterogeneous catalysis including the catalyst before and after reaction and in contact with adsorbates such as reactants and products.

Within the scope of this thesis, schematically presented in fig. 1.1, model catalysts such as supported gold nanostructures were characterised by means of linear and non-linear chiroptical spectroscopic methods, for consecutive use as asymmetric heterogeneous catalysts. While the bare nanostructures here may represent the catalyst before or after the reaction, the nanostructures in contact with chiral adsorbates can be seen as the asymmetrised catalyst during the reaction in this picture. Not only do we need to search for adequate model catalyst systems with efficient chirality induction, but the selection of appropriate chiral characterisation methods with paramount sensitivity to structural details is important as well. Thus, especially the suitability of the non-linear method second harmonic generation circular dichroism spectroscopy is highlighted for examinations of such model catalysts and related systems. The scope also includes possible support materials and adsorptive molecules in the form of molecular thin films, that may be employed for efficient asymmetrisation of the model catalyst materials or may represent an adsorbed reactant. Since the effect and origin of induced circular dichroism in general remain unknown for many compounds, other contributions to the knowledge on interactions between chiral and achiral entities in a variety of systems are presented as well, including chiral transition metal complexes, laser dyes in chiral gel structures, crystallisation and desorption of chiral molecular thin films, and crystalline luminescent chiral perovskite thin films.

2. Background

For the creation of a heterogeneous asymmetric model catalyst, we intend to use plasmonic nanoparticles as the carrier of catalytic activity in combination with a chiral inducer that is responsible for the introduction of optical activity into the system. Thus, relevant aspects on plasmonic nanoparticles and induced circular dichroism are summarised in this chapter. Afterwards, a concise introduction to the spectroscopic methods of circular dichroism and second harmonic generation circular dichroism is given.

2.1. Plasmonic Metal Nanoparticles

Particles with a size in the nanoscale are generally referred to as nanoparticles (NPs). In comparison to bulk materials, a significant fraction of atoms are located at the surface, so that physical and chemical properties such as melting point, reactivity, and crystal parameters depend linearly on the particle size.[5] Even smaller particles of 1 nm and below consist of very few atoms only. Since most of the atoms of such a small cluster are located at the surface, one observes drastic property changes with cluster size or atom count and arrangement, accordingly.[6,7]

One intriguing aspect of noble metal NPs such as Au, Ag, and Cu is their interesting optical properties which are heavily influenced by localised surface plasmon resonances (LSPRs). A plasmon is the propagating, collective oscillation of the Drude free electron cloud relative to the fixed position of their metal ions. Its resonance frequency is described by the plasma

frequency ω_p according to[8]

$$\omega_p = \sqrt{\frac{e^2 \cdot n_e}{\varepsilon_0 \cdot m_e}} \tag{2.1}$$

with the elementary charge e, the number of charge carriers n_e, the vacuum permittivity ε_0, and the effective electron mass m_e. At the interface between the metal and an dielectric, the surface plasmon resonance is modified with the dielectric constant of the surrounding medium ε_m as in[8]

$$\omega_{SPR} = \frac{\omega_p}{\sqrt{1+\varepsilon_m}}. \tag{2.2}$$

Through spacial confinement within the NP, the surface plasmon becomes a non-propagating (localised) excitation (LSPR).In dependence on the polarisability of the material, this resonance absorption is accompanied by resonance Mie scattering, leading to overall broad and intense extinction bands.[9–11]

For spherical particles, that have the same dimensions along all three particle axes, a triple degenerate LSPR mode is expected.[12] In the case of any other shape, however, geometrical splitting of the LSPR is observed. This can be understood intuitively in the case of oblate particles such as ellipsoids, where there exists one long NP axis and two shorter axes that correspond to a doubly degenerate mode with a higher resonance energy than the one corresponding to the longer axis. The effect of mode splitting can also be observed for NPs at the surface as soon as the NP shape differs from a sphere.[12] While the optical properties of the simple shapes of spherical and ellipsoidal NPs have been mathematically solved around a century ago,[13,14] the theoretical description of the response from more complex shapes is still the topic of current research.[15,16]

Even though applicable for the SPR, equation 2.2 gives a first impression of the influence on the surrounding medium on the LSPR *via* the dielectric constant. This can be altered for example through the choice of solvent in the case of dispersed NPs, the interaction with oxide coatings or support materials, and when in contact with molecular adsorbates. Overall, the LSPR is tunable through adjustment of the particle composition, size, shape, and arrangement. Additionally, the physico-chemical surrounding influences the LSPR immensely.[17–19]

2.2. Induced Circular Dichroism and Chirality Transfer

Molecular Interactions with Induced Circular Dichroism

When a chiral molecule (often referred to as "host") comes into contact with an achiral one ("guest"), an induced circular dichroism (ICD) effect may emerge meaning that the electronic transitions of the guest are now CD-active as well, schematically presented in fig 2.1. The ICD mechanism can either be direct (DICD) or indirect (IICD).[20] 1) One type of DICD appears when the transition dipole moments of host and guest couple (coupled oscillator). This is specifically relevant if the electronic transitions occur at the same scale of energy. The one-electron effect also is a DICD where the host has a strong asymmetric static field that leads to a perturbation of the guest's molecular orbitals. 2) Any other interaction mechanism of host and guest is described as IICD, often incorporating structure perturbation. This usually includes stronger interactions to chemical binding.

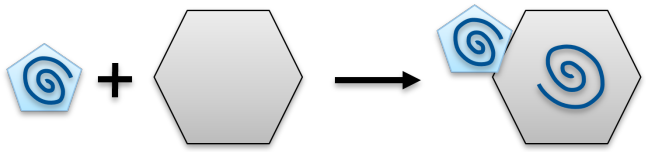

Figure 2.1.: Conceptual representation of induced circular dichroism.

Chirality in Nanostructures and on the Surface

Generally, there are three models proposed for the emergence of optical activity in metal NPs:[21,22] 1) an intrinsically chiral metal core (chiral growth). This is caused by preferential growth of the core due to interaction with the chiral molecule. 2) electronic interactions (chiral polarisation). Similar to the one-electron effect in the case of molecules, the contact of an achiral NP with a chiral molecule can lead to an DICD effect *via* a perturbation of the electron density. Also, a chiral electrostatic field created by a chiral adsorption pattern on the achiral core can induce a chiral distribution of electron density. 3) achiral core but relaxation of surface atoms in a chiral fashion (chiral footprint). This mechanism can be viewed as a

compromise of the extremes 1) and 2), as the mainly achiral metal core experiences surface reconstruction in a chiral fashion due to strong binding. It is pronounced for molecules with at least two binding sites to the surface of the particle and can be compared to the IICD for the case of molecular interactions, vide supra. Optical activity of real NP samples, however, most likely emerges from a combination of these mechanisms. And furthermore, the question whether only the core of the NP, the surface alone, or both carry chirality often remains unanswered.[21]

In the concept of interaction between chiral host and achiral guest, an ICD around the LSPR can be observed for the case of plasmonic nanostructures as the achiral guest.[23–25] Plasmon-enhancement can play a significant role in the formation of new CD signals, especially as soon as transitions of the plasmonic nanostructure and the chiral host are energetically close. At the same time, plasmonic nanostructures can amplify the intrinsic CD of the chiral host through plasmon-enhancement.[26,27]

Similarly, there are several concepts discussed for the existence of chirality at the surface, specifically.[28–30] In addition to intrinsically chiral crystal space groups, defined crystal facets with high Miller indices of achiral space groups can exhibit chirality as well.[30] Another source of chirality on the surface is found by the chiral arrangement of achiral entities, such NPs.[31,32] Furthermore, the achiral or chiral arrangement of chiral molecules can induce chirality. Studies about the chirality on the nanoscale in the sense of planar surfaces – potentially with such arrangements – are often conducted with microscopic methods such as scanning tunnelling microscopy (STM).[30] Furthermore, great efforts are spent for the fabrication and characterisation of metasurfaces with optical activity, also investigated with non-linear spectroscopy.[33–37]

Applications of Induced Circular Dichroism

The ICD effect finds application in a plethora of scientific and technological fields, e.g. chiral sensing, determination of absolute conformations, data storage, drug delivery, as well as optoelectronics,[38,39] also see chapter 6.2 on page 74. We are specifically interested in finding

and exploring a system for asymmetric heterogeneous catalysis. Usually, heterogeneous catalysts such as small metal particles are achiral. However, if the catalyst interacts with chiral entities, ICD may emerge enabling the observation of the asymmetrisation of the heterogeneous catalyst.[3,40,41]

2.3. Circular Dichroism Spectroscopy

Molecular Absorbance

The loss of radiation intensity when passing a medium of interest is generally described by the Beer–Lambert law

$$I/I_0 = 10^{-A} = 10^{-\varepsilon \cdot c \cdot l} \tag{2.3}$$

with the absorbance (extinction) A, molar extinction coefficient ε, concentration c, and length of the path l. This is true for the whole energetic spectrum. However, absorption in the ultra-violet and visible (UV-vis) range generally corresponds to vibronic excitations. Quantum-mechanically, the process of photon absorption corresponds to an excitation of the system from the "initial" (ground) state into the "final" (excited) state of higher energy. The energetic difference between the two states must align with the photon energy absorbed. The transition probability, and therefore the strength of an electronic excitation, is given by the square of the transition dipole moment $|\overrightarrow{\mu_{fi}}|^2$, that itself depends on the wave functions of initial and final state Ψ_i and Ψ_f, the electron spin wave function S_i^e and S_f^e, as well as the electronic dipole moment operator $e \cdot \overrightarrow{r}$,

$$\overrightarrow{\mu_{fi}} = \langle \Psi_f^e | e \cdot \overrightarrow{r} | \Psi_i^e \rangle \cdot \langle S_f^e | S_i^e \rangle \cdot \langle \Psi_f^v | \Psi_i^v \rangle \tag{2.4}$$

with the indices e for electronic and v for vibrational wave functions. The last factor here represents the vibrational overlap of the wave functions involved (Franck–Condon factor) that leads to the observation of vibronic bands rather than purely electronic transitions in a UV-vis spectrum. The second factor equals the Kronecker delta ($\langle S_f^e | S_i^e \rangle = \delta_{fi}$) meaning that

transitions with a change of the total spin are forbidden. In contrast, the first factor concerns the symmetry selection rules of the molecule of interest.[42,43]

The variety of possible interactions of electromagnetic radiation with a molecule, or matter in general, can be described mathematically as a multipole series. At first approximation, the interactions of electric dipole–electric field and magnetic dipole–magnetic field appear as the most prominent,[42,44] also see chapter 2.4. Accordingly, one can define the dipole strength D of a electronic transition[42,43]

$$D = |\overrightarrow{\mu}|^2 + |\overrightarrow{m}|^2 \tag{2.5}$$

that depends on the electronic and magnetic dipole transition moments $\overrightarrow{\mu}$ and $\overrightarrow{m}$, respectively. This entity can also be derived from experiment by integrating the spectra.

Circular Dichroism

The most common spectroscopic technique for determinations regarding chirality uses the effect of circular dichroism (CD), which is defined as the differential extinction coefficient of left- and right-handed circular polarised light according to[44,45]

$$CD \equiv \Delta\varepsilon = \varepsilon_l - \varepsilon_r \tag{2.6}$$

where the indices l and r regard to the left- and right-handed circular polarised light, respectively. Similarly to the definition of dipole strength D (equation 2.5), the rotatory strength R can be defined as[44,45]

$$R = |\overrightarrow{\mu}| \cdot |\overrightarrow{m}| \cdot cos\varphi \tag{2.7}$$

where φ is the angle between electronic and magnetic dipole moment $\overrightarrow{\mu}$ and $\overrightarrow{m}$, respectively. Accordingly, in order for CD-activity of a molecular transition, both $\overrightarrow{\mu}$ and $\overrightarrow{m}$ must be unequal to zero while the two vectors must not be perpendicular to each other as well ($\varphi \neq 90°$).[45]

Instrumentally, the difference in absorbance of left- and right-handed circular polarised light ΔA is measured directly. Nevertheless, CD is often given as the ellipticity Θ (mdeg) for historical reasons. However, since A and ΔA depend on concentration and path length according to equation 2.3, the anisotropy factor g is regularly used for ease of interpretation and comparison with other samples, that is defined by the CD normalised over absorbance,[45]

$$g = \frac{\Delta A}{A} = \frac{\Delta \varepsilon}{\varepsilon} = 2\frac{\varepsilon_l - \varepsilon_r}{\varepsilon_l + \varepsilon_r} = 4\frac{R}{D} \tag{2.8}$$

where ε represents the average over ε_l and ε_r. The sign of g (ΔA, $\Delta \varepsilon$, Θ) can be determined with the knowledge of the orientation of $\overrightarrow{\mu}$ and $\overrightarrow{m}$ within the molecule. With a parallel arrangement of the two vectors, g reaches its positive maximum while anti-parallel orientation leads to the negative extreme. Since enantiomers are of image–mirror image structure to each other, the transition dipole moments $\overrightarrow{\mu}$ and $\overrightarrow{m}$ and their angle $cos\varphi$ experience a change in sign when going form one enantiomer to the other. Thus, the image–mirror image behaviour of CD curves for the two enantiomers can be understood intuitively.[45]

Circular Dichroism and the Solid Phase

In the solid phase, not only the resonant transitions of chiral molecules influence the CD spectrum, but also structural effects and ordering may play a role. In the case of thin films of chiral organic molecules, a flip of CD with reversal of the light propagation direction in the sample is regularly observed, however, not for every system. Also, a modulation of the CD signal is possible upon rotation of the sample around the light propagation direction. These effects are generally associated to structural aspects inherent to the solid phase that lead to alterations to the perceived CD response, i.e. linear dichroism (LD), linear birefringence (LB), and circular birefringence (CB).[46] With an approach based on Mueller-matrices, the different contributions can be disentangled to a certain degree.[47–49] In contrast, simulations on the chiroptical properties of the thin films quantify the individual contributions, revealing that the structural effects sometimes strongly dominate the overall perceived CD response.[46]

Another effect influencing the CD spectra of solid samples is circular differential scattering (CDS), a preferential scattering by large chiral structures depending on the circular polarisation of the incident light. As a special case of Rayleigh scattering, the intensity of CDS depends indirectly proportional on the wavelength to the power of four ($I_{CDS} \propto \lambda^{-4}$). Additionally, CDS becomes more pronounced with a similar size of the chiral structures in comparison to the wavelength. CDS has been observed for example in crystallised thin films of chiral molecules[49–51] and for macromolecules such as protein-nucleic acid complexes,[52,53] but also in the case of chiral assemblies of achiral noble metal nanoparticles.[54]

Also interesting in terms of optical activity in the solid state is the observation of psi-type CD. This phenomenon summarises different interactions of large chiral structures and aggregates with left- and right-handed circular polarised light, including resonance excitation with strong delocalisation of the excited states within long-range chiral structures. Similar to CDS, the effect of psi-type CD becomes larger when the particle size matches the wavelength, in order of magnitude.[55]

2.4. Second Harmonic Generation Circular Dichroism Spectroscopy

Surface Second Harmonic Generation

With higher field strengths of the incoming electromagnetic radiation, e.g. in the case of laser light, processes of higher order become relevant in addition to the linear response. This is the case as soon as the polarisation $\overrightarrow{P}$ in the material under investigation starts to depend non-linearly on the electric field strength $\overrightarrow{E}$. This dependency is typically described in a power series of $\overrightarrow{E}$,[56,57]

$$\overrightarrow{P}(t) = \varepsilon_0 \chi^{(1)} \overrightarrow{E}(t) + \varepsilon_0 \chi^{(2)} \overrightarrow{E}(t)^2 + \ldots \tag{2.9}$$

where $\chi^{(n)}$ is the susceptibility tensor of nth order. The second term is defining for second-order non-linear processes, such as sum and difference frequency generation, as well as the

special case of second harmonic generation (SHG). Accordingly, the SHG intensity depends on the susceptibility tensor of second order $\chi^{(2)}$.[56]

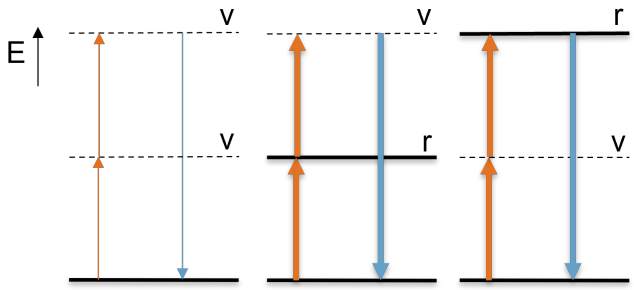

Figure 2.2.: Resonance modes of non-resonant SHG and resonance-enhanced SHG with virtual (v) and real (r) states.

During the collinear SHG process, the energy $\hbar\omega$ of two fundamental photons are absorbed and transformed into one single photon with double the energy of the fundamental radiation $2\hbar\omega$,[56,57] see fig 2.2. In a generic system without real electronic states, SH is generated equally over the spectral range without pronounced spectral features. In contrast, a strongly increased SHG intensity is observed with a transition in resonance with the fundamental or SH photon. Overall, the SHG intensity in transmission depends on the SHG conversion efficiency (including $\chi^{(2)}$), the electric field strength and incidence angle of fundamental radiation, geometric properties of the sample, and more parameters.[58]

In the electric dipole approximation, the elements of $\chi^{(2)}$ vanish in centrosymmetric media for symmetry reasons.[56] However, inversion-symmetry across surfaces and at interfaces is broken so that SHG processes perpendicular to the surface become symmetry-allowed. Therefore, one expects contributions solely from the interfaces, in the case of centrosymmetric support materials such as isotropic glasses.[59] This surface-sensitivity means that SHG of nanoparticles on centrosymmetric supports is plasmon mode-selective (also see chapters 2.1,4.1). Similarly, ordered molecules at the surface can be probed by SHG in regards to their orientation.[56]

Second Harmonic Generation Circular Dichroism

The susceptibility tensor of second order of a chiral medium $\chi^{(2)}$ is comprised of achiral and chiral tensor elements. While the achiral elements are electric dipole-forbidden as of the symmetry selection rule mentioned above, higher-order contributions such as electric quadrupole and magnetic dipole are generally allowed. The chiral and achiral contributions can be evaluated by modifying the combination of linear input and output polarisations.[56]

Alternatively, for the detection of chirality with non-linear spectroscopy, SHG can be combined with CD, meaning that the sample generates a different amount of SH for the fundamental radiation being left- and right-handed circular polarised, respectively. Analogously to fundamental CD spectroscopy (equation 2.8), the anisotropy factor g of SHG-CD is defined by the difference of SH generated by left- and right-handed circular polarised light I_l and I_r, respectively, normalised over their average,

$$g = \frac{\Delta I}{I} = 2\frac{I_l - I_r}{I_l + I_r} \tag{2.10}$$

also see chapter 3.2. This approach was introduced by Hicks and co-workers in the 1990s.[60–63]

A main advantage of SHG-CD over the fundamental CD is the increased CD-sensitivity. The non-linear anisotropy factor is up to three orders of magnitude larger in comparison to the fundamental one. This allows high surface-sensitivity that reaches sub-monolayer sensitivity for SHG-CD.[60,63–66] Another important difference is that SHG-CD depends on the molecular orientation *via* the arrangement of the transition dipole moments.[56,67] Also, SHG-CD is basically background-free since the generation of photons is detected, instead of a difference in transmission.

3. Experimental

3.1. Sample Preparation

Supported Gold Nanostructures

In the course of this thesis, a variety of supported gold nanostructures were characterised in regards to their interaction with the chiral molecules Binol or Cysteine (tab. 3.1). Preparation methods are equally diverse and range from nanoimprinting followed by etching (imprinted cylinders) to thermal dewetting of gold thin films (hemispheres) and sputtering deposition (spheres). Some of the samples have an adhesive interlayer of titanium between the borosilicate support and the nanostructures, which increases resilience against laser desorption during measurement. A full list of samples can be found in the appendix (page 101).

Table 3.1.: Overview on employed supported gold nanostructures

Description	LSPR (nm)	Support	Coating	Literature
Spheres	580	BK7	Cysteine	Refs. [68, 69]
Hemispheres	560	BK7	Cysteine	Refs. [70–72]
Porous hemispheres	640	BK7	Cysteine	-
Imprinted cylinders	640	Ti/BK7	Binol	Ref. [73]

Molecular Evaporation

Submonolayer-precise deposition of molecules onto nanostructures or support materials was achieved with a molecular evaporator of in-house design, that is based on resistive heating. Both the evaporator setup and details about the procedure itself have been reported before.[66]

In short, the deposition is monitored *via* a INFICON *345 12* quartz crystal microbalance (QCM) operating at 6 MHz. The eigenfrequency of the QC changes upon molecule adsorption and is correlated to the change of adsorbed mass by the SAUERBREY equation. With molecular mass and under the assumption of the molecular volume of the crystal structure of the molecule also being valid for the evaporated film, the change in mass can be transferred into number of deposited molecules and film thickness in situ (tab. 3.2).

Table 3.2.: Heating and crystal parameters for molecular evaporation

Molecule	Heating current (A)	Volume constant (a.u.)	Literature
Binol	0.9	$3.57 \cdot 10^{-22}$	Refs. [67, 74]
Cysteine	0.8	$2.63 \cdot 10^{-23}$	Ref. [75]

3.2. Characterisation and Data Evaluation

Linear Spectroscopy and Microscopy

UV-vis spectroscopy was performed on a ANALYTIK JENA *Specord-40* device.

Circular dichroism (CD) spectroscopy was conducted with a JASCO *J-815* spectrophotometer. In the case of liquid samples, two-way quartz cuvettes from THORLABS with path lengths of 2 mm were used. Solid samples, such as supported particles and thin films, were measured in several geometries for each sample (support and sample first in the beam path; 0°, 45°, 90°, and 135° rotation of the sample around the beam path).

Atomic force microscopy (AFM) images were taken with a NANOSURF *easyScan 2* setup with external controller and an *isoStage* vibration buffer.

Setup for Nonlinear Spectroscopy

" The experimental setup for s-SHG spectroscopy was reported before[66] and the parts used during this experiment are summarized here very briefly[, see Fig. 3.1]. The setup consists of a combination of ultra-high vacuum (UHV) chambers for sample preparation and storage,

and an optical unit for s-SHG and cavity ring-down (CRD) spectroscopies. " (Ref. [70])

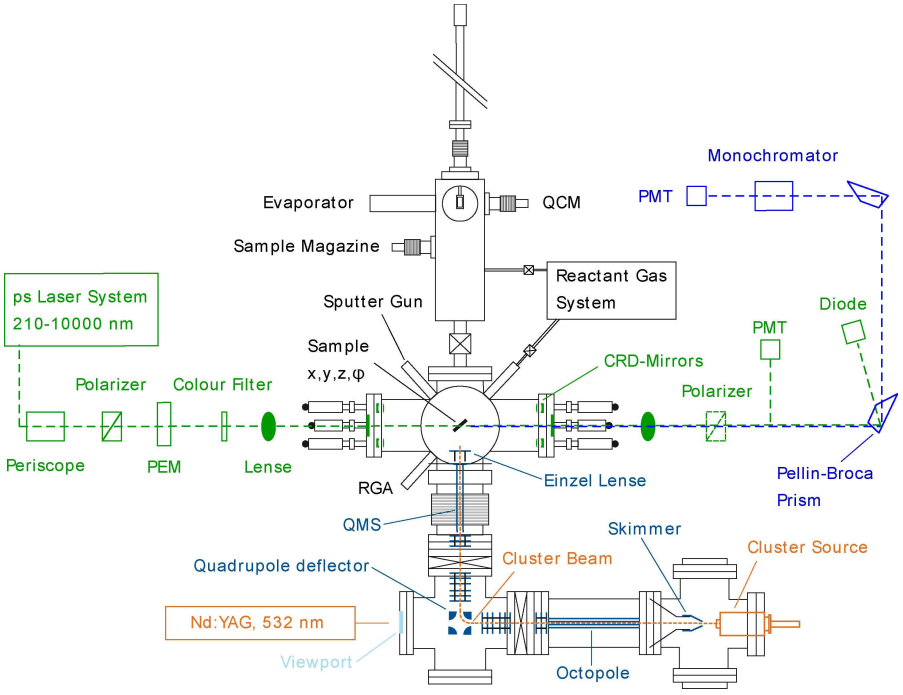

Figure 3.1.: Setup for nonlinear spectroscopy. Reproduced with permission from ref. [66].

" The UHV analysis chamber has a base pressure of $1 \cdot 10^{-10}$ mbar and is equipped with a four-axes manipulator head for sample positioning (x, y, z, φ). For our experiment, also important is the attached transfer chamber which allows sample introduction into the analysis chamber without braking the vacuum [and molecular evaporation]. In the transfer chamber, sample storage in the depot is possible as well.[66] " (Ref. [70])

" Regarding the optical components, the radiation emitted before the chamber is monochromatic and coherent and is generated by an optical parametric amplifier system *PG401* from Ekspla, which covers the range from 210 to 10000 nm with 30 ps pulses at 20 Hz repetition rate. After polarizing and filtering components (Glan-Laser calcite polarizer, *II FS42A* from Hinds Instruments, *FELH0400* from Thorlabs), p-polarized light is focused onto the sample within the UHV chamber. Here, SH is generated collinearly to the fundamental radiation. After recollimation after the chamber, fundamental and SH radiation are separated with two rotatable Pellin-Broca prisms and a monochromator (*Omni-λ150* from LOT) and detected

by a silicon-based photodiode and a photomultiplier tube (*H9305-03* from HAMAMATSU), respectively. A *Waverunner* oscilloscope processes both resulting currents. The SH spectrum is then corrected by the fundamental laser power and for the spectrometer function.[66] " (Ref. [70])

Evaluation Routine for SHG-CD Measurements

SHG-CD measurements can either be conducted as a wavelength-dependent scan or, alternatively, for a larger amount of laser pulses at a single wavelength being called *time measurement*, with the aim of increased statistics and error estimation. Latter is a repetition of several single point measurements at one specific wavelength and after the evaluation procedure, the data is represented as a single point in a spectrum. The reference for both measurement modes is either the bare support, or the support with a racemic mixture of the molecule of interest.[66]

By importing the oscilloscope trace files with *Igor Pro*, one corrects the curves of each polarisation for power and detector-sensitivity. For the wavelength-dependent mode, the curves of the sample are then corrected with a smoothed function of the reference material, and the anisotropy factor g is calculated afterwards according to

$$g = 2\frac{A - C}{A + C} \tag{3.1}$$

with A and C being the SHG by left- and right-handed circularly polarised light, respectively.[66]

For time measurements, the reference correction takes place by dividing the sample curves for left- and right-handed circularly polarised light by those of the reference material, respectively, and calculation of g as in

$$g = 2\frac{\frac{A_s}{mean(A_r)} - \frac{C_s}{mean(C_r)}}{\frac{A_s}{mean(A_r)} + \frac{C_s}{mean(C_r)}} \tag{3.2}$$

with indices s for sample and r for reference data waves, respectively. Afterwards, the resulting wave of g is averaged into a single value, while the standard error of means serves as statistical

measure. This procedure readily allows background corrections of time measurements with sample and reference data waves being of different length while maintaining decent error estimations, and was implemented as script functions within *Igor Pro*.

3.3. Laser System Calibration for SHG

Prism Calibration with SH Adjustment Stage

The laser used for nonlinear spectroscopy is a Ekspla *PG-401* system with variable wavelength between 210 and 10000 nm, based on a diode pumped Nd:YAG rod. After creation of second and third harmonic of the initial radiation of 1064 nm, the wavelength is adjusted by optical parametric generation and amplification.

For the automation of spectroscopy measurement, two step-motors – one for each Pellin-Broca prism – are employed. The rotation of these step-motors with wavelength must be calibrated after beam path alignment.[66] Since fundamental and SH beams of the OPA laser (for example 560 and 280 nm, respectively) don't overlap spatially after the laser units due to mechanical restrictions, the SH beam must be adjusted without changing the original (fundamental) beam path, in order to have a precise separation of fundamental and SH during the experiment. With introduction of a stage with three additional mirrors, this can be achieved (fig. 3.2). Thus, the beam path of fundamental is fixated by means of two orifices and the introduced mirrors on the removable stage are adjusted, so that the SH beam is passing through both targets. Tab. 3.3 gives a suggestion on which settings to use.

Table 3.3.: Fixated fundamental wavelength for prism calibration

Fixated (nm)	Calibration (nm)
480	450-500
560	520-580
640	600-680
740	740-1100

Calibration of prism positions with wavelength then leads to curves similar to exponential

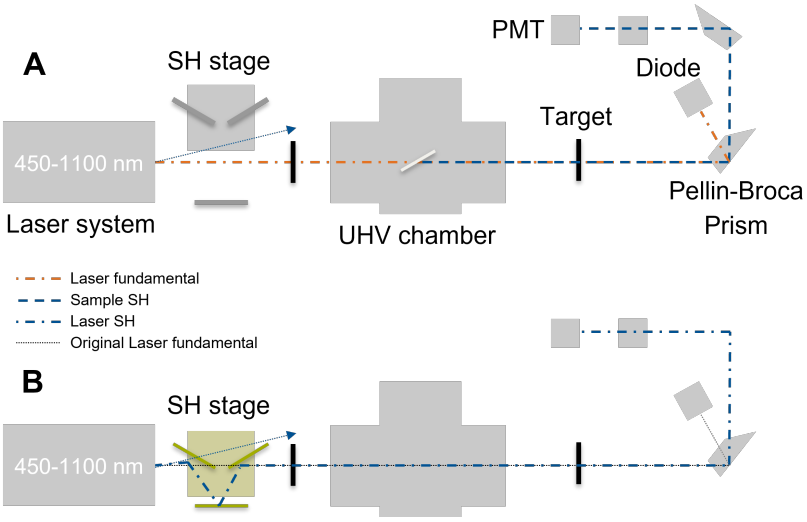

Figure 3.2.: Simplified setup overview during measurement (A) and during prism calibration with SH adjustment stage in the beam path (B).

functions, as reported before.[66] As a benchmark, a freshly evaporated thin film of 230 nm (320 ML) of R-Binol on a BK7 substrate has proven to be handy, vide infra.

Reproducibility with Spectrometer Calibration

The SHG-CD spectra of both enantiomers and the racemic mixture of Binol thin films are already known.[66] The spectra included a high energy band above 240 nm SH, a middle energy band around 280 nm SH, and a low energy band above 330 nm SH. Depending on the enantiomer used, the SH intensity observed with left- and right-handed circular polarised light (lcp and rcp, respectively) of those three bands varied. In the case of a R-Binol film of 2000 ML, the authors found a strongly positive anisotropy factor at short wavelengths and a zero-crossing around 265 nm SH, followed by a negative g for longer wavelengths. For a sub-ML film thickness, g was less extreme and especially around the high energy band way closer to zero.[66]

Fig. 3.3A shows the SHG-CD curves of several freshly evaporated R-Binol thin films on BK7 with nominal 320 ML (230 nm) film thickness. The samples were measured at different days, with adjustments and changes on the setup of the SHG-CD spectrometer such as alignment

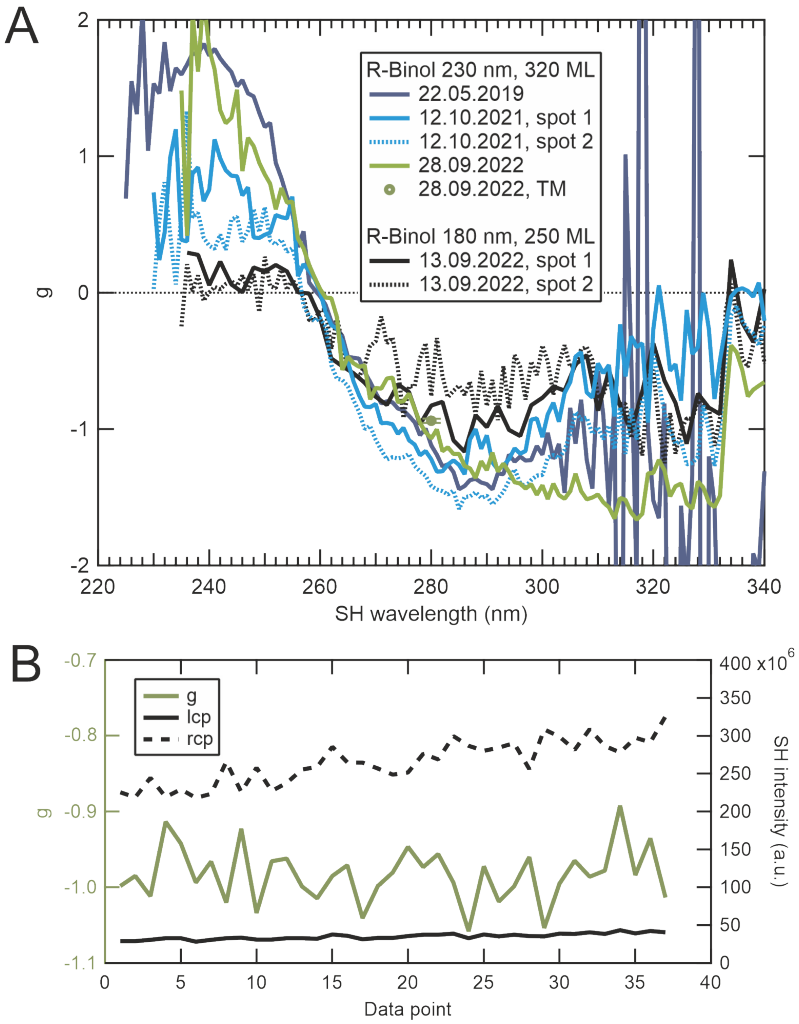

Figure 3.3.: SHG-CD spectra of R-Binol thin films on BK7 substrates with 320 ML and 250 ML film thickness (A), and g over the course of a *time measurement* at 280 nm SH (B).

of laser and beam path of the analytics unit, baking of the ultra-high vacuum chamber, and prism replacement and recalibration. It becomes evident that all spectra inherit the same spectral features: At short wavelengths, the anisotropy factor is positive, reaching nearly the maximum per definition of $g = +2$. After the zero-crossing around 260 nm SH (560 nm fundamental), the curves reach a plateau of around $g \approx -1$ for 280 nm SH and above. This is very comparable with the anisotropy factor found for thicker films of R-Binol in terms of order of magnitude.[66] The zero-crossing at a slightly lower wavelength may originate from the thinner layer (320 *vs.* 2000 ML).

With slightly thinner layers of R-Binol (250 ML, 13.09.2022), the zero-crossing and negative part of the spectrum are observable similarly as before, while the positive feature below 260 nm is hardly present. This band appears to depend strongly on the film thickness as can be seen for measurements at several spots on the same sample (12.10.2021 and 13.09.2022). Due to the geometry of the setup during evaporation, there may be deviations in the film thickness depending on the support and laser spot positions. For SHG-ORD measurements at 674 nm fundamental (337 nm SH) with increasing Binol film thickness, the molecules reached their final orientation with a coverage of $5 \cdot 10^{16}$ molecules $\cdot$ cm^{-2} (225 ML).[67] However, the band around 240 nm SH appears sensitive to layer thickness changes beyond that point for SHG-CD measurements.

For this setup, a sufficient sensitivity in statistical regards of ML and even sub-ML detection of Binol thin films has already been shown.[66] In the present case, a representative curve for measurements of one sample at the same position is shown by repeating the SHG-CD measurement at a single wavelength several times (fig. 3.3B, compare also chapter 3.2 on page 16). While small fluctuations are certainly present, the standard error is only around 1.2 % of the mean value during the 37 repetitions. This examination then forms data in the shape of a single point in the g spectrum of fig. 3.3A, and lies well within the less statistically challenging measurement curve (28.09.2022, TM).

Overall, the SHG-CD spectrometer setup gives data that satisfy the claims about reproducibility after setup changes and readjustments. Thus, a freshly evaporated R-Binol film of

320 ML (230 nm) film thickness is suggested as benchmark for the system, being quick and straightforward in preparation while exhibiting a handy SHG-CD signal intensity as well.

4. Suitability of SHG-CD Spectroscopy for Model Catalyst Examination

This chapter aims to show the strengths of SHG and SHG-CD spectroscopy for investigations within asymmetric heterogeneous catalysis, namely sensitivity to minute changes in structure, surrounding, and orientation. First, supported Au NPs with varying titania coating are investigated, that have already proven useful as heterogeneous catalysts. Afterwards, the focus shifts towards Cysteine thin films which may serve as adsorbates onto metal NPs in the picture of catalysis, or as chiral inducer for asymmetrisation of the heterogeneous catalysts.

4.1. Supported Gold Nanoparticles with Titania Coating

The combination of metal NPs and semiconductor oxides have been intensively investigated for several catalytic and photocatalytic reactions, such as carbon dioxide reduction, hydrogen evolution, and alcohol photoreforming.[76–78] When in contact with the oxide, the NP bands experience bending, which promotes charge carrier separation.[79] Furthermore, an oxide coating can help in protecting the NPs from degradation and ripening.[80] Overall, Au NPs with titania coating comprise an intriguing system for catalytic applications and were therefore examined through SHG in dependence on the titania coating thickness. The following is a comprehensive summary of our publication, ref. [70].

The supported Au NPs were prepared by thermal annealing of sputtered Au thin films on BK7 glass slides. Afterwards, titania was deposited *via* atomic layer deposition (ALD) with nominal thickness ranging from 0 to 10 nm. The resulting particles have an average

diameter of 36 ± 22 nm. Most of the NPs are around $20 - 40$ nm in size, while few large NPs are present as well (fig. 4.1A).

For the optical properties of the NPs, each size will contribute according to the number of atoms per NP and the particle count. Accordingly, Mie calculations for the NP ensemble reveal that the majority of the optical response stems from the larger particles, few in number but dominating the absorbance spectra. The resulting curves of the ensemble can be fitted equally well by one and two Gaussian functions, meaning that the overlap of plasmon resonances conceals a discrimination of different NP sizes or plasmon modes. Ultimately, tracing of small details as well as changes in structure or interactions becomes impossible by means of UV-vis spectroscopy alone, in this case.

With increasing titania coating, the surrounding medium of the NPs constantly changes, leading to a red-shift of the plasmon frequency. Also, the absorbance becomes more intense. Experiment complies to our expectations from theory (fig. 4.1B).

As for the SHG spectra, from the bare NPs to the thickest titania coating, a red-shift and an increase in intensity are clearly visible as well (fig. 4.1C). However, a fit of the plasmon energies reveals that the resonance from SHG spectroscopy remains constant for a coating of up to 5 nm nominal thickness followed by a sudden drop in resonance at 10 nm nominal thickness, while the ones from UV-vis spectroscopy experience a constant decline with increasing thickness (fig. 4.1D). Only transitions with a transition dipole moment perpendicular to the surface are SHG-active, which is the plasmon mode of the particle height in the present case. Thus, the mode perpendicular to the surface is not affected much by the change in surrounding through coating for the first few nm. This is conclusive with a model where the oxide support and the NP's low coordination sites – like corners and edges – are coated first and full encapsulation happens with thicker coatings only, as sketched in fig. 4.1E. We found full encapsulation with a nominal thickness of 10 nm *via* voltametry measurements, while for NPs with 5 nm titania, the Au surface was still exposed. The proposed model finds further confirmation by simulations of small supported Au NPs with titania coating *via* ALD.[81]

SHG examinations on Au NPs with increasing titania shell have already been reported

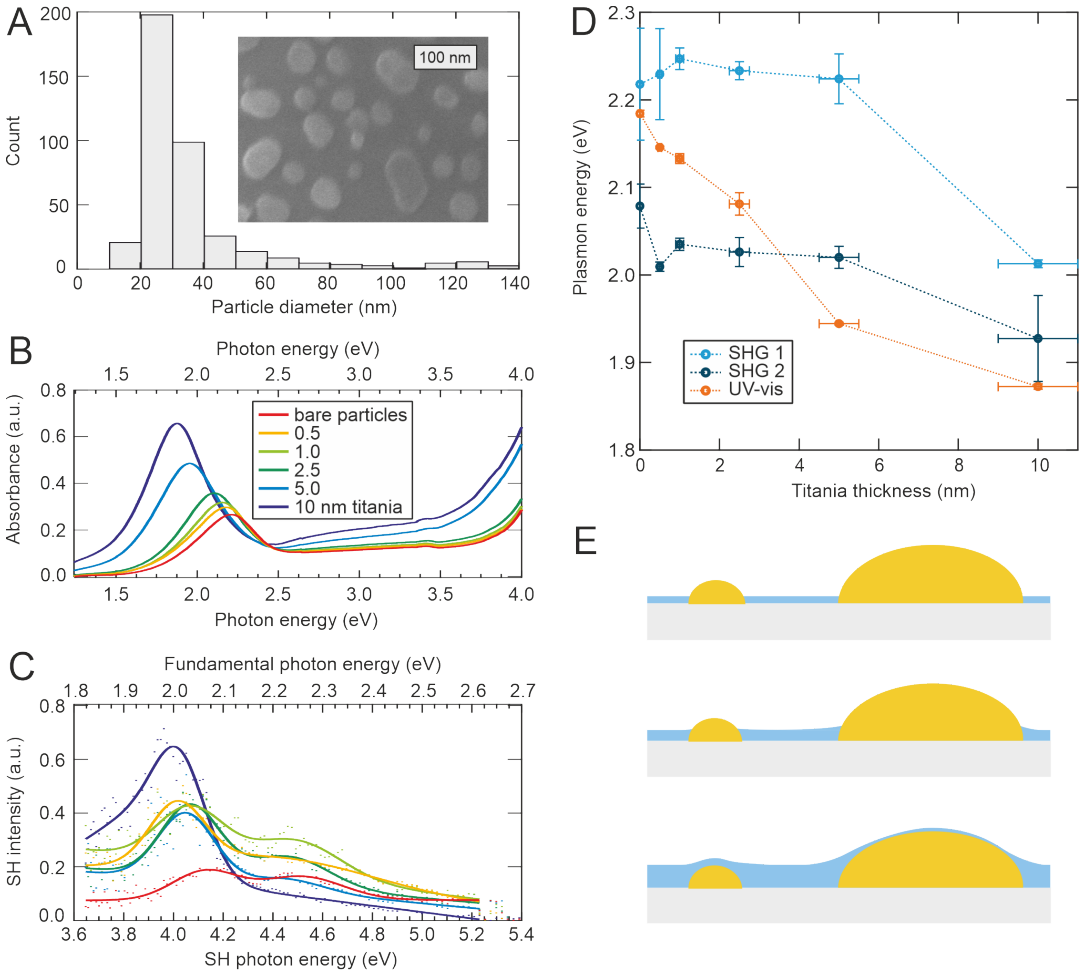

Figure 4.1.: Supported Au NPs with increasing titania coating thickness. Size distribution and representative He^+ micrograph (A), UV-vis (B) and SHG spectra (C), plasmon resonances with coating thickness (D), and coating model (E). Modified from Ref. [70].

and gave insights into the shell growth process. It is a plausible conclusion to attribute the increase of SHG signal towards stronger off-resonant absorption for the particles.[82] Nevertheless, with measurements at a single wavelength, the amount of information gained is naturally limited. In our publication,[70] we presented the SHG spectra of such NPs with variation of the titania coating thickness for the first time, to the best of our knowledge. In this way, we are able to take into consideration the plasmon bands in SHG and their shift with changing physico-chemical surrounding as well.

For each of our samples, there are two bands in SHG observable (fig. 4.1C,D). The mode-selectivity of SHG allows to distinguish transitions that overlap in the case of UV-vis spectroscopy. Thus, the appearance of those two bands can be attributed to a bimodal distribution in NP height, meaning that there are two populations of NPs with different heights. The flatter population corresponds to stronger confinement and therefore higher resonance energy. Also, the flatter NPs must have a thicker layer of titania after coverage than the higher NPs, so that their plasmon resonance experiences a stronger red-shift – which is exactly what the data show in fig. 4.1D.

Overall, this data set renders an excellent example for demonstrating the sensitivity of SHG spectroscopy. Due to the mode-selectivity, s-SHG revealed more insights into structure and especially structural details, in comparison to UV-vis spectroscopy: 1) Minute changes in physico-chemical surrounding of the NPs were detected, that come along during the oxide coating process. 2) The NPs' bimodal size-distribution in height was discernible only through SHG spectroscopy. Thus, SHG is a suitable method for the examination of model systems for the application in asymmetric heterogeneous catalysis comprised of Au NPs.

4.2. Cysteine Thin Films on Oxide Supports

SHG and SHG-CD have already been employed for investigations of structural details in thin molecular films, such as orientation of the molecules.[64,67] With the thiol group, the chiral amino acid Cysteine can form strong interactions to metals with high polarisability

such as gold and silver.[83] Especially with thiol-ligand protected gold nanoparticles, there exist a plethora of investigations on their optical properties in the liquid phase with the aim of functionalisation of the nanoparticles, dynamics and mechanisms of aggregation and ligand-exchange, or applications in sensing.[84–89] However, on defined facets of gold and silver crystals, such as Au(110)[65,90,91] and Ag(111),[92,93] Cysteine has been studied in regard to orientation and arrangement mainly through microscopic methods, while Cysteine on oxide surfaces was given less attention. Cysteine is thus an interesting candidate as chiral inducer of model catalysts made from gold nanoparticles, and was therefore examined by SHG-CD with variation of the film thickness. Two commonly used oxide supports were chosen, namely borosilicate (BS) and fused silica (FS).

Fundamental Absorbance and CD Spectroscopy

Fig. 4.2 shows the fundamental CD spectra of both Cysteine enantiomers in aqueous solution in comparison to thin films of L-Cysteine on BS and FS glass supports. For Cysteine in solution, only the onset of the transition lowest in energy is visible in the examined range, with a maximum below 200 nm. This transition has a pronounced CD-activity, that follow the behaviour of enantiomers being as image and mirror-image, as expected.

Thin films of L-Cysteine on FS show an additional feature around 230 nm in absorbance. Additionally, pronounced scattering becomes visible that obscures the optical response of the molecules themselves. However, over the scattering in the off-resonant part above 250 nm, the additional feature around 230 nm can be identified as a red-shifted band due to the contact with the surface. The CD curve is characterised by small circular differential scattering (CDS) above 250 nm and an intense monosignate band below 250 nm. Substrate absorbance for FS happens below 195 nm for FS, allowing for detection of these transitions.

In contrast, for the film on BS glass, only the off-resonant parts are visible because of support absorption below 300 nm. The absorbance and CD, however, follow the same overall impression as in the off-resonant case for FS supports but with greater scattering in comparison, despite the smaller film thickness (900 *vs.* 1500 ML). This can be understood

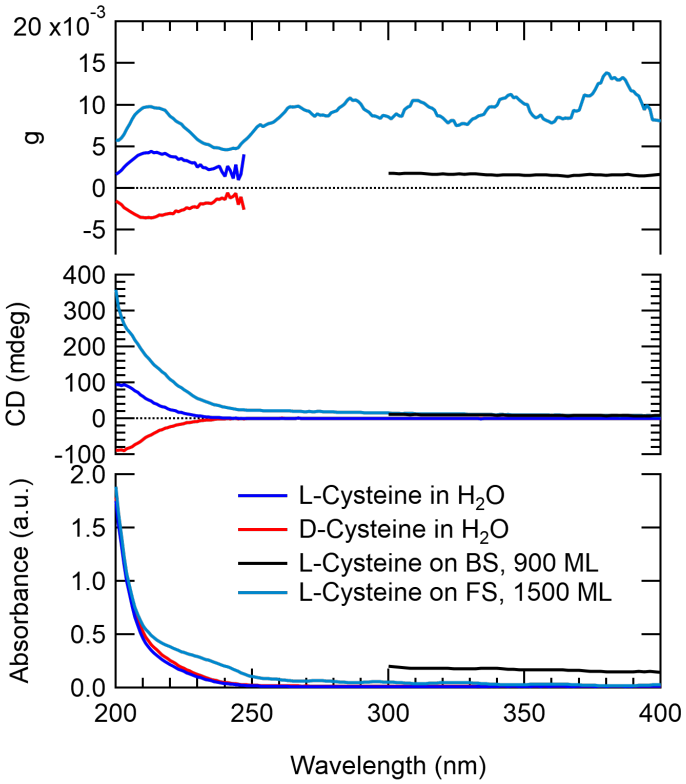

Figure 4.2.: CD spectra of D- and L-Cysteine in aqueous solution in comparison with D-Cysteine on fused silica (FS) and on borosilicate glass (BS).

from atomic force microscopy (AFM) images, where the supports with L-Cysteine show a roughness in the same order of magnitude, even though the L-Cysteine film thickness on BS being 250 ML and on FS being 1500 ML.

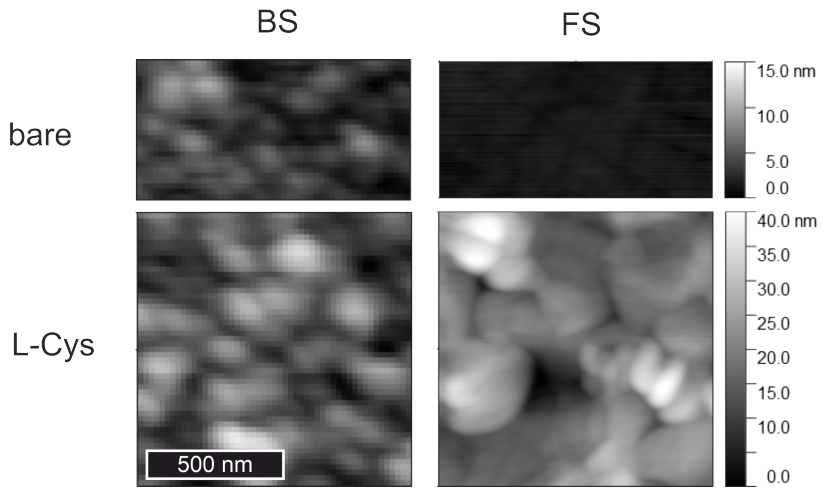

Figure 4.3.: Atomic force microscopy images of BS (left) and FS (right), bare (top) and with L-Cysteine (bottom). Scale: 500 nm.

In addition to scattering and eventual absorbance bands, an interference pattern similar to the etalon effect is observed in the absorbance curve of L-Cysteine on the oxide supports. Through reflection at the air-glass, glass-film, and film-air surfaces, constructive and destructive interference occur in dependence on the wavelength of incoming radiation, adding to scattering and absorption of the sample itself. Since the anisotropy value/factor g depends on both CD and absorbance, this effect also creates the periodical artefacts in the g spectra.

The conformational freedom of Cysteine molecules, especially in the gas and liquid phase,[94,95] complicates investigations that are influenced by the molecular orientation, such as analysis of oriented thin films or oriented molecules at the surface. Nevertheless, ultraviolet photoelectron spectroscopy (UPS) studies of Cysteine thin films on FS[96–98] revealed the nature of the various transitions, in dependence on the conformer studied. The band lowest in energy corresponds per definition to the HOMO-LUMO transition, that was determined to have charge-transfer character in the case of L-Cysteine thin films of 400 nm (800 ML) thickness. The HOMO has a strong contribution from S-3sp, while the LUMO is dominated by O-2p and

C-2p orbitals. The onset of the transition was found to be at 5.8 eV (220 nm), that is in good agreement with our experiment. Also, the comparison of experimental and simulated UPS spectra revealed the preferred (average) conformation of Cysteine within the films, that can be described as elongated so that the acid and thiol moieties have a maximum distance.[96–98]

SHG and SHG-CD Spectroscopy

SHG spectra in dependence on the polarisation of fundamental radiation of selected film thicknesses of L-Cysteine on BS and FS supports are shown in the lower part of fig. 4.4. With increasing film thickness, a more pronounced SHG signal is observed in both cases of support materials. While hardly any SH is generated by very thin layers of 20 ML Cysteine, the emergence of two bands around 260 and 320 nm SH wavelength is observed for a film thickness of $200 - 250$ ML. For very thick layers of over 900 ML, intense SH is generated and the two bands become more pronounced.

Overall, Cysteine on a BS support generates more SH than on FS despite of the slightly thinner film examined (900 *vs.* 1500 ML). All samples have been prepared freshly – shortly prior to characterisation – so that crystallisation and structural surface reconstruction processes play a negligible role. This hints towards slightly different preferred orientations of the molecules on the two surfaces or differences in surface quality in terms of surface roughness and defect sites of the support materials, vide supra.

For molecules on FS supports, an interference pattern is clearly visible over the full range of measurement. This happens due to the support being transparent above 195 nm. SH generated at the interface vacuum–glass, facing the radiation source, will then interfere with SH generated at the interfaces glass–molecules and molecules–vacuum. While being beneficial in fundamental CD spectroscopy in terms of spectroscopic window (fig. 4.2), in the case of SHG spectroscopy this interference complicates data analysis since it appears for all polarisations and additionally in the anisotropy factor g (top of fig. 4.4), reducing the perceived data quality of SHG and SHG-CD bands and hindering sensitivity. This is also the case for BS supports, but only above 600 nm fundamental (300 nm SH) due to its spectroscopic

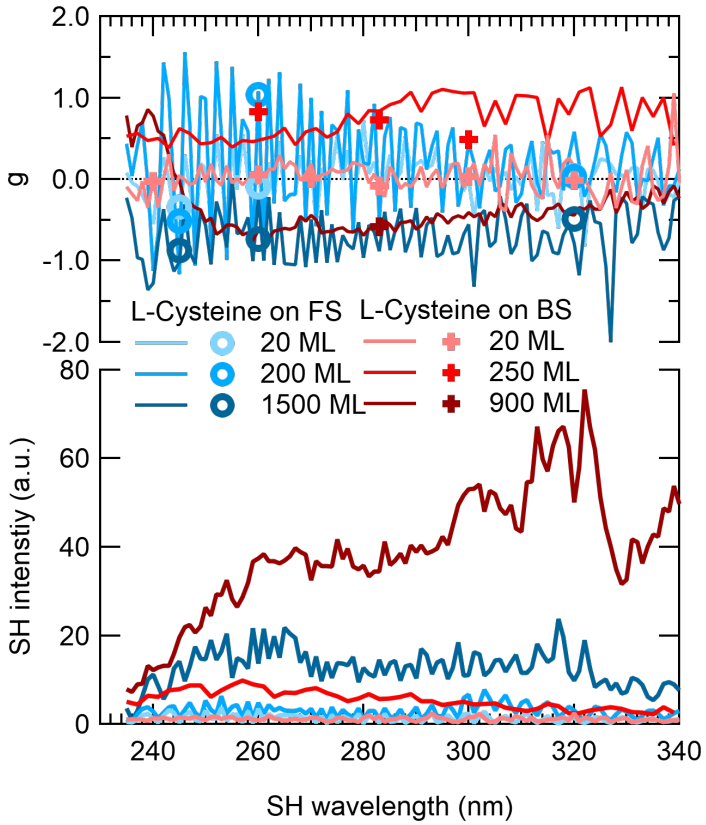

Figure 4.4.: SHG (bottom) and SHG-CD spectra (top) of L-Cysteine on FS and BS substrates with selected film thickness.

window, leaving the remaining range of measurement pristine.

Regarding the SH generated by the different incoming polarisations (top of fig. 4.4), the anisotropy factor remains around zero for thin layers of 20 ML. With a moderate thickness of 200 ML, a positive g is observed of around $g \approx +0.75$ while the sign changes for thick layers above 900 ML ($g = -0.75$ at 260 nm SH). In the case of crystallised Binol thin films, a strong modulation of the non-linear g was observed depending on the orientation of the molecules within different parts of a crystal domain, so that for one enantiomer the values $g = -1.0$ until $g = +1.5$ were observed.[49] However, this structural effect plays a minor role in the present case, since the thin films have been examined shortly after preparation, vide supra.

Off-resonant SHG-ORD examinations on increasing film thickness of Binol layers on borosilicate supports showed that the molecules reach their final orientation with $5 \cdot 10^{16}$ molecules·cm^{-2} (ref. [67]). This corresponds to a film thickness of around 225 ML (160 nm). However, for the higher energy band of Binol in SHG-CD (resonant), we observed earlier distinct g values for films of 250 *vs.* 320 ML (180 *vs.* 230 nm) thickness (chapter 3.3, page 18). While the sensitivity-range on changes in the film thickness seems to differ for resonant SHG-CD and off-resonant SHG-ORD, both show a saturation-type curve of g with increasing thickness.[67]

In contrast, we did not observe a steady development of g with layer thickness for Cysteine thin films. Instead, as depicted in fig. 4.5 at selected wavelengths and as an average over the full measured range ($470 - 680$ nm fundamental), g increases until around $300 - 500$ ML on both BS and FS supports with a maximum value of $g \pm 1$ (at 640 nm on BS and 520 nm fundamental wavelength on FS). Then, g decreases again leading to negative values of g for films thicker than 900 ML, at all wavelengths and the curve average as well. Whether the final value is reached at around $g \pm -0.75$ remains unclear since the thickest layers examined were of 900 and 1500 ML, respectively. Nevertheless, the non-linear development of g with thickness including even a change of sign has been shown clearly. Furthermore, this overall trend was observed for all the selected fundamental wavelengths of 490, 520, and 640 nm for both BS and FS supports and is represented by the average as well. However, g crosses

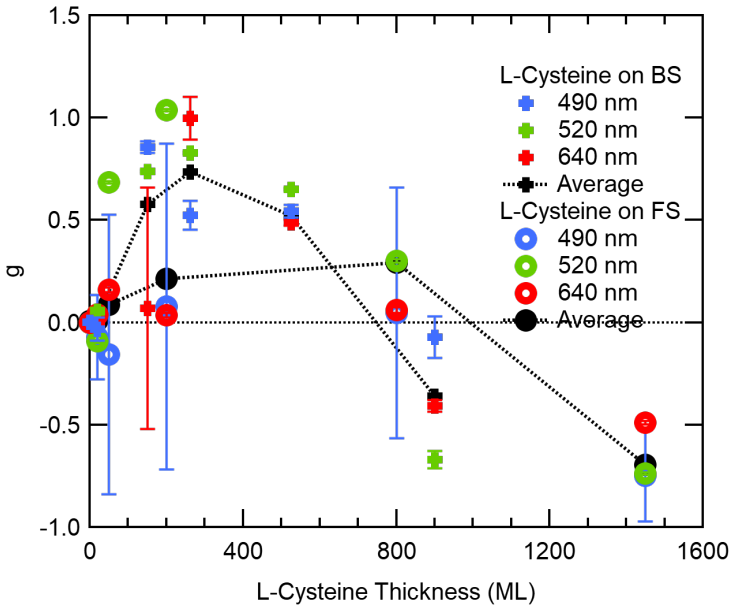

Figure 4.5.: SHG-CD at selected fundamental wavelengths with L-Cysteine thickness on FS and BS substrates.

zero with thinner layers for the BS in comparison to the FS support ($600 - 800$ *vs.* > 800 ML, respectively). For verification, this trend should be reproduced with the other enantiomer, D-Cysteine.

The interference pattern of the measurements on FS complicates this evaluation process for the samples also. With large standard errors, statements about g with increasing film thickness of L-Cysteine on FS should be classified as qualitative, especially at 490 nm fundamental wavelength. Thus, the average over the whole curve or around a transition of interest may be an indicator better suited for tracking the development with film thickness for FS supports, instead of single wavelengths.

Conclusions on Cysteine Thin Films on Oxide Supports

The chiral amino acid Cysteine is an intriguing candidate for chiral induction of gold nanoparticles. Therefore, Cysteine thin films of up to 1500 ML were deposited onto borosilicate (BS) and fused silica supports (FS), followed by examination with CD and SHG-CD spectroscopy.

We observed stronger scattering and SHG intensity from Cysteine on BS supports, even though being of thinner layer thickness than on FS, and assigned this to the surface quality of the support material. With the higher surface roughness of BS, both scattering and SHG become more pronounced with comparable film thickness. Furthermore, this means a stronger concentration of nucleation sites for film growth, potentially leading to more grain boundaries and increased surface roughness of the Cysteine layer itself.

Both in fundamental and non-linear CD spectroscopy, an interference pattern dominated the spectra of Cysteine on FS. In the fundamental case, the interference emerges from reflections at the interfaces, similar to the etalon effect, and are observed for BS supports as well. For the non-linear examination, SH generated at the support surface facing the light source is interfering with SHG from the other side. With BS absorbing this SH, the interference pattern was visible over the whole measurement range in the case of the transparent FS. Thus, FS supports may be suitable for linear CD determination of Cysteine thin films while complicating SHG-CD data interpretation at the same time.

Interestingly, the non-linear anisotropy factor g depends non-linearly on increasing layer thickness of L-Cysteine. After a maximum of $g \pm +0.75$ with layers around 300 ML for BS supports, g experiences a sign change over a large portion of the spectral range examined. This holds true for the average over the full measurement range, as well as measurement at single wavelengths selected depending on the observed bands in SHG spectroscopy. For FS supports, this trend was observed as well even though the data analysis being somewhat more complicated due to the interference effect.

Overall, Cysteine provides a plethora of potential orientation and binding modes onto a surface, also depending on the coverage and interactions with the support material. As a candidate as chiral inducer for Au NPs with moderate film thickness, the first ML of molecules will be chemisorbed to the gold surface atoms *via* the sulphur group, in an upstanding manner.[65,83,93,99]

4.3. Conclusions on Suitability of SHG-CD Spectroscopy for Model Catalyst Examination

In summary, the non-linear spectroscopic method SHG-CD was evaluated in terms of its suitability for investigations on model systems for asymmetric heterogeneous catalysis. Indeed, high sensitivity to structural details and molecular orientation were confirmed for the sophisticated method.

In the case of supported Au NPs, minute changes in the physico-chemical surrounding of the NPs were detected through the influence of a titania overcoat on the NP LSPR. Furthermore, a bimodal distribution in NP height was resolved thanks to the mode selectivity of SHG spectroscopy. In contrast, the amount of NP sizes and activity of all LSPR modes made any distinction of structural details impossible for the fundamental absorbance spectroscopy.

The investigations on Cysteine thin films revealed the dependence of the CD and SHG-CD response on the film thickness. Interestingly, a non-linear dependence was found in the case of SHG-CD. The use of fused silica (FS) and borosilicate glasses (BS) as support each have their own advantages and disadvantages, in respect to their optical windows and potential interference effects emerging for fundamental and non-linear spectroscopy. While Cysteine certainly provides a plethora of possible conformers that complicates analysis and interpretation, the molecule nevertheless appears as an intriguing candidate for chiral induction. This is due to the fact that Cysteine forms self-assembled ML on noble metal surfaces with defined molecular orientation (thiol group towards the metal atoms) at medium to high coverages. Since the chiroptical properties of Cysteine with different film thickness are known now for fundamental and non-linear CD and SHG-CD spectroscopy, the molecule was utilised as chiral inducer for supported Au NPs, see the following chapter.

5. Chiroptical Properties of Supported Gold Nanoparticles with Chiral Adsorbates

For the creation of a model system for asymmetric heterogeneous catalysis, we intend to mainly follow the strategy of asymmetrisation of an established heterogeneous catalyst through contact with a chiral inducer, as mentioned in chapter 1. For this, we search for a catalytically relevant model system that is comprised of a catalyst in the form of Au NPs in combination with a chiral adsorbate. The adsorbate in this picture can either be the chiral inducer for asymmetrisation of the catalyst, or additionally take part in a future reaction as well. Overall, the requirements of a suitable model system for our investigations in asymmetric heterogeneous catalysis for examination with SHG-CD comprise of the following:[3]

- Supported particles of materials and structures with catalytically relevant properties
- Resonance observable in SHG
- Spectrally resolved transitions of particles and chiral inducer
- ICD in particle resonance through interaction with chiral inducer
- Preservation of SHG signal with adsorption of chiral inducer
- Decent resistance against laser-induced damage

Plasmonic NPs and clusters, especially in combination with a dielectric, are routinely employed in catalysis and photocatalysis,[71,72,76–78] also see chapter 4.1 on page 23. Especially, supported clusters have drawn a lot of attention in this regard due to their size-dependent reactivity. Clusters with few atoms only are intriguing model systems for catalysis with

defined optical properties. Furthermore, calculations on these model systems are accessible without too excessive computational efforts. An introduction to cluster properties and characteristics can be found in ref. [6].

However, examinations of plasmonic Ag clusters with chiral adsorbates experienced SHG quenching, even for very small dosages of molecules.[3] One possible explanation includes the particles being symmetrically surrounded by the molecules. While this does not exclude a possible asymmetrisation of the particle itself, we turn blind to the chirality aspect when examining those model catalysts with SHG-CD due to the symmetry selection rules of the method. With a higher number of atoms, larger NPs provide a stronger optical response than clusters, which is traceable by mainstream spectroscopic techniques with standard sensitivity like fundamental absorbance and CD spectroscopy. This means, that even if the SH activity is lost due to symmetrisation through the chiral molecules, the presence of an ICD can still be investigated with fundamental CD spectroscopy in the case of NPs.

For the vast majority of samples investigated in the scope of this thesis, CD-activity was observed with fundamental CD spectroscopy, accompanied by an ICD around the LSPR in the case of plasmonic NPs. However, ICD has not yet been observed with SHG spectroscopy, either due to symmetrisation of the NP surrounding quenching SH generation or caused by laser damage suffered by the sample. The plethora of samples investigated for ICD includes a collection of supported Au NPs of various sizes and shapes in combination with Cysteine or Binol, thiol ligand-protected chiral Au clusters, chiral 2D perovskites, self-assembled monolayers of chiral allenes on Au/Ti thin films, and Binol thin films with protective silica overcoat. A comprehensive sample list with indications to CD and SHG-CD results can be found in the appendix on page 101.

Within this chapter, the most promising selection of supported Au NPs are presented in terms of their interactions with the chiral molecules Binol and Cysteine, sorted by relevance and potential for studying ICD in supported model catalysts. First, imprinted cylinders show ICD through interaction with Binol, unmistakably recorded by SHG-CD for the first time in our labs and to the best of our knowledge in the literature. Afterwards, porous and

solid hemispheres with Cysteine are compared in terms of SHG with different polarisations. Lastly, spheres with Cysteine highlight the search of a suitable model system providing the requirements mentioned above before a summary and outlook to the chapter.

5.1. Imprinted Gold Nanoparticles with Binol

Recently, a successful imprinting method for supported Au NPs onto oxide supports with high reproducibility over relatively large sample areas has been reported.[73] Through the lithography process, an interlayer between the NPs and the support can be incorporated and adjusted. Such an interlayer can increase adhesion of the NPs to the support. Furthermore, this leads to readily tunable LSPR of the NPs *via* the diameter of the NPs and appropriate choice of the interlayer. Thus, these NPs appear as intriguing candidates for investigations on ICD with an chiral inducer.

Binol and its derivatives are chiral compounds regularly used for asymmetric catalysis in the homogeneous phase.[100–102] The electronic transitions of Binol are energetically well separated from the LSPR of the present NPs, rendering Binol an ideal candidate as chiral inducer.

Nanoparticle Characteristics

Supported Au NPs were imprinted *via* lift-off nanoimprint lithography onto borosilicate BK7 supports, with an adhesive mixed titanium-titania interlayer following the procedure of Ref. [73]. The resulting NPs are of cylindrical shape with a diameter of (75 ± 1) nm and a total feature height of (20 ± 1) nm, of which (17 ± 1) nm are comprised of Au alone. Furthermore, the NPs show high order arrangement over mm-scale range while being well-separated.[73] Representative AFM and SEM images are shown in figs. 5.1A,B, accompanied by a schematic representation of the NP composition (fig. 5.1C).

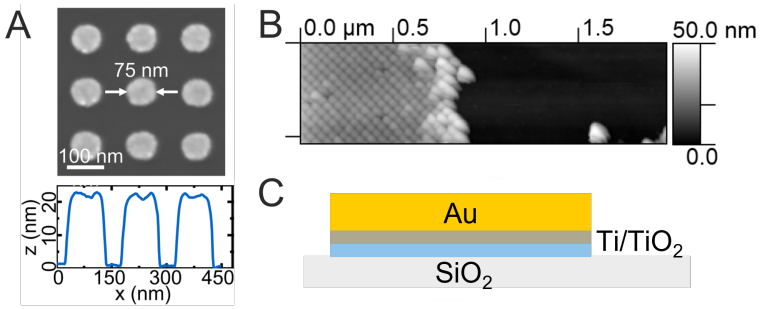

Figure 5.1.: Scanning electron microscopy image (A), atomic force microscopy image (B), and schematic of imprinted Au NPs (C). A reproduced with permission from ref. [73].

LSPR in Absorbance Spectroscopy

Fig. 5.2 shows the absorbance and CD spectra of supported Au NPs, bare and coated with 30 nm (42 ML) R- and S-Binol, respectively. The bare NPs have an LSPR band around 650 nm with a shoulder to shorter wavelengths and small interband absorption is visible around 450 nm and below. Thin Binol layers of 30 nm (42 ML) do not absorb in the examined wavelength range for both enantiomers. The combination of the NPs with 30 nm (42 ML) S-Binol shows an unaltered plasmon resonance position with slightly increased absorbance (bare and with S-Binol in fig. 5.2). The NPs covered with R-Binol were from another physical sample, thus the variation in plasmon band shape and position.

It is well known that the LSPR depends heavily on the physico-chemical surrounding that changes here with Binol deposition, see chapter 2. Since the effective refractive index increases with Binol deposition, a red-shift of the LSPR is expected, accompanied by stronger absorbance. With the NP shape, plasmon splitting is to be expected as well, i.e. into a mode perpendicular and a degenerate one parallel to the surface.[9,103] We have seen before that a bimodal or broad size distribution can also be accountable for disguising various plasmon modes through spectral overlap.[70] However, this seems improbable considering the narrow size distribution due to the sample preparation (fig. 5.1). Calculations on a simplified model of Au spheres, with different sizes corresponding to the NP dimensions, predict a smaller resonance energy for the longer LSPR mode (parallel to the surface) in comparison to the shorter one (perpendicular). Another relevant property influencing the LSPR is the NP

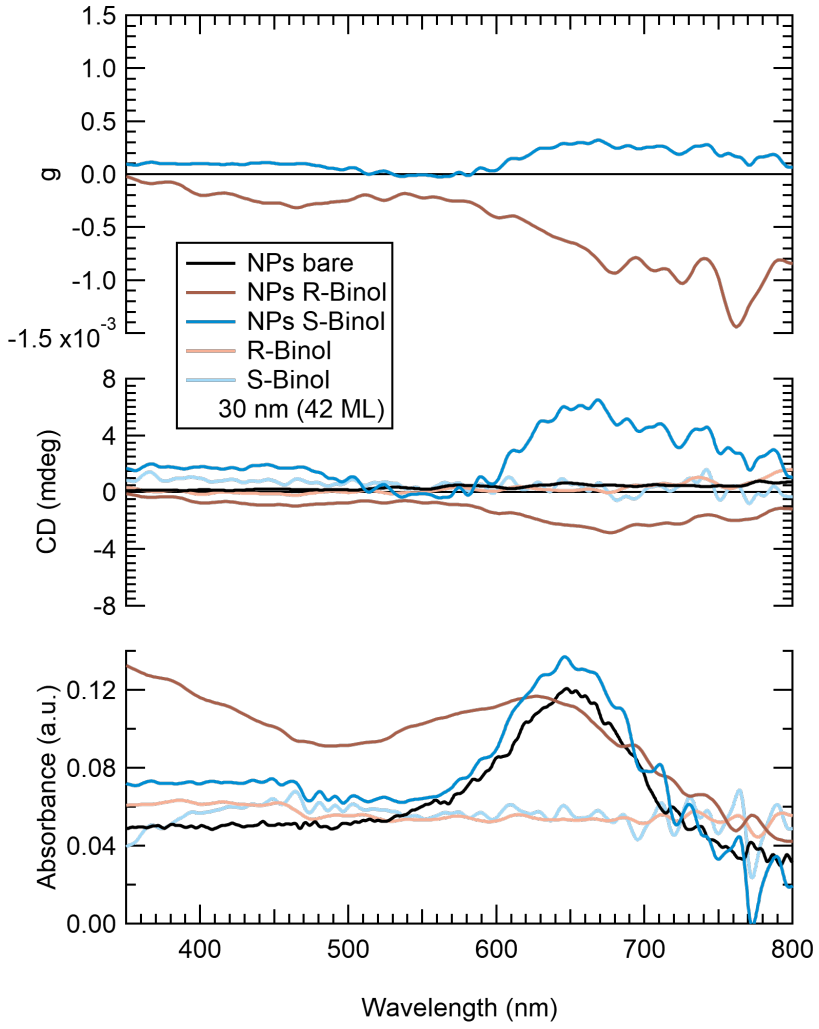

Figure 5.2.: Absorbance and CD spectra of imprinted Au NPs with adhesive titanium-titania interlayer on BK7, with 30 nm (42 ML) R- and S-Binol.

arrangement. However, with the distance between the NPs being slightly larger than the NP dimension itself (75 *vs.* 150 nm), the NP arrangement does not influence the LSPR in this case.[104]

Accordingly, the spectra of bare and covered NPs were fitted with two Gaussian curves each, representing the short and long LSPR modes. The shorter mode (perpendicular to the surface) was meanwhile fixed to the resonance obtained *via* SHG, vide infra. For the bare NPs, a peak position of 1.89 eV was found with a fixed resonance energy of 2.12 eV (655 and 585 nm), while the fit resulted in 1.90 and 2.16 eV in the case of NPs with Binol (653 and 574 nm). In both cases, the area under the Gaussian curves are in a ratio of around 1 : 2, as expected for the singly and doubly degenerate short and long modes, respectively. While the increase in absorbance follows the expectation from theory, the position of the Gaussian curves indicate a small blue-shift with Binol deposition. Taking into account the data quality especially in the case of SH, however, the ostensible blue-shift of 0.01 and 0.04 eV for the long and short LSPR, respectively, lies within the average fitting uncertainty of around $\pm$0.09 eV. With repeated measurements and an increased data quality, the red-shift predicted from theory may become resolvable.

Optical Activity and CD Spectroscopy

Regarding optical activity, the bare Au NPs show no CD signal, as expected from achiral substances (fig. 5.2). Since Binol does not absorb in the examined wavelength range, no CD is observable for the Binol thin films on BK7 accordingly. Furthermore, scattering and circular differential scattering are hardly present as well. However, the combination of both NPs with Binol shows a response at the plasmon band around 650 nm that is therefore attributable to the interaction of the particles with the chiral inducer. For the NPs with S-Binol, a mono-signate CD band between 600 and 750 nm has its extrema of $+$6.0 mdeg at the plasmon position around 650 nm. Additionally, optical activity is observable in the interband transitions around 450 nm with the same sign.

The NPs with the other enantiomer, R-Binol, show a CD response that follows the as-

mentioned trend. However, intensity and details in shape of the ICD vary between the two samples of NPs with R- and S-Binol, respectively. As already mentioned, the NPs are two physical samples with slight variation of the particle dimensions. These changes then lead to different interactions with the chiral inducer, determining the observed spectral details of ICD. Nevertheless, the curves are roughly in the shape of image and mirror-image, as expected for enantiomers, and the observed pattern becomes more evident from the anisotropy factor g. As already mentioned earlier in this chapter, similar to a variety of other systems, we observe decent ICD in the present system of imprinted Au NPs with Binol with fundamental CD spectroscopy (fig. 5.2).

LSPR in SHG Spectroscopy

Regarding the SHG spectra of the imprinted Au NPs (fig. 5.3), the NPs show a moderate SH intensity with a band around $270 - 310$ nm SH. According to the symmetry selection rules of SHG, the LSPR mode perpendicular to the surface is SH-active. In the present case, this is the shorter NP axis and thus corresponds to a higher resonance energy. Fitting with a Gaussian curve implies a maximum at 585 nm fundamental (2.12 eV; 293 nm SH), which has been used as the fixed resonance for LSPR fitting in the fundamental case (vide supra, fig. 5.2). Indeed, the LSPR mode observable with SHG (perpendicular) is blue-shifted in respect to the one parallel to the surface and also the entirety of modes (vide supra). Furthermore, with the observation of the LSPR around 650 nm in fundamental CD spectroscopy, the resonance mode is thus with the second harmonic here.

A thin Binol film of 30 nm (42 ML) shows low SHG (factor 0.5 in respect to the NPs) with no apparent bands. In contrast, the combination of NPs and 42 ML of R-Binol generates more SH than the bare NPs and Binol thin films (factor 3 and 6 in respect to NPs and Binol, respectively). Fitting resulted in an LSPR position of 574 nm fundamental (2.16 eV; 287 nm SH) for the perpendicular mode that is blue-shifted in respect to the ones parallel to the surface, as expected and as observed for the bare NPs before (fig. 5.2).

Comparing the bare and covered NPs, fitting implies a blue-shift of the LSPR through

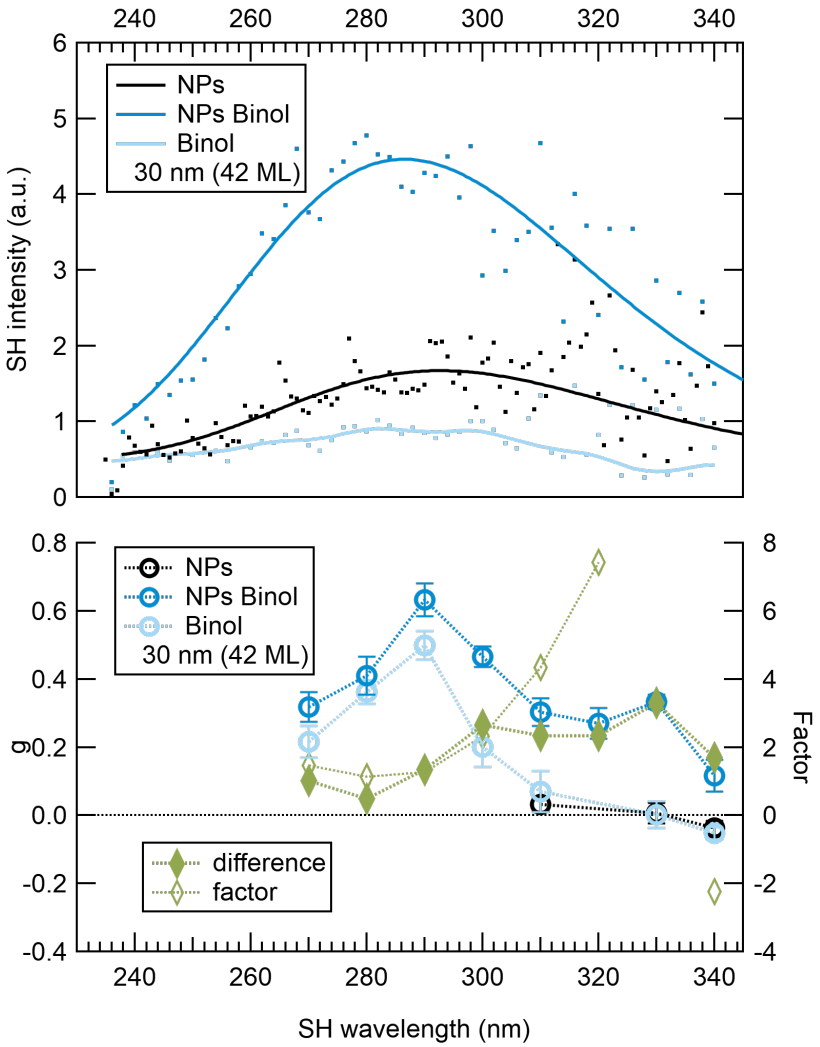

Figure 5.3.: SHG and SHG-CD spectra of imprinted Au NPs and 30 nm (42 ML) Binol.

interaction with Binol. With an increase of the effective refractive index, this contradicts the expectation from theory. As mentioned before, this ostensible blue-shift lies well within the fitting uncertainty, while the increase in intensity follows predictions from theory. With improved data quality, a red-shift and increase of the LSPR with increasing effective reflective index is resolvable with SHG spectroscopy, as already observed before in the case of supported hemispherical Au NPs with titania coating.[70]

Most importantly at this point, the particles do not experience SHG quenching, as commonly experienced for small metal particles with various adsorbates as summarised in ref. [3] and also observed during the cause in this thesis, see chapters 5(5.2,5.3) on page 37(50,59) and appendix page 101. This means, that a potential gradient complying to the symmetry selection rules for SHG remains for the present NPs, due to the adhesive titanium-titania interlayer between NP and support. However, the SHG was not only preserved but even increased for the imprinted NPs upon interaction with Binol. As already discussed, we expect an increase of the LSPR from theory due to the change of the effective refractive index upon Binol deposition. While this likely plays the key role for the observed change, other effects such as plasmon enhancement and molecular orientation should be taken into account as well.

In short, plasmonic NPs have the capacity of increasing the electric field strength close to their surface, especially at edges and corners.[105] As a result, transitions of molecules in close proximity are enhanced. This effect of plasmon field-enhancement finds a variety of applications, such as in surface-enhanced Raman spectroscopy and catalytic applications.[106,107] Since plasmon enhancement depends on the plasmon intensity, the fraction between the combined compounds and the molecules should follow the plasmon shape of the bare NPs itself. However, this is not the case here. Thus, while certainly being present, plasmon enhancement is not the main contribution to the increased intensity between NPs and the combination of both.

In the case of SHG, a reorientation of the molecules in such a way that its transitions have a larger projection perpendicular to the surface would lead to an increased SH intensity, in

comparison to the original orientation. With the different physico-chemical interfaces and the NP top and side being perpendicular surfaces, Binol must have a different average orientation on BK7 *vs.* on the NPs on BK7 (fig. 5.4A).

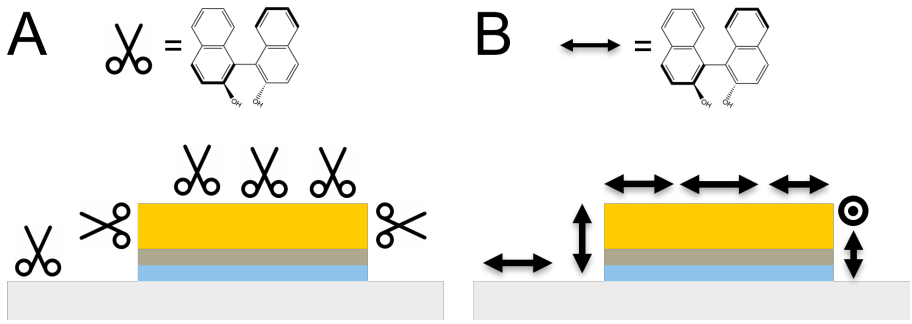

Figure 5.4.: Schematic of the preferred orientation of Binol with the hydroxyl group towards BK7 and the Au NPs (A) and transition dipole moment of the low-energy band (B).

Binol on BK7 has a preferred orientation with the hydroxyl groups to the oxide surface. With increasing coverage, the molecules will adapt a less ordered structure.[67] When considering the orientation of phenols on polycrystalline Au,[108] it is reasonable to assume a similar preference for Binol, which is with the hydroxyl groups towards the surface as well. Therefore, the first layer to first few layers of Binol will have a preferred orientation with the hydroxyl groups to the BK7 support and the top of the Au NPs. On the side of the NPs, Binol still interacts with the hydroxyl groups to the Au surface, meaning an orientation perpendicular to the other interfaces (fig. 5.4A). The transition SH-active for the side-orientation of Binol corresponds to the low energy band[61] and the main increase in SHG should accordingly happen above 300 nm. However, since this is not the observation here (fig. 5.3), reorientation of Binol is another minor player regarding the SH intensity increase. Nevertheless, we will come back to Binol orientation when discussing optical activity of these NPs.

Optical Activity and SHG-CD Spectroscopy

Chirality was already successfully detected with the current SHG-CD spectrometer for ML and even sub-ML Binol thin films.[66] With a rather small signal in comparison to the collected

number of laser pulses in the present case, increased statistics in terms of longer data collection can help in clarifying small differences in SHG intensities by lcp and rcp. Therefore, *time measurements* (TMs) at single wavelengths with about 50 times more laser pulses were conducted for the further examination of the potential asymmetric heterogeneous model catalyst comprised of Au NPs and chiral Binol molecules (fig. 5.3), for more details see chapter 3.2 on page 16.

Regarding the chirality of the present sample, the bare NPs show no optical activity around the LSPR band determined from fundamental absorbance ($310 - 340$ nm SH, fig. 5.2), as expected for an achiral sample. With a layer thickness of 30 nm (42 ML), the optical activity of the middle-energy band of Binol is already detectable. The overall g is positive with a maximum of $g = +0.5$ at 290 nm SH. Around the LSPR of the NPs, there is hardly any optical activity from Binol on BK7 (310 nm SH and above). In contrast, the anisotropy factor of the NPs with Binol is more positive than the one of Binol alone, over the whole examined spectral range. Also around the original LSPR position ($310 - 340$ nm SH), it remains clearly positive. While there are hardly contributions from Binol or the bare NPs in this spectral part, only the combination accounts for the observed $g \approx +0.3$. This follows strictly the definition of ICD from Binol to the NPs. Since plasmon enhancement and reorientation of Binol on the NP side have minor influences on the SH intensity, their effect on SHG-CD is evaluated as well.

Plasmon enhancement increases the intensity of both lcp and rcp in equal measures, e.g. a factor of 3 was observed for the increase in SH intensity earlier. Through the definition of g (see chapter 2.4 on page 12),

$$g' = 2\frac{3 \cdot I_{lcp} - 3 \cdot I_{rcp}}{3 \cdot I_{lcp} + 3 \cdot I_{rcp}} = 2\frac{3 \cdot (I_{lcp} - I_{rcp})}{3 \cdot (I_{lcp} + I_{rcp})} = g \tag{5.1}$$

where I_{lcp} and I_{rcp} stand for the SH generated by lcp and rcp radiation, respectively. In the end, the factor 3 can be removed from the fraction and one results in the definition of g itself, meaning that plasmon enhancement has no influence on g – plasmon enhancement leads to a ratio of 1 between g of the molecules and plasmon-enhanced molecules. However, the ratio

of g from Binol and the NPs with Binol ("factor" in fig. 5.3) does not equal 1 but is wavelength dependent. Therefore, the observed SHG-CD cannot stem from plasmon enhancement.

While being small, an influence from the Binol reorientation at the Au surface on the SHG intensity was discussed earlier. This reorientation becomes more relevant in terms of optical activity: the low-energy band of Binol has a drastically increased projection perpendicular to the BK7 surface due to orientation at the NP side and furthermore is in the same spectral region as the observed ICD (see also fig. 5.4B).

Heister *et al.*[67] examined the SHG-ORD and SHG intensity of Binol thin films on BK7 with increasing film thickness for the low energy band of Binol. With a layer thickness of 30 nm (42 ML, $4 \cdot 10^{15}$ molecules per cm^2), basically no SHG and SHG-ORD was observed,[67] indicating that the molecules inside the thin film did not (yet) experience much disordering. Additionally, from a publication by Weber *et al.*[66] and previous experiments in the scope of this thesis (see chapter 3.3, page 18), the SHG-CD spectra of Binol ML and sub-ML films are known for the three Binol bands observable below 240, around 280, and above 300 nm, respectively. A fully oriented Binol thin film of 2000 ML has an optical activity at 320 nm of $g = +1.25$ (ref. [66]). Lastly, we assume that each Binol molecule contributes individually to optical activity, depending on its orientation in respect to the surface normal of the BK7 support.

The NPs are completely embedded in the Binol layer. Now considering the surface areas of the interfaces [Binol–BK7 and Binol–NPs(top)] and Binol–NPs(side), it becomes clear that the side of the NPs only contributes to around 15.1 % of the total interface area with Binol. Then, this estimation on optical activity leads to $g_{est} = +0.0053$. In contrast, the observed ICD around 310-330 nm SH is $g_{exp} \approx +0.3$ (fig. 5.3), which is two orders of magnitude larger. This assessment is under the assumption that the first ML of Binol at the NP side-interface experiences the strongest ordering effect, while the contribution of the second ML already is negligible since it is dominated by the "bulk" orientation from the NP top and BK7. However, even with 3 ML of perfectly aligned Binol molecules taken into account, the simple model conservatively predicts $g_{est} = +0.016$. Furthermore, the molecules can – and will at least

partly – be ordered at the NP side without the low-energy band having a large projection perpendicular to the BK7 surface (fig. 5.4B). Thus, it can be confidently concluded that the observed optical activity of the NPs with Binol does not originate from Binol reorientation at the NP side alone. Instead, Binol orientation plays a minor role.

These two phenomena of plasmon enhancement and reorientation of Binol at the NP side may influence the SHG intensity, however, they are not responsible for the observed optical activity. The combination of Binol and NPs show a SHG-CD that is more than the sum of the individual contributions, which follows the definition of ICD. The effect can be grasped well from the "difference" curve between NPs–Binol and [NPs and Binol] in fig. 5.3. Thus, the Au NPs experience asymmetrisation through the interaction with Binol. This is the first case of ICD into supported Au NPs without protective coating successfully detected with SHG-CD without laser damage and under preservation of symmetry in our labs – and to the best of our knowledge also in the literature.

Conclusions on Imprinted Gold Nanoparticles with Binol

In summary, the supported Au NPs with adhesive titania-titanium mixed interlayer on BK7 showed a decent ICD at the LSPR and interband transitions through interaction with Binol in fundamental CD spectroscopy. The small effect was validated by examining both enantiomers R- and S-Binol, respectively.

For the nonlinear investigation, the LSPR not only remained detectable upon Binol deposition but an increased SHG efficiency was observed that we attribute to the change in physico-chemical surrounding. Thanks to the adhesive interlayer, the NPs were covered by the molecules only at the top and side and no laser damage was witnessed after investigation. Furthermore, an ICD around the LSPR was unmistakably observed with SHG-CD spectroscopy, for the first time in our labs and to the best of our knowledge in the scientific society as well. These results highlight the necessity of the strong interaction between the NPs and the support material.

With the process of asymmetric heterogeneous catalysis in mind, however, the chiral inducer

in the form of a 42 ML Binol thin film renders the accessibility of the asymmetric model catalyst difficult for approaching reactants. In the ideal case, chirality is induced from the support material, or the adhesive interlayer. This leaves the majority of the NP surface open for interactions with the substrate.

5.2. Closed and Porous Gold Nanoparticles with Cysteine

As already mentioned in chapter 4.1, we investigated catalytically relevant hemispherical Au NPs on BK7 upon an increasing titania overcoat,[70] to verify the suitability and sensitivity of SHG spectroscopy for the investigation of potential model systems in heterogeneous asymmetric catalysis. In terms of high reaction rates in heterogeneous catalysis, a large surface area of the catalyst may be advantageous, which can be achieved for example by means of porosity. Furthermore, optical activity has been shown for Au NPs with high surface area that were modified from a templated micelle-assisted growth.[109] Recently, a suitable theoretical model of the chirality of the NP surface and geometry successfully described the optical activity.[110]

The chiral amino acid Cysteine forms strong interactions with Au entities due to its thiol group, that can lead to rearrangement of surface details and atoms.[83,111,112] Playing the role of chiral inducer, induced CD has been commonly observed in semiconductor quantum dots,[39,113] Au(I) supra-molecules,[114] Au and Ag NPs,[22,84,88,115–117] and other systems in contact with Cysteine. Therefore, the interaction of supported porous Au NPs with Cysteine was examined, in comparison to the closed NP counterparts.

Nanoparticle Characteristics

Supported closed hemispherical Au NPs were prepared by thermal annealing of sputtered Au thin films on BK7 supports (analogously to chapter 4.1 on page 23). The porous NPs were prepared in a similar fashion but from a mixed Au-Ag thin film, and an etching step followed annealing for Ag removal. The resulting NPs are of various sizes and roundish shapes. An

impression of the NPs can be received from HeM and SEM images (fig. 5.5).

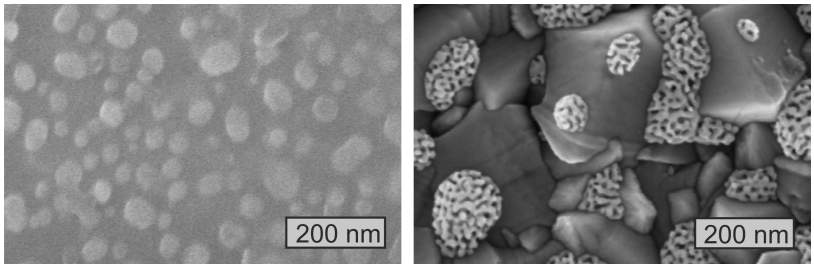

Figure 5.5.: He ion microscopy of closed hemispherical Au NPs on BK7 (left) and scanning electron microscopy of porous hemispherical Au NPs on ITO (right). Scale bar: 200 nm.

Fundamental Absorbance and CD Spectroscopy

Regarding the optical properties (fig. 5.6), the closed hemispherical NPs on BK7 have an LSPR band around 560 nm (2.20 eV) and interband transitions are visible below 450 nm. As determined before (chapter 4.1 on page 23), these NPs have a relatively broad size distribution that obscures the various contributions from different NP sizes and LSPR modes.[70] This complicates analysis of the LSPR tremendously. However, with the addition of 30 nm (60 ML) Cysteine, a red-shift of the LSPR to 590 and 600 nm (2.10 and 2.07 eV) and an increase in absorbance are clearly visible. Latter is also affecting the absorbance at the interband transitions. With an refractive index of $n \approx 1.5$ for Cysteine,[118] the observed change complies expectations from theory. The two physical samples used for D- and L-Cysteine show a small difference in the final LSPR position after deposition of Cysteine (0.10 and 0.13 eV shift).

In contrast, the porous NPs display a broad and intense LSPR band centred around 730 nm (1.70 eV), that probably consists of a combination of various LSPR modes and NP sizes as well. Furthermore, interband transitions are also observable. With Cysteine deposition, the LSPR experiences a strong blue-shift to around 590 and 640 nm (2.10 and 1.94 eV), respectively. The two physical samples with formerly very similar LSPR lead to a large variation in final LSPR position (0.40 and 0.24 eV shift). The nominal layer thickness of 30 nm (60 ML) of Cysteine suggests a saturation of the LSPR shift through the thick layer of dielectric around the NPs.[119] Considering the strong S-Au interactions,[83] however, the chiral molecules align with the thiol

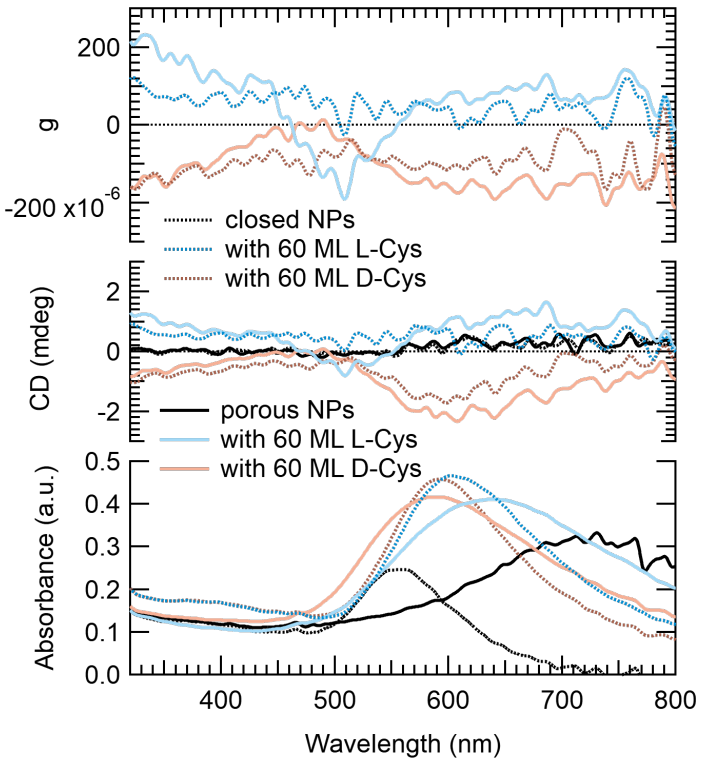

Figure 5.6.: Absorbance and CD spectra of closed and porous, hemispherical Au NPs on BK7 with 30 nm (60 ML) D- and L-Cysteine.

group towards the Au surface. Furthermore, Cysteine was deposited *via* thermal evaporation and a certain surface mobility shortly after deposition can be assumed. In the case of porous NPs, Cysteine may then cover the surface area inside the pores, in addition to the external NP surface. In total, more Cysteine is needed for the LSPR "saturation", depending on the surface area (or volume) of the pores, and the porous NP has a thinner layer of Cysteine surrounding than a closed NP of the same size. If now the physical samples show different average porosity of the NPs, the surrounding Cysteine shell has a different thickness meaning that the LSPR shift observed for porous NPs with Cysteine may converge with thicker Cysteine layers. Also, the broadness of the involved LSPR bands hints towards structural diversity as well. A change in LSPR intensity through molecule adsorption is unclear in this case, because only a part of the LSPR according to the bare porous NPs was recorded and thus the area under the curve remains unknown. However, the interband transitions do not experience a change in intensity what would be expected for the change in physico-chemical surrounding.

Regarding CD spectroscopy, the bare NPs (closed and porous) don't show any optical activity, as expected for the achiral samples (fig. 5.6). With 30 nm (60 ML) Cysteine, however, a small CD signal emerges around the LSPR (550-700 nm) that amounts to an extrema of -2 mdeg for D-Cysteine. The interband transitions around 450 nm are hardly affected while CD-activity with the same sign is observed at short wavelengths again (below 450 nm). Considering the thin films of Cysteine on oxide supports discussed earlier, latter can be explained by circular differential scattering (CDS) by Cysteine alone (see chapter 4.2, page 26). Since Cysteine does not have any transitions in the spectral range observed and the behaviour of the CD signal above 500 nm cannot be explained by CDS, the optical activity around the LSPR emerges solely from the interaction of Cysteine with the NPs, and thus is an ICD.

The closed NPs with the other enantiomer, L-Cysteine, result in a spectrum that is similar to a mirror-image, as expected. When considering the different LSPR positions for the porous NPs, the respective curve appears similar to a mirror-image as well but with a shift to longer wavelengths. Interestingly, the same sign is observed for one enantiomer on both closed and porous NPs. However, the ICD intensity for the porous NPs is generally smaller than for

the closed NPs, which could be influenced from structural properties or due to the smaller embedding of the NPs with nominal thickness as discussed before.

Another aspect that should be mentioned regarding the porous NPs in contact with Cysteine corresponds to changes in the sample with time. A freshly prepared sample with porous NPs and L-Cysteine has a more pronounced ICD being positive up to +6 mdeg around 500 nm and a zero-crossing at 600 nm, which is followed by a negative CD of −4 mdeg at 650 nm and above (see appendix, page 99). In contrast, the sample two weeks later shows the spectrum mentioned and shown above (fig. 5.6); this process thus includes a sign reversal around 600-700 nm. Also, the LSPR became narrower and slightly red-shifted in the course of two weeks. This again hints to structural changes within the NP sample in contact with the chiral inducer, such as crystallisation and ordering of Cysteine or large-scale rearrangement of Au atoms through Cysteine in the pores. Since such changes have not been observed in the case of closed NPs, an impact solely from Cysteine can be excluded. Overall, the temporal development of such samples, also in combination with microscopy remains to be investigated. Nevertheless, while being of small intensity and eventually showing time-dependence, an ICD for both closed and porous Au NPs in contact with Cysteine was observed.

SHG and SHG-CD Spectroscopy

The closed NPs show a strong SHG in a narrow band centred around 280 nm SH (560 nm fundamental), accompanied by a less pronounced shoulder around 310 nm SH (fig. 5.7A). For similar NPs,[70] we assigned the appearance of two SH-active LSPR modes to the existence of a bimodal distribution in particle height that is associated to incomplete annealing of the NPs during preparation (also see chapter 4.1 on page 23). Thus, a shoulder around 620 nm for fundamental absorbance can be resolved through SHG spectroscopy. This, however, also complicates the analysis by overlapping the various LSPR modes from different NP sizes. In comparison to the LSPR in fundamental absorbance, the intense SH band is basically at the same spectral position. For hemispherical particles, the shortest axis is the one perpendicular to the surface and the SH-active LSPR mode should thus have a higher resonance than the

entirety of modes (as recorded from fundamental absorbance). Nevertheless, fitting of the data may give corrections to the above impression from smoothed curves.

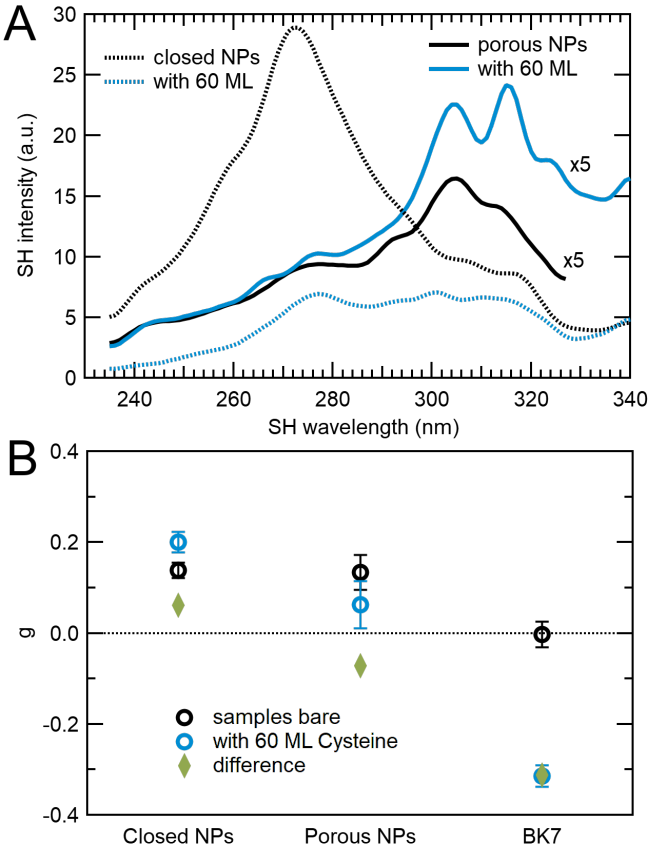

Figure 5.7.: SHG spectra (A) and SHG-CD at 280 nm SH (B) of closed and porous, hemispherical Au NPs on BK7 with 30 nm (60 ML) D-Cysteine.

Through the addition of Cysteine, less SH is generated by the closed NPs over the whole examined spectral range. Interestingly, the pronounced band around 280 nm experiences a stronger reduction than the one around 310 nm (factor 0.25 and 0.70, respectively). The refractive indices of BK7 and Cysteine in the examined spectral range are rather similar with $n_{BK7} = 1.520$ (ref. [120]) and $n_{Cysteine} = 1.51$ (ref. [118]) at 520 nm fundamental. Considering now the symmetry-selection rule for electronic transitions in SHG processes, the NPs experience a smaller gradient in the surrounding potential with the Cysteine layer. This effect should be even more pronounced for a higher film thickness surrounding the NPs, since

the effective index converges towards Cysteine in that case. The higher resonance energy corresponds to a shorter NP axis (flatter NPs) and with a constant thickness deposited, the flatter NPs are covered to a higher degree (fig. 5.7). While we observed this effect already with increasing titania film thickness on similar NPs,[70] the main observation is SH quenching through interaction with the molecules in the present case. Thus, the NPs experience a more symmetric surrounding as in the introduction to chapter 5 on page 37.

The porous NPs generate little SH with two implied bands around the same positions as for the closed NPs (280 and 310 nm SH). The intensity ratio between the two bands are reversed though, in comparison to the closed NPs (ratios 3 : 1 and 1 : 2, respectively). Unfortunately, the LSPR in SH corresponding to the maximum observed in the fundamental absorbance lies outside the examined spectral range ($350 - 400$ nm).

With deposition of Cysteine, the band around 310 nm increases slightly in intensity while the one around 280 nm remains indifferent in intensity. Nevertheless, the intensity in both cases is still lower than the closed NPs with Cysteine that experienced partial quenching (fig. 5.7A). A shift of the LSPR with change of the surrounding was not observed but can potentially be resolved with adequate fitting of the smoothed spectra.

As for the case of closed NPs, two SHG-active LSPRs are suggested from the spectra. However, the presence of a bimodal height distribution has been shown for the closed NPs, leading to the two resonances in SHG spectroscopy.[70] In contrast, a convolution of more resonances could make up the spectrum while other factors such as quadrupole contributions and variation in the physico-chemical surrounding may play an additional role, for the porous NPs. Accordingly, the number of SHG-active transitions remains unclear, especially without a comprehensible theoretical description of the fundamental optical properties.

The chiroptical properties with nonlinear spectroscopy were determined at a single wavelength close to the LSPR in the fundamental case of NPs with D-Cysteine (560 nm fundamental; 280 nm SH), see fig. 5.7B. The bare BK7 support has no optical activity, as expected for the achiral material. With D-Cysteine deposition of 30 nm (60 ML) film thickness, a shift to $g = -0.30$ is observed meaning that more SH is generated by rcp than lcp, also compare

chapter 4.2 on page 26 for L-Cysteine.

The achiral bare NPs both show a bias of $g = +0.15$ with unknown origin. Nevertheless, a relative change of g can be evaluated upon D-Cysteine deposition ("difference" in fig. 5.7B). For the porous NPs, a relative shift of $\Delta g = -0.1$ is observed which is the same tendency as for Cysteine on the BK7 support, however, less pronounced. In contrast, the closed NPs experience a slight increase by $\Delta g = +0.05$ with Cysteine deposition. With fundamental CD spectroscopy, a negative ICD was observed for both NPs. Considering the symmetry-selection rules for SHG-CD spectroscopy, this observation could give insights into NP geometric details and Cysteine–NP interactions, through the help of a decent LSPR model and knowledge on more NP characteristics like size distribution and porosity.

In summation, both closed and porous NPs show an altered optical activity upon Cysteine deposition that does not correspond to the sum of the individuals. This strictly follows the definition of ICD. With being a rather small effect, however, the ICD observed in SHG-CD should be verified through investigations with the other enantiomer. In the case of ICD, the use of L-Cysteine on the NPs must lead to the opposite shifts of g.

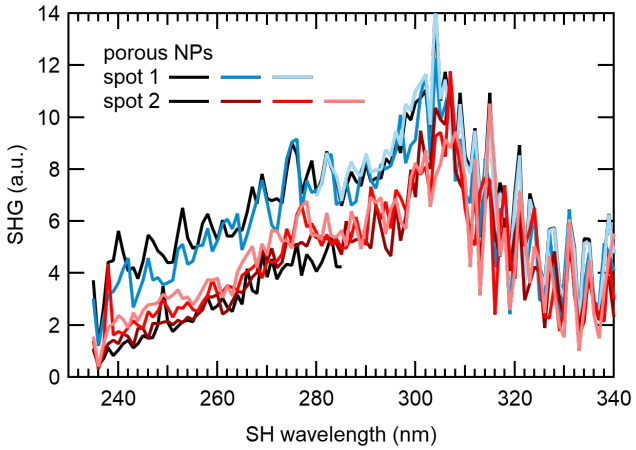

Figure 5.8.: SHG spectra of porous NPs repeated 3 and 4 times at two spots, respectively.

Another aspect that should be considered in laser spectroscopy regards sample damage. After the investigation, a small damage in the surface covered by the porous NPs was observed by eye. Nevertheless, repeated measurements at the same spot (fig. 5.8) for 3 or 4

times lead to unaltered spectra for the porous NPs. This suggests that the damage happens at the first contact of the NPs with the laser radiation, and the examined sample morphology may be altered due to interaction with the laser. Strategies for reduction of laser damage include reduced electromagnetic field strength at the surface decorated with NPs and reduced absorbance of radiation by the NPs, i.e. avoiding the most intense absorbance close to the LSPR maxima.

Conclusions on Closed and Porous Gold Nanoparticles with Cysteine

In summation, an ICD around the fundamental LSPR was observed for both closed and porous hemispherical Au NPs on BK7 with Cysteine, accompanied with a shift of the LSPR upon interaction. The ICD has the same sign for the interaction of closed and porous NPs with one enantiomer of Cysteine while the intensity of ICD is stronger for the closed NPs. Furthermore, the NPs with the two Cysteine enantiomers follow the principle of image and mirror-image.

In the nonlinear case, the closed NPs lost a large part of their SHG efficiency due to symmetrisation with the Cysteine layer. While showing less SHG efficiency to begin with, the SHG signal of the porous NPs remained unaltered through Cysteine deposition. Finally, a change in optical activity with SHG-CD spectroscopy was detected for both NPs upon interaction with Cysteine at a single wavelength close to the LSPR. Interestingly, the closed and porous NPs experienced an opposed shift in optical activity , in contrast to the fundamental. While being small, the ICD effect in SHG-CD can be validated by using the other Cysteine enantiomer. Also, a more thorough investigation over a broader part of the spectrum can help classify the observations and suggest an ICD mechanism. Nevertheless, measurement parameters should be optimised first, in order to minimise and then annul laser damage.

Overall, the porous NPs leave many questions open, especially in regards to geometry, porosity, and LSPR model. Here, the dependency of the LSPR and ICD with time could be examined in smaller increments and complementary microscopic methods can give insights into structure and potential rearrangement.

5.3. Spherical Gold Nanoparticles with Cysteine

Catalytically relevant Au NPs are an intriguing candidate for investigations with the aim of asymmetric heterogeneous catalysis. Furthermore, the chiral inducer Cysteine establishes strong interactions with Au due to the thiol group. A more detailed description and motivation of the choice of NP material and chiral inducer can be found in the introduction to chapter 5 on page 37, including chapters 5.1,5.2 as well as chapter 4.1, especially in the perspective of the requirements for potential asymmetric heterogeneous catalysts.

Another important factor when considering those requirements listed in the introduction to chapter 5 on page 37, is the complexity and availability of the NPs samples to be investigated. The NPs regarded in this chapter comprise a relatively simple system with straightforward sample preparation. They are of highly symmetric shape and show a low degree of ordered arrangement on the surface. Such LSPR-tunable surfaces are commonly used in surface-enhanced spectroscopy like fluorescence and surface-enhanced Raman spectroscopy (SERS), e.g. for investigations of biochemical compounds. With a broad field of applications, the NPs are readily available commercially, and were investigated in regards of ICD through contact with the chiral inducer Cysteine. The results from this project have also been summarised and discussed in refs. [121, 122].

Nanoparticle Characteristics

Au NPs on borosilicate supports (BS) were prepared by sputtering deposition according to refs. [68, 69]. Afterwards, L-Cysteine was deposited by thermal evaporation in consecutive steps with an accumulated thickness of up to 850 ML (425 nm). AFM images of the bare and Cysteine covered NPs reveal a relatively large NP size of around 400 nm in diameter and a close, unordered NP arrangement (fig. 5.9). Furthermore, the NPs give a similar impression before and after Cysteine deposition.

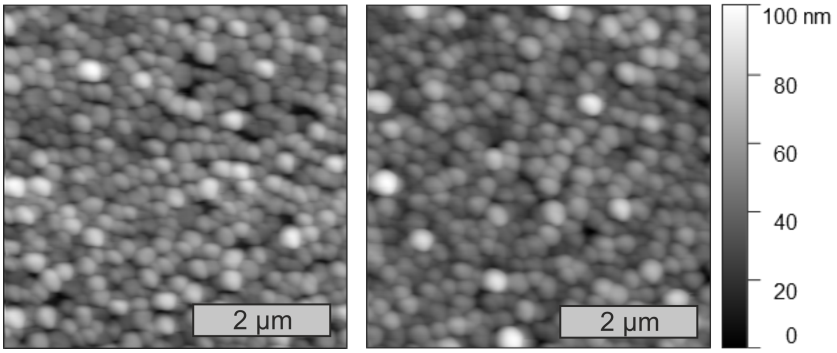

Figure 5.9.: Atomic force microscopy of spherical Au NPs on BS, bare (left) and with 180 ML (90 nm) L-Cysteine. Scale bars: 2 μm.

Fundamental Absorbance and CD Spectroscopy

The LSPR band of the bare NPs has a maximum around 575 nm and interband absorbance is visible below 500 nm (fig. 5.10). Given the tail towards longer wavelengths, the curve consists of a variety of LSPR modes, likely due to the NP size distribution as seen before for hemispherical supported Au NPs.[70] With 20 ML (10 nm) L-Cysteine, the LSPR shifts towards 650 nm and an increase in absorbance is observable. This follows the expectations for a change in the physico-chemical surrounding due to the Cysteine deposition, with a refractive index of $n_{Cysteine} \approx 1.5$ (ref. [118]). By further Cysteine deposition up to 850 ML (425 nm), no further shift of the LSPR band is observed. Nevertheless, scattering increases below 500 nm due to the Cysteine film, as seen for L-Cysteine without NPs on the BS support as well (fig. 5.10).

For the 850 ML (425 nm) Cysteine films, both with and without NPs, an interference pattern is visible in absorbance and CD. As mentioned already in chapter 4.2 on page 26, this interference stems from internal reflections at the air–sample and sample–sample interfaces along the beam path and is similar to the etalon effect.

Regarding the fundamental CD spectra, the bare NPs don't show any optical activity, as expected of achiral samples. Cysteine does not have any electronic transitions in the examined spectral range (also see chapter 4.2 on page 26). Nevertheless, a film of 850 ML (425 nm) of L-Cysteine on BS shows considerable scattering and circular differential scattering (CDS) with positive sign.

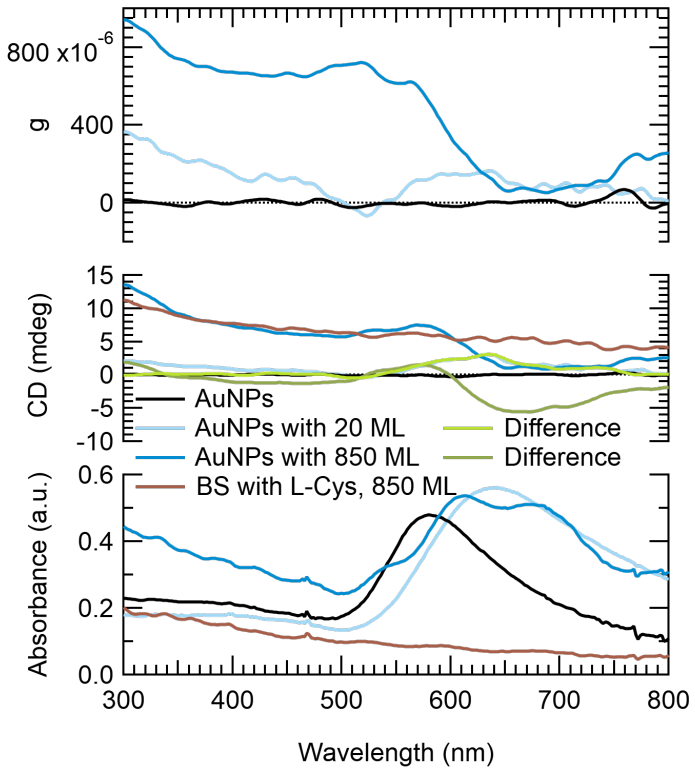

Figure 5.10.: Absorbance and CD spectra of spherical Au NPs on BS supports with L-Cysteine.

The combination of NPs with 850 ML (425 nm) of L-Cysteine show a similar chiroptical response as the Cysteine film alone. However, around the LSPR ($600 - 750$ nm), the CD curve is modulated in comparison to the Cysteine film that cannot be explained by CDS. Also, a small modulation of the CD response between the Cysteine alone and the combination with NPs is observable for the 20 ML Cysteine film ("difference" in fig. 5.10). However, the intensity is smaller for the thinner 20 ML film than the 850 ML film with $\Delta g = +3$ mdeg and $\Delta g = -5$ mdeg, respectively. In conclusion, the modulated optical activity around the LSPR emerges from the interaction of Cysteine with the NPs, and accordingly follows the definition of ICD. Interesting also is the change in sign of the ICD from the thinner to the thicker layer of L-Cysteine on the NPs. This sign reversal was also observed in SHG-CD for L-Cysteine layers on BS and fused silica supports, without NPs (chapter 4.2 on page 26). However, only the L-enantiomer of Cysteine was investigated in the present case. For a verification of the ICD from Cysteine into the spherical Au NPs, the D-enantiomer should be examined as well.

SHG and SHG-CD Spectroscopy

Moving on to the nonlinear optical response, the bare NPs generate a moderate amount of SH with a LSPR band centred around 270 nm SH (540 nm fundamental). This is blue-shifted in comparison to the fundamental absorbance (575 nm; shift of 0.14 eV), exceeding measurement uncertainties and eventual adjustment through revising the shift through LSPR fitting. Per definition, the axes of a spherical NP are of the same size and thus the LSPR for fundamental absorbance and SHG are expected at the same spectral position. However, arrangement of NPs is one important factor influencing the LSPR.[104] Considering the close spacing between the NPs (fig. 5.9), arrangement may indeed play a significant role for the LSPR. Nevertheless, the NPs are not ordered but randomly distributed over the surface. Alternatively, a slight deformation of the NP shape is reasonable due to the interaction with the support, that leads to the perpendicular NP axis being slightly shorter than the others and that may make up for the ostensible discrepancy in LSPR positions. As already discussed in chapter 4.2 on page 26, L-Cysteine on oxide supports shows medium to intense SHG with various underlying

resonances due to molecular orientation and transitions. In the case of a 100 ML (50 nm) film, the moderate SH generated is complemented by a maximum around 250 nm SH. In contrast, the thicker layer of 850 ML (425 nm) generates intense SH with a maximum around 310 nm SH.

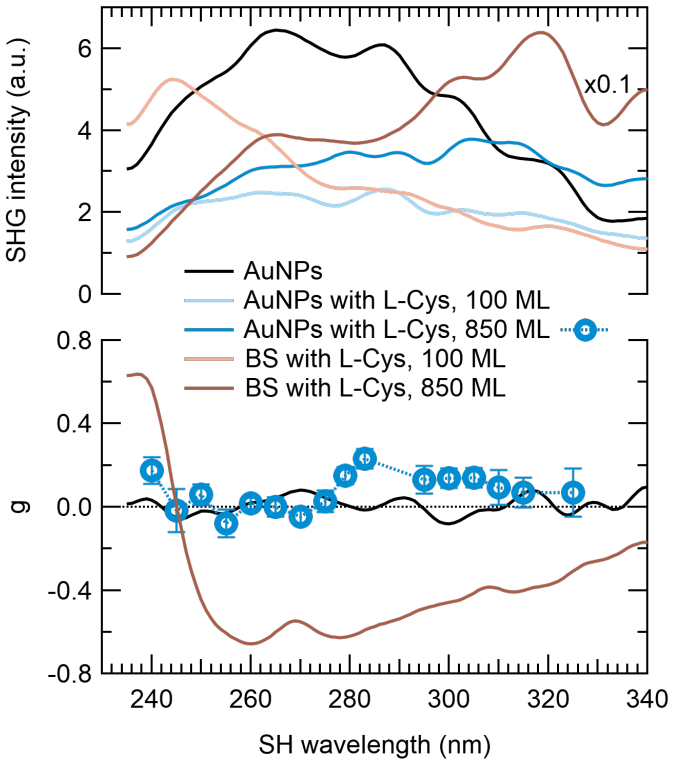

Figure 5.11.: SHG and SHG-CD spectra of spherical Au NPs on BS with L-Cysteine.

Now, the combination of NPs with 100 ML L-Cysteine film has a drastically reduced SHG intensity in comparison to the bare NPs (factor 0.3), obscuring the LSPR and without the maximum observed for L-Cysteine alone. Similarly, with a film thickness of 850 ML, the NPs give little SH, even though a small increase in intensity above 300 nm SH in comparison to the NPs with the thinner film suggests stronger contributions from the Cysteine film itself. One possible explanation for the loss of SH intensity lies with the similarity of refractive indices experienced by the NPs through the support and Cysteine layer: $n_{BK7} = 1.520$ (ref. [120]) and $n_{Cysteine} = 1.51$ (ref. [118]) at 520 nm fundamental. As discussed for the closed and porous

NPs with Cysteine before (chapter 5.2, page 50), the Cysteine layer on top of the NPs reduces the asymmetric potential perpendicular to the surface. Nevertheless, the SHG intensity is not fully lost in the present system of (close-to)-spherical Au NPs with L-Cysteine.

The bare NPs show no optical activity in SHG-CD (fig. 5.11), as observed in the fundamental case as well and as expected for the achiral NPs. In contrast, L-Cysteine on BS has a negative anisotropy factor over the majority of the examined spectral range with an extrema around 260 nm SH of $g = -0.7$ (also see chapter 4.2 on page 26). The combined system of NPs with 850 ML Cysteine was measured at individual wavelengths with a large number of laser shots for enhanced statistics due to the signal–noise ratio. The resulting curve suggests optical activity around $280 - 300$ nm SH (560-640 nm fundamental) of around $g \approx +0.2$. Interestingly, the observed CD-activity is positioned around the same spectral range, but of opposite sign as in the fundamental case. With the suggested ICD being a small effect, verification with the other enantiomer D-Cysteine is needed.

However, considering the sample morphology, for the NPs with a layer as thick as 850 ML L-Cysteine, effects of Cysteine itself should be readily seen in the SHG and SHG-CD spectra as well. Since this is not the case here, at least parts of the NP covered surface experiences laser damage and both NPs and Cysteine molecules desorb from the support. This is additionally witnessed by a reduction of fundamental absorbance caused by a large area scanning with the laser radiation (see appendix fig. A.2 on page 100), and puts the reduced SHG intensity in perspective. However, the fact that still parts of the LSPR and also optical activity can be detected with SHG and SHG-CD spectroscopy means that some of the material remains on the support. Nevertheless, the area where SH is generated experiences unknown and potentially extreme changes to the surface such as reconstructions and partial desorption, so that further investigations and interpretations of this system of supported spherical Au NPs with Cysteine appear intricate and speculative. Further comments on the NPs with Cysteine can be found in refs. [121, 122].

Conclusions on Spherical Gold Nanoparticles with Cysteine

In summary, a small ICD from L-Cysteine to the spherical Au NPs on BS was observed in fundamental CD spectroscopy, for each of the $20 - 850$ ML ($10 - 425$ nm) molecular thin films investigated. At the same time, the modulation in CD around the NP LSPR changes sign with increasing Cysteine deposition, as observed for Cysteine thin films on oxide supports earlier. The LSPR itself shifts upon Cysteine deposition as expected to higher wavelengths accompanied by an increase in absorbance. For layers of 850 ML (425 nm), interference patterns were observed due to internal reflection at the sample's interfaces.

The SHG spectra of the NPs were recorded. However, the NPs with Cysteine lost large parts of SHG efficiency, probably due to a combination of symmetrisation and laser damage, independent on Cysteine layer thickness. In contrast, L-Cysteine on BS generates intense SH with a distinct optical activity, see also chapter 4.2 on page 26. Nevertheless, the data suggests an ICD in SHG-CD with opposite sign in respect to the NPs with Cysteine in fundamental CD spectroscopy and Cysteine on BS. This should be verified with examinations on the other enantiomer, D-Cysteine.

However, strong laser damage to the sample, especially in the case of the NPs with Cysteine, renders interpretation speculative, see also refs. [121, 122]. This is partly due to the small SHG efficiency of the NPs with Cysteine and consequently increased electric field strengths for investigation. Overall, this project on spherical Au NPs on BS with L-Cysteine highlights the necessity of a strong interaction between NPs and support, to prevent symmetrisation of the potential experienced by the NPs at the surface. The strong interaction can additionally increase resistance against laser damage.

5.4. Conclusions and Outlook on Supported Gold Nanoparticles with Chiral Adsorbates

For the hemispherical closed and porous, as well as for the spherical supported Au NPs with Cysteine, an ICD around the LSPR was observed with fundamental CD spectroscopy.

Although the bare NPs generated a decent amount of SH, however, the SHG efficiency reduced greatly upon Cysteine deposition. At the same time, a different amount of SH was generated by lcp and rcp around the LSPR. Nevertheless, this suggested ICD remains ambiguous since verification with the other enantiomer is left to be investigated and laser damage plays a significant role, especially for the spherical NPs.

Similarly, an ICD was observed around the LSPR for the cylindrical imprinted Au NPs in combination with Binol with fundamental CD spectroscopy that was verified with both R- and S-Binol, respectively. In contrast to the other Au NPs, however, the imprinted NPs showed a clear increase in SHG efficiency upon Binol deposition attributable to a combination of plasmon enhancement and change of the physico-chemical surrounding. Most intriguingly, an ICD around the LSPR was determined with SHG-CD spectroscopy, for the first time in our labs and to the best of our knowledge in the scientific society as well. Since the ICD is independent on plasmon enhancement and orientation of the molecules at the NP surface, it originates from the physico-chemical interaction of the NPs with the chiral inducer. Consequently, this system serves as a proof-of-principle for the observation and further investigations of ICD in Au NPs with SHG-CD spectroscopy.

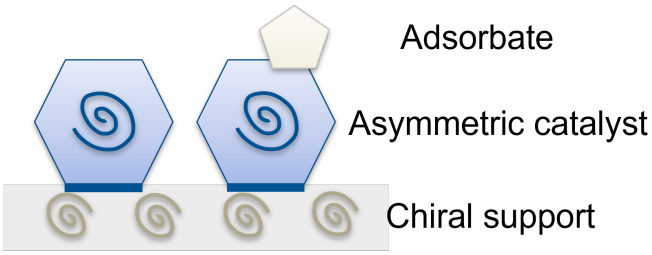

Figure 5.12.: Schematic illustration of the ideal model system for investigations on asymmetric heterogeneous catalysis, comprised of a catalyst with strong interactions to a chiral support material.

The outstanding characteristic of the imprinted Au NPs is the adhesive interlayer of mixed titania-titanium composition between NPs and BK7 support. This inhibits laser-induced damage to the NPs. At the same time, symmetrisation of the surrounding potential through diffusion of the molecules between NPs and support is annulled as well, preventing

SHG quenching. When conceptualising this interlayer, this is where strong metal–support interactions[123–125] between metal NPs or clusters and the oxide support come onto the stage.

Another aspect that should be considered for the investigation of asymmetric heterogeneous catalysis is the accessibility of the catalyst itself. The presented systems were conceptually built according to the same principle: a supported catalyst thoroughly covered with chiral inducer. The investigated films were of 30 ML or more. This, however, renders accessibility of the catalyst by an approaching substrate challenging since it must traverse the molecular film twice, before and after reaction. Consequently, in the ideal case, the supported catalyst has a strong interaction with the support – which additionally acts as chiral inducer, as schematically depicted in fig. 5.12.

6. Chirality Transfer and Induced Circular Dichroism in Other Systems

With our goal of spectroscopy with the aim of asymmetric heterogeneous catalysis, ICD is more a necessary tool rather than the ultimate goal. There have been tremendous efforts on ICD in various systems such as molecule-molecule and molecule-nanoparticle interactions. Similarly, scientists reported on structural chirality such as chiral assembly and ordering. At the same time, theoretical descriptions and models evolved that predict or explain the fundamental chiroptical phenomena observed. However, many aspects of ICD and chirality transfer are not well understood to date, also see chapter 2.2. In order to use ICD in the investigations of asymmetric homogeneous catalysts, it is important to understand the various mechanisms of ICD and chirality transfer. Our efforts presented in this chapter include investigations of the chirality transfer from a chiral ligand to the metal centre in a metal-organic, homogeneous asymmetric catalyst in solution and upon surface fixation. We introduced a new system for the asymmetrisation of dye molecules with the help of chiral gels with high molecular order, with a strong and reproducible ICD that is tunable by the choice of dyes and dye mixtures. In the new field of chiral perovskites, we presented new solvent-assisted synthetic routes that allow tunability of the chiroptical properties, a lead-free perovskite with polarised excited states that reach life times in the ns scale, and a new perovskite material that shows strong luminescence and an unusually high degree of polarisation in circularly polarised luminescence at room temperature. Finally, the effects on crystallisation and desorption on the chirality in Binol thin films are briefly summarised.

6.1. Optical Activity in Catalytically Active Chiral Pd Complexes

We concentrate our main efforts on the asymmetrisation of heterogeneous catalytic systems, see chapters 1 and 5. However, the far more common approach in order to achieve an asymmetric heterogeneous catalyst includes the fixation of asymmetric homogeneous catalysts onto an appropriate surface.[3] Pd is one of the common metals used for heterogeneous catalysis of hydrogenation reactions, but is was also proven as powerful catalyst in asymmetric homogeneous catalysis.[126–130] Similarly, Binap is a chiral ligand often used for enantioselective catalysis with high enantiomeric excess and decent selectivity.[100,102,131–133] In combination with Me ligands that can be used for surface fixation methods,[134] a complex of Pd^{II} with Binap and Me ligands appears as an intriguing candidate for such applications, accordingly. Furthermore, the catalytic activity of specifically [Pd(Binap)Me_2] has already been shown in the homogeneous phase with high enantioselectivity.[135] However, neither a synthetic route with satisfactory purity nor a thorough characterisation has been reported yet. This chapter is a summary of ref. [136] with additional results from ref. [137]. We show a new successful synthetic route with high purity and explore the nature of optical activity of the homogeneous catalyst.[136] Afterwards, [Pd(Binap)Me_2] is fixated onto a silica surface with preservation of optical activity.[137]

First, we found a successful new synthesis route with high purity for the target compound [Pd(Binap)Me_2] in order for thorough characterisation and subsequent surface fixation. Since we found quick degradation of the target compound to [Pd^0(Binap)$_2$] depending on the synthetic conditions, we followed a more unusual route by attaching Binap to [$PdCl_2(CH_3CN)_2$] (refs. [129, 131]) and subsequent methylation. The compound purity was assured by single-crystal X-ray diffraction (SC-XRD, fig. 6.1A) accompanied by ^{1}H- and ^{31}P-NMR and IR spectroscopy for both enantiomers of R- and S-[Pd(Binap)Me_2]. Also, the density functional theory (DFT) optimisation with B3LYP (LanL2DZ for Pd and 6–311++G* for residual atoms) resulted in structural parameters that show a deviation of $<5\%$ from the SC-XRD structure (fig. 6.1A). For the vast majority of parameters, the deviation even is below $<1\%$, such as

Pd-Me distance, angle between phenyl moieties, and more. Thus, already with the affordable computational expense, a certain similarity between the SC-XRD and DFT structures is present.[136]

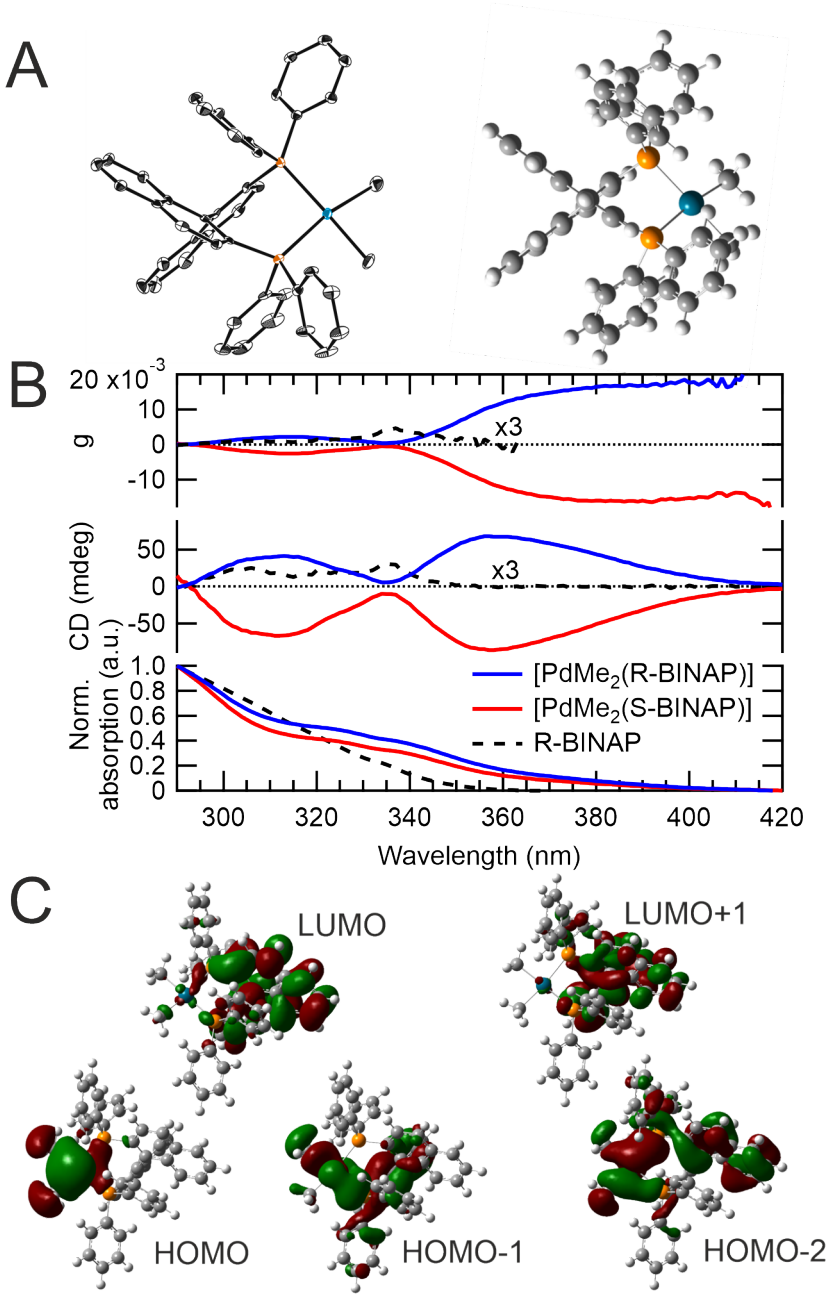

Figure 6.1.: SC-XRD and DFT-optimised structure (A), experimental CD spectra (B), and MOs with high occurrence (C) of [Pd(Binap)Me_2].[136]

Regarding the CD spectra of the target compound in toluol (fig. 6.1B), optical activity was observed with an additional band at higher wavelengths in comparison to Binap in solution. Now, the question arises whether this band is a band from Binap shifted due to the changed potential with Pd – or an ICD between Pd and Binap emerges. For asymmetric homogeneous catalysts, however, the question on the origin and nature of chirality and the mechanism of chirality transfer within the compound or between catalyst and substrate remains mainly neglected. In the current opinion, the role of the metal centre is ascribed to catalytic activity overall, while the chirality is introduced into the reaction by steric guidance of the substrate due to the sterically demanding Binap ligand. From a spectroscopic point of view, this can be assessed over the contributions of the Pd centre in the CD-active electronic transitions. While we don't have a suitable spectroscopic method at hand, DFT readily predicts electron density in terms of molecular orbitals (MOs) and their combinations for the molecular excitations. Furthermore, we observed a certain structural agreement between the SC-XRD and DFT structures. By examining the MOs and their crossings, the contributions of Pd in the relevant CD-active transitions that are composed of these MOs can be approximated.[136]

For the calculation of optical properties, 40 single-excited states were considered. As expected, the frontier orbitals play an important role in the various transitions (fig. 6.1C). While the unoccupied MOs generally are of π-type with strong contributions of the naphthyl moieties and small impact from the metal centre, occupied MOs are dominated by the metal centre with fewer contributions from the ligands. This applies especially for the frontier MOs with high occurrence and the Pd centre takes part in all relevant CD-active transitions. Also, for a second DFT optimisation that can be viewed as another conformer, the same observation as described becomes visible. Thus, DFT suggests that Pd indeed experiences ICD through contact with the chiral Binap ligand. Accordingly, Binap not only has steric influence for the approaching substrate during asymmetric homogeneous catalysis but also takes part in the electronic structure of the catalyst, so that the entirety of the complex is chiral. In addition to the steric contributions, such electronic properties and ICD should be taken into account for catalyst and ligand design.[136]

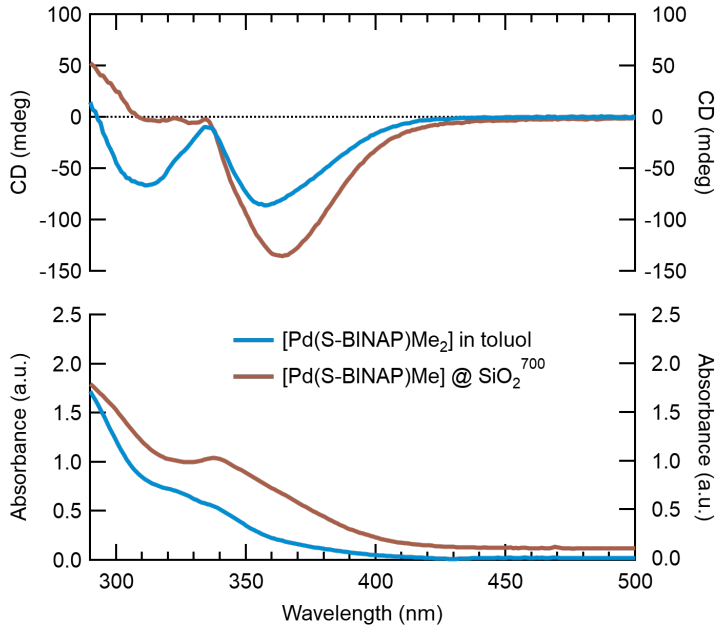

Figure 6.2.: Absorbance and CD spectra of [Pd(Binap)Me_2] and [Pd(Binap)Me]@SiO_2^{700}.

For the creation of the heterogeneous catalyst, [Pd(Binap)Me_2] can be fixated at a suitable surface. Following the protocol of ref. [134] that requires the presence of Me ligands, we successfully attached [Pd(Binap)Me_2] onto SiO_2^{700}, resulting in [Pd(Binap)Me]@SiO_2^{700}. The compound purity was assured with elemental analysis, IR spectroscopy, and solid state NMR spectroscopy and a catalyst loading of around 0.6 wt.% was found. For the catalyst in solution, two pronounced CD bands around 360 and 320 nm were observed. In contrast, the catalyst on the silica surface shows a band at 360 nm, with the same sign as in solution with a second feature suggested around 320 nm (fig. 6.2). Also, the intensity of absorbance and CD vary between solution and surface. Accordingly, the electronic structure and optical activity of the catalyst change due to the fixation process. Most importantly however, CD-activity is preserved for [Pd(Binap)Me_2] upon surface fixation so that asymmetric heterogeneous catalysis can be examined in further research.[137]

In conclusion, we presented a new successful synthetic route to the intriguing catalyst [Pd(Binap)Me_2] for asymmetric catalysis with high purity and verified its structure through SC-XRD. With limited computational resources, there already appeared a structural agreement

to DFT optimisations. During examination of the optical activity of the compound, the question arises whether the band around 360 nm is a shifted band of the chiral ligand Binap, or originates from the interaction of Binap with the Pd centre through ICD. Examining the MOs and their contribution to relevant CD-active transitions through DFT calculations, a strong contribution of the Pd centre was observed. This indicates that Pd indeed experiences ICD through the interaction with Binap. Thus, we recommend incorporating considerations of steric nature, but additionally electronic properties and ICD in the process of ligand and catalyst design.[136] For the creation of a asymmetric heterogeneous catalyst, we fixated the compound onto a silica surface. Upon fixation, the electronic structure was certainly altered. However, optical activity and chirality were nevertheless preserved. Subsequently, the catalyst can now be examined for reactivity, selectivity, and enantioselectivity in the terms of asymmetric heterogeneous catalysis.[137]

6.2. Tunable Induced Circular Dichroism in Gels

While our main focus for ICD lies on the aim of asymmetrisation of a heterogeneous catalyst, ICD can also be used as chiroptical method for the determination of details in structure and interaction, e.g. the absolute confirmation and configuration of chiral and achiral compounds.[138–140] Accordingly, ICD was suggested for applications in chiral sensing, data storage, drug delivery, optical materials, and more.[38,141–144] Especially for thin films of π-conjugated systems, a plethora of investigations was already performed. An overview on ICD in thin films can be found in ref. [145] while the contents of this chapter are a summary of ref. [146] and data as a part of ref. [122].

For a system of achiral laser dye Rhodamine 110 (Rh) and chiral Binol prepared by spin-coating, in earlier works from our group we found formation of J-aggregates by the dye. Depending on the Binol molar fraction, the formation of one enantiomer of the dye aggregates was enhanced over the other enantiomer, leading to optical activity in the thin films that is tunable in respect to the ICD intensity.[147] The ICD depends on the exact details in aggregate

structure and interaction between chiral host and achiral guest. However, spin-coating is a highly dynamic preparation process and depends on a variety of parameters. While external settings such as rotational speed and direction are easily controllable, the evaporation rate is an intricate interplay between position and amount of solution deposited and details of the spreading of the liquid.[148]

In the case of the Rh–Binol system, five nominally identical samples show the same absorbance curves. In contrast, a great variety of CD spectral features distinguishes the samples, such as intensity, ratio between the bands, and position of zero-crossing. Here, all controllable parameters such as spinning speed and time, volume and concentration of the coating solution, and support preparation were kept constant. Nevertheless, small details in average aggregate structure leads to low reproducibility for the CD data.[146]

One way for a stronger confinement in the interaction between chiral inducer and achiral molecule is with the help of gel fibres that provide a high order on the molecular level. The chiral gelator N,N'-dibenzoyl-L-Cystine (L-DBC) is commercially available while the synthetic route to its enantiomer (D-DBC) is known from literature. Due to gelation, the DBC molecules form stacks through hydrogen bonding that provide a regular and ordered environment for interaction with the achiral dye molecules.[146]

The DBC gel monomers as well as the gelated samples absorb in the UV and show CD-activity. The achiral dye molecules of Rh show absorption in the visible range without CD. In contrast, the combination of chiral gel with achiral dye leads to a pronounced ICD around the absorbance of the dye molecules (fig. 6.3). Since the ICD is mono-signate, aggregation of the dye molecules is not present. This suggests a direct ICD mechanism (electronic perturbation). The intensity of the ICD depends linearly on the dye concentration and g is constant with concentration while no change in shape of the ICD is observed. Also, microscopy images reveal that the dyes are located close to the gel fibres while the solvent in-between fibres is hardly coloured. A pronounced interaction between gel fibres and achiral dyes, without direct interaction of the dyes themselves, is possible with the dye molecules adsorbing individually at the cavity comprised of the phenyl groups along the gel backbone.[146]

Regarding the reproducibility, five gel samples of L-DBC with Rh show the same absorbance curves. Furthermore, the CD is alike in shape, intensity, and spectral position for the five samples showing sound reproducibility. With the other enantiomer D-DBC, identical absorbance appears while the CD behaves as an image–mirror image pair, as expected for enantiomers. Also, the same absorbance is observed for the racemic mixture while the CD is zero as expected.[146]

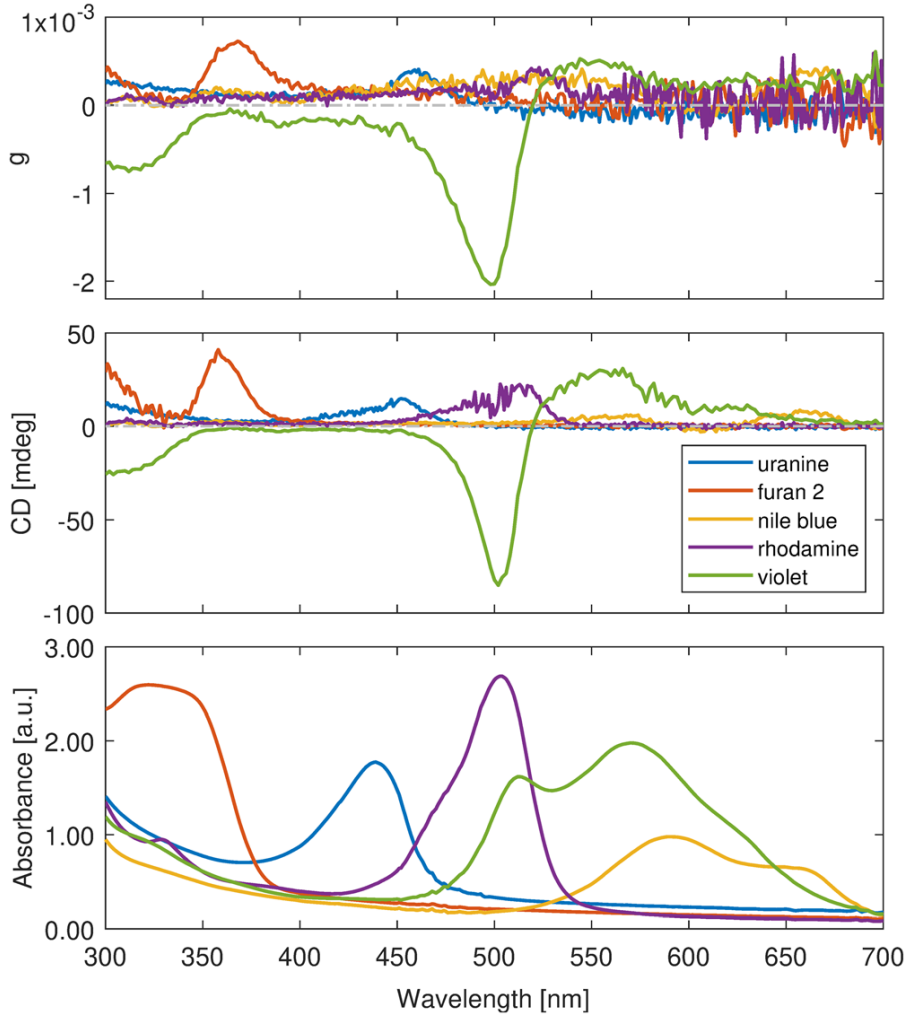

Figure 6.3.: ICD of achiral dye molecules (Uranine, Rhodamine 110, Cresyl Violet Perchlorate, and Nile Blue) embedded in chiral gel fibres of L-DBC. Ref. [146].

We exchanged the dye molecule with Furan 2 (absorption below 400 nm), Uranine (400 – 475 nm), Rhodamine 110 (Rh, 450 – 550 nm), Cresyl Violet Perchlorate (CVP, 475 – 650 nm),

and Nile Blue ($550 - 700\,\text{nm}$). In each case, we observed a pronounced ICD around the absorbance bands of the dye and image–mirror image behaviour is observed for the two gel enantiomers (fig. 6.3). With the supposition of one single dye molecule intercalated at the phenyl cavity without interactions to the next dye molecule, a combination of dyes should be a superposition of the individual spectra. For the duo mixture of Uranine–Rh and the trio mixture of Uranine–CVP–Nile Blue, the resulting spectra indeed showed a strong conformity with the mathematical addition of the individual dyes, both in absorbance and in CD. Overall, a highly reproducible ICD over a broad wavelength range can be created and tuned with these five dyes in combination with the chiral gel.[146]

While for the majority of dyes investigated no aggregation in the gelated samples is observed, CVP clearly shows an additional band when intercalated into enantiopure DBC gel. Additionally, the ICD is bi-signate and one order of magnitude larger that in the other dyes. All this hints towards aggregation of CVP in DBC. Since the additional absorbance band is blue-shifted, it can be associated to H-aggregation (head-head orientation). As the case for the other examined dyes, microscopy indicates accumulation at the gel fibres. However, the H-aggregate band of CVP vanishes for the racemic gel mixture meaning that the interaction of CVP with the enantiopure gel and with the racemic mixture is qualitatively different. With less order in the gel strand due to the different orientations of the phenyl moieties in the racemic gel, CVP aggregation is suppressed. These findings can be interpreted in such a way that CVP orderly intercalates at the phenyl moieties but still has strong interactions with the neighbouring molecule in the sense of aggregates.[146]

To back this hypothesis, we performed experiments of CVP with DBC monomers before gelation in aqueous solution.[122] Three spectroscopic species are discernible in solution, i.e. the dye monomer with absorbance maximum around 600 nm and two blue-shifted H-aggregate species. Now assuming a linear combination of the individual contributions, a set of linear equations approximates the individual spectra of each species. Due to different speeds of precipitation by the three species and varying concentrations, the ratio between the species could be varied. Consequently, the system of linear equations was solved and the CD spectra

of the individual species were obtained. While the monomer has basically no CD-activity, both H-aggregates show a pronounced bi-signate CD signal, that interestingly is close to a image–mirror image pair but with different intensity. The bi-signate nature of the ICD indicates an indirect mechanism (structural perturbation).[122]

In conclusion, we introduced a new system for ICD with defined and ordered interactions between chiral gel fibres of DBC and achiral dye molecules with high reproducibility. The dye molecules intercalate at the phenyl moieties of the gel backbone. Through exchange and addition of the dyes Furan 2, Rhodamine 110, Uranine, Cresyl Violet Perchlorate, and Nile Blue, the ICD is tunable and adjustable over the wide spectral range of $300 - 700\,\mathrm{nm}$. Nevertheless, with the appropriate dye choice this spectral range may be extended even further.[146] While the majority of dyes show the optical response of monomers, aggregation-like behaviour is observed for CVP with enantiopure gel fibres indicating that interactions across the gel phenyl cavities are possible for CVP. In contrast, no aggregation was observed for CVP in the racemic gel. Accordingly, the structure of the racemic gel fibres are in such a way that aggregation-like interactions between CVP molecules are not possible, meaning less structural order due to the arrangement of the phenyl moieties.[122] Now the determination of the racemic gel structure and simulations on the aggregates and dye–gel compounds come to the fore.

6.3. Chirality in Perovskite Thin Films

Perovskites are octahedra-based structures with general chemical formula ABX_3 and comprise a large group of crystalline inorganic or mixed organic-inorganic compounds. The relatively new scientific field of chiral perovskites is rapidly growing, promoted due to promising and intriguing applications of the compounds such as generation and detection of circular polarised luminescence (CPL), chirality induced spin-selectivity (CISS), spintronics, and ferroelectrics.[149–155] With the velocity of scientific progress within the field, review articles may not keep up to date of the developments. Nevertheless, refs. [155, 156] give an introduction to

the topic and its diversity, while this chapter aims for an overview over our contributions in the field.

The most straight-forward idea of a chiral perovskite lies within a chiral crystal structure meaning that the ions are ordered in a chiral fashion within the unit cell.[157] However, chirality can also be introduced through chiral adsorbates or ligands binding to the crystal surface. This corresponds to an ICD mechanism with structure perturbation while most often electronic interactions are present as well.[158] Furthermore, there exist more complex compounds and meta-materials, e.g. the integration of an achiral perovskite into a chiral polymer matrix that produces CPL.[159]

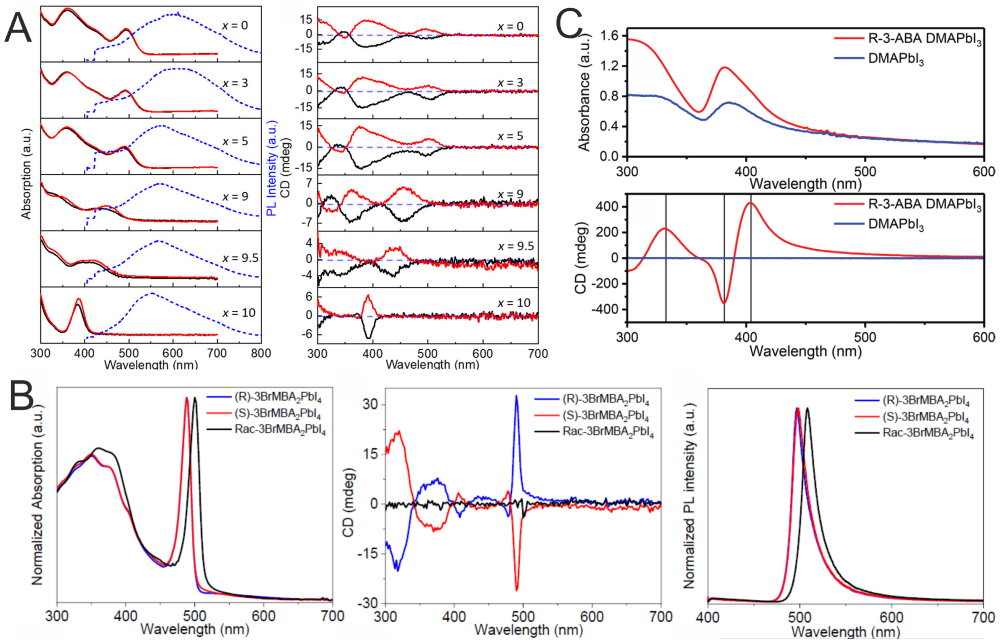

Figure 6.4.: Chirality in perovskite thin films: band gap tunability through halogen ratio (A),[160] strong luminescence with high CPL (B),[161] and ICD through incorporation of amino acids (C).[162]

We suggested the thin films of a Bi-based lead-free 0D perovskite for application in spintronics due to the lifetime of chiral excited states.[160] With $x = 10$, (R/S)-$CHEA_4Bi_2Br_xI_{10-x}$ exhibits only Br as halogen ion. The exciton absorption band is located around 385 nm and the compound accordingly appears yellow to the eye (fig. 6.4A). In the case of I halogen ions ($x = 0$), exciton absorption is present at 495 nm and an additional band-to-band absorption

feature appears around 360 nm. Furthermore, the band gap is tunable continually between these two extrema through adjustment of the halogen ion ratio. Importantly, we observe unusually long inherent spin polarisation relaxation lifetimes of the excited states that reach the ns time scale. Thus, this band-gap tunable system appears as promising candidate for next-generation spintronics.[160]

For applications such as CPL, the amount of luminescence but also the degree of polarisation of the emission is important. For a lead-halide 2D perovskite (R/S/Rac)-BrMBA$_2$PbI$_4$ with chiral crystal structure, we found both unusually high photo-luminescence quantum efficiency and degree of polarisation, already at room temperature.[161] The efficiency is as high as 40 %. Also, the excited states show a difference in life-time in dependence on the spin state. Therefore, the compound follows different relaxation mechanisms (i.e. radiant *vs.* non-radiant) for the different spins which ultimately leads to the strong polarisation in CPL of over 50 % (fig. 6.4B). Hence, we show that the polarisation degree of CPL originates not only from a different amount of absorbance of circular polarisations (CD) but is influenced by the relaxation mechanism as well.[161]

Another important factor for the application of new sophisticated materials is the ease and efficiency of preparation. For the hybrid lead-halide 1D semiconductor DMAPbI$_3$ with the amino acid 3-ABA, we found a strong ICD that is readily tunable through details in the thin film fabrication process, such as spin-coating parameters and content of chiral adsorbate.[162] Similar to the case of chiral organic thin films, we observed achiral contributions to the CD response that obscure the intrinsic CD of the compound. Therefore, the different contributions were disentangled with an approach based on Mueller-matrices. However, this aspect is regularly neglected in the field of chiral perovskite thin films. Importantly for the preparation complexity, the spin-coated compounds are accessible directly from the ligands and nanocrystals, without prior colloid formation. Furthermore, this is the first report on ICD due to amino acids in thin film perovskites (fig. 6.4C), to the best of our knowledge.[162]

In conclusion, the new scientific field of chiral perovskites is rapidly growing and many compounds with promising properties have been reported to date. With our publications,

we contribute in terms of new materials and systems, tunability of the band gab and optical activity, chirality transfer and life-time of polarised states, efficiency of circular polarised luminescence and relaxation mechanisms, and ease of preparation of such perovskite thin films.

6.4. Chirality in Binol Thin Films

The chiral molecule Binol and its derivatives are commonly used for asymmetric catalysis and other applications of chirality, as mentioned before. However, the optical activity and structure of Binol in the solid phase such as thin films still leaves room for further investigations.[49] This chapter summarises our contributions to understanding the non-linear optical activity of Binol thin films under sample ageing and laser illumination (refs. [163, 164]). Mortaheb *et al.*[165] radiated racemic Binol thin films with circularly polarised light that led to partial desorption of the molecules. Afterwards, significant non-linear optical activity (SHG-CD) was observed at the treated positions. The sign of the SHG-CD response depended on lcp and rcp during desorption, respectively, and the resulting curves showed image–mirror image behaviour, as expected for enantiomers. In contrast, the thin films showed no SHG-CD when lp was used for desorption, as for the combination of achiral molecules with lcp or rcp for desorption. The authors conclude with a phenomenological model that includes different desorption rates for the Binol enantiomers through two-photon-absorption when they interact with lcp and rcp, respectively. Importantly, both thermal and quantum-mechanical contributions are responsible for the desorption rates.[165]

In an attempt in "Understanding laser desorption with circularly polarized light" (ref. [163]), we consecutively examined the crystallisation process of the Binol thin films through surface roughness measurements, polarisation resolved microscopy, SHG-CD, and more. Especially, the influence of the crystallisation state on the optical response in terms of SHG-CD signal lay within the scientific focus (fig. 6.5A), before and after desorption.[163] For fundamental CD spectroscopy, it is known that chirality at the surface does not necessarily come from

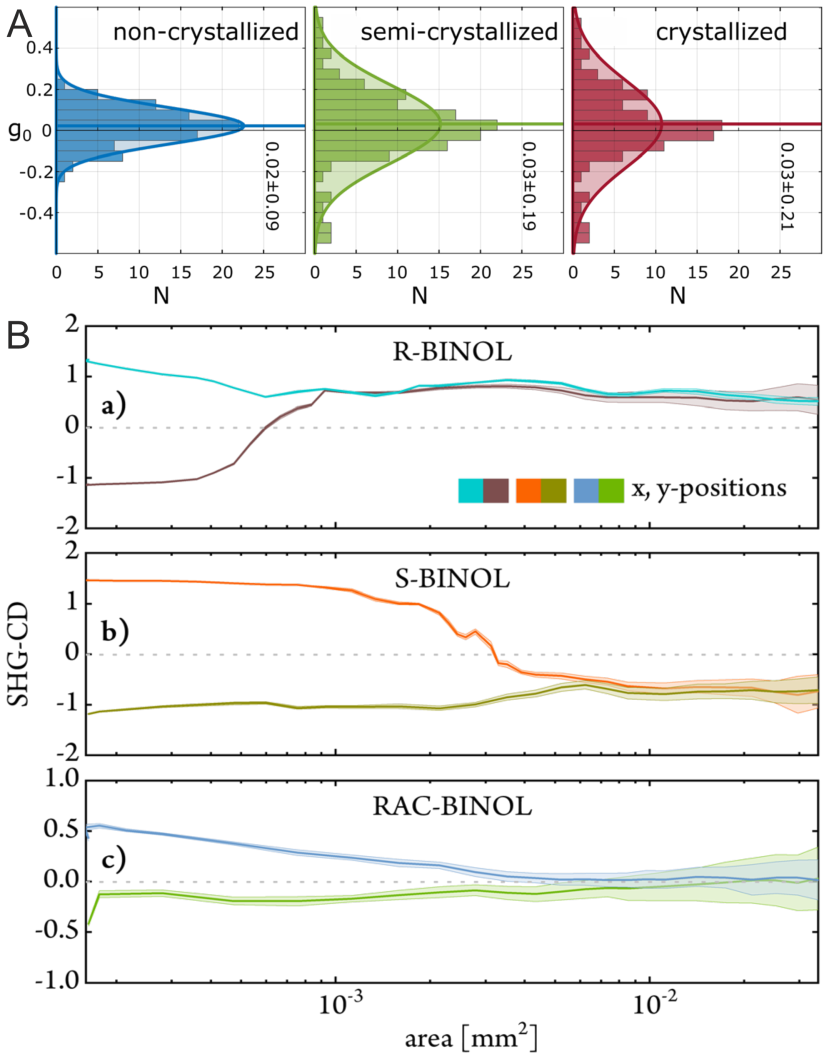

Figure 6.5.: Chirality in Binol thin films: effect of crystallisation state on SHG-CD of racemic films (A),[163] and effect of sampling area on SHG-CD of enantiopure and racemic films (B).[164]

an excess of one enantiomer as it can also originate from chiral superstructures and other structural effects (see chapter 2.2). Also, SHG-CD on thin films not necessarily gives the signal expected from the enantiomer excess present since we observed different anisotropy factors g in dependence on the desorption process but also sample age.[163]

The optical activity in crystallised Binol thin films depends also on the local structure. For one Binol enantiomer, an SHG-CD between $g = -1.0$ and $g = +1.5$ can be observed by merely changing the sampled area within a crystallite.[49] Thus, also the sampling area and position in respect to the crystallite size and arrangement is of importance when considering chirality at the surface. For the Binol thin films, we found that an anisotropy factor representative for the whole sample can be investigated with a large beam.[164] In contrast, smaller sampling areas lead to probing of local chirality (fig. 6.5B). As previously observed for organic thin films in the case of fundamental CD, the SHG-CD response additionally depends on sample orientation that can be altered by flipping and rotation along the beam direction. In this specific case, the SHG-CD response was reversed upon flipping while no effect from out-of-plane angles were observed. Even though the theoretical description according to Mueller-matrices is not fully understood in the non-linear regime, we were able to disentangle chiral and achiral susceptibility tensor elements and contributions for crystallised Binol thin films.[164]

While we broadened our knowledge on optical activity of Binol thin films in regards to structure, crystallisation, and effects from illumination and desorption, a hard proof of circular differential desorption is the verification of the enantiomeric excess of the desorbed molecules. This may be achieved with a sophisticated setup that is both capable of the desorption process, SHG-CD for surface analysis and circular dichroism in resonance-enhanced multiphoton ionization (CD-REMPI) for gas-phase analysis.

7. Conclusions and Outlook

In summation, we aim for the creation of an asymmetric heterogeneous catalyst *via* asymmetrisation of a heterogeneous catalyst in the form of supported NPs through interaction with a chiral inducer such as adsorbed molecules. For the study of such materials, the chirality transfer or ICD between the two entities is of special interest, that requires the use of appropriate chiroptical methods with high sensitivity to chirality and small changes of the nanostructures. Additionally, an adequate model system with pronounced ICD and catalytic relevance is needed for the investigation. This work presents efforts in those two requirements for the detection of ICD between supported noble metal NPs and chiral adsorbates with the aim of spectroscopy for asymmetric heterogeneous catalysis (chapters 4,5). The investigations are complimented by experiments in various other systems in order to gain a broader understanding of ICD effects (chapter 6).

First, the non-linear method of SHG-CD was validated in terms of structural details regarding supported Au NPs (chapter 4.1). It was found that SHG indeed is capable of detecting structural details and nm-scale changes in the physico-chemical surrounding of the NPs. The investigation of the NP LSPR determined the interaction between the NPs with a titania overcoat with increasing thickness. Accordingly, a coating model was proposed that includes coverage of the oxide support and low-coordination sites of the NPs for the first few nm of coating, while full encapsulation of the NPs by titania happens only with higher coverage. Furthermore, a bimodal height distribution of the NPs was revealed through wavelength-dependent SHG spectroscopy, due to the surface-sensitivity and mode-selectivity of the non-linear method.

For molecules as candidates for chirality induction, the reordering of chiral molecules within thin films with increasing thickness was successfully examined with SHG-CD for Binol and Cysteine (chapter 4.2). With increasing Cysteine layer thickness, the SHG intensity increased tremendously. Additionally, two SHG-active bands of Cysteine were observed. Depending on the average orientation of the molecules throughout the film, the ratio between these two bands could be varied. Regarding the non-linear optical activity of these films investigated with SHG-CD, with increasing film thickness a stronger optical activity was observed over the spectral range investigated. Interestingly, a sing-change of g appeared for very thick Cysteine layers that correlates to molecular orientation and the projection of the transition dipole moments perpendicular to the surface. For Binol, qualitatively the same observations are applicable, i.e. an orientation dependent SHG and SHG-CD response, ultimately adjustable over the average orientation of the molecules and their transition dipole moments that depends on the film thickness (chapter 3.3 and refs. [66, 67]).

Second, a plethora of supported Au NPs of different size and shape as potential asymmetric heterogeneous catalysts were investigated when in contact to potential chiral inducers such as Binol and Cysteine (chapter 5). In order to investigate these model catalyst systems with SHG-CD, the NPs must fulfil a variety of prerequisites that include, but are not limited to, a decent ICD between NP and chiral inducer, spectrally well-separated resonances of NPs and chiral inducer, and most importantly, preservation of the SHG-CD response during adsorption of the chiral inducer. For all investigated NPs an ICD in the fundamental case was observed. However, in most cases, the SHG-CD response was lost either due to laser damage or symmetrisation of NP surrounding by alignment of the molecules on the NP surface.

Nevertheless, the imprinted Au NPs stood out from the total collection of supported Au NPs investigated during the course of this thesis (chapter 5.1). Apart from the strong chiroptical response in the fundamental case, an ICD between supported Au NPs and a chiral molecule was also detected unambiguously by SHG-CD, for the first time to the best of our knowledge. This was possible because the mixed titania-titanium interlayer between NPs and BK7 support has adhesive properties, reducing laser-induced damage to the sample. Most

importantly, the symmetrisation of the NP surrounding is also inhibited through the adhesive interlayer. Accordingly, we observed an SHG intensity increase as expected from theory upon the deposition of Binol onto the NPs. Furthermore, the ICD was successfully validated with the non-linear method.

Originally, Au NPs were examined because of the interesting and easily tunable optical properties including a strong optical response due to the NP size, accompanied with the relevance in catalysis (chapter 5.4). Nevertheless, supported metal clusters that are comprised of few atoms only have proven suitable as model systems for heterogeneous catalysis, both through experiments and calculations. With a small overall optical response of the supported clusters, the sensitivity of SHG-CD can be used to its full potential. Furthermore, strong metal–support interactions become even more important for inhibiting the symmetrisation of the particle surrounding through evenly distribution of the adsorbate.

Another issue that should be addressed in the scope of catalysis is the accessibility of the catalyst. During this thesis, the main objective was the observation and investigation of an ICD that was achieved by adsorption of chiral inducer on top of the supported NPs. Accordingly, the NPs were thoroughly covered with 42 ML of chiral inducer and more. In regards to the accessibility of the catalyst, the chiral inducer in the form of a support materials appears as a better option than molecular thin films on top of the NPs.

In combination with the adhesive interlayer, an ideal chiral support can be achieved for example by a chiral template in the form of an evaporated Binol thin film, that is covered by a thin oxide layer through ALD for separation of the molecules from the clusters. Finally, titanium deposition onto the oxide overcoat leads to the adhesive and protective interlayer for strong metal–support interactions. Such a support material can then be used for deposition of clusters directly, and complementary experiments with larger NPs may be performed by micelle-assisted NP growth directly at the surface. If ICD is observed and the SHG from the NPs is preserved, the catalytic properties with focus on the enantioselectivity can be examined within this system.

Bibliography

(1) *Handbook of asymmetric heterogeneous catalysis*; Ding, K., Ed.; Wiley-VCH Verl.: Weinheim, 2008.

(2) Heitbaum, M.; Glorius, F.; Escher, I. *Angew. Chem. Int. Ed.* **2006**, *45*, 4732–4762.

(3) Kartouzian, A. *Chirality* **2019**, 641–657.

(4) Schrader, I.; Neumann, S.; Šulce, A.; Schmidt, F.; Azov, V.; Kunz, S. *ACS Catalysis* **2017**, *7*, 3979–3987.

(5) Cao, G.; Wang, Y., *Nanostructures and nanomaterials: Synthesis, properties, and applications*, Second edition; World Scientific Series In Nanoscience And Nanotechnology, Vol. Volume 2; World Scientific: Hackensack, New Jersey, 2011, %5Curl%7Bhttps://ebookcentral.proquest.com/lib/kxp/detail.action?docID=5227135%7D.

(6) *Nanocatalysis: With 14 tables*, 1. ed., 2. print; Heiz, U., Landman, U., Eds.; Nanoscience and technology; Springer: Berlin, Heidelberg, 2008.

(7) Luo, Z.; Khanna, S. N., *Metal clusters and their reactivity*; Springer: Singapore, 2020, %5Curl%7Bhttps://ebookcentral.proquest.com/lib/kxp/detail.action?docID=6382727%7D.

(8) Di Bartolo, B., *Spectroscopy and Dynamics of Collective Excitations in Solids*; Nato Science Series B, Vol. v.356; Springer: New York, NY, 1997, %5Curl%7Bhttps://ebookcentral.proquest.com/lib/kxp/detail.action?docID=6497910%7D.

(9) Bohren, C. F.; Huffman, D. R., *Absorption and scattering of light by small particles*; Wiley-VCH: Weinheim, 2007, %5Curl%7Bhttp://onlinelibrary.wiley.com/book/10.1002/9783527618156%7D.

(10) Zhang, J.; Zhang, L. *Advances in Optics and Photonics* **2012**, *4*, 157.

(11) Zhang, J.; Zhang, L.; Xu, W. *Journal of Physics D: Applied Physics* **2012**, *45*, 113001.

(12) Kreibig, U.; Vollmer, M., *Optical Properties of Metal Clusters*; Springer Berlin Heidelberg: Berlin, Heidelberg, 1995; Vol. 25.

(13) Mie, G. *Annalen der Physik* **1908**, *330*, 377–445.

(14) Gans, R. *Annalen der Physik* **1912**, *342*, 881–900.

(15) Myroshnychenko, V.; Rodríguez-Fernández, J.; Pastoriza-Santos, I.; Funston, A. M.; Novo, C.; Mulvaney, P.; Liz-Marzán, L. M.; García de Abajo, F. J. *Chemical Society reviews* **2008**, *37*, 1792–1805.

(16) Yu, R.; Liz-Marzán, L. M.; García de Abajo, F. J. *Chemical Society reviews* **2017**, *46*, 6710–6724.

(17) Amendola, V.; Pilot, R.; Frasconi, M.; Maragò, O. M.; Iatì, M. A. *J. Phys.: Condens. Matter* **2017**, *29*, 203002.

(18) Link, S.; el-Sayed, M. A. *Int. Rev. Phys. Chem.* **2000**, *19*, 409–453.

(19) *Colloidal synthesis of plasmonic nanometals*; Liz-Marzán, L. M., Ed.; Jenny Stanford Publishing Pte. Ltd: Singapore, 2020.

(20) Allenmark, S. *Chirality* **2003**, *15*, 409–422.

(21) Gautier, C.; Bürgi, T. *Chemphyschem : a European journal of chemical physics and physical chemistry* **2009**, *10*, 483–492.

(22) Jakob, M.; von Weber, A.; Kartouzian, A.; Heiz, U. *Phys. Chem. Chem. Phys.* **2018**, *20*, 20347–20351.

(23) Maoz, B. M.; Chaikin, Y.; Tesler, A. B.; Bar Elli, O.; Fan, Z.; Govorov, A. O.; Markovich, G. *Nano letters* **2013**, *13*, 1203–1209.

(24) Ben-Moshe, A.; Maoz, B. M.; Govorov, A. O.; Markovich, G. *Chemical Society reviews* **2013**, *42*, 7028–7041.

(25) Fan, Z.; Govorov, A. O. *Nano letters* **2010**, *10*, 2580–2587.

(26) Govorov, A. O. *The Journal of Physical Chemistry C* **2011**, *115*, 7914–7923.

(27) Govorov, A. O.; Fan, Z.; Hernandez, P.; Slocik, J. M.; Naik, R. R. *Nano letters* **2010**, *10*, 1374–1382.

(28) Gautier, C.; Bürgi, T. *CHIMIA* **2008**, *62*, 465–470.

(29) Amabilino, D. B., *Chirality at the Nanoscale: Nanoparticles, surfaces, materials and more*; Wiley-VCH: Weinheim, 2009, `%5Curl%7Bhttp://site.ebrary.com/lib/alltitles/docDetail.action?docID=10301773%7D`.

(30) Jenkins, S. J., *Chirality at solid surfaces*; John Wiley & Sons: Hoboken, NJ, 2018.

(31) Auguié, B.; Alonso-Gómez, J. L.; Guerrero-Martínez, A.; Liz-Marzán, L. M. *The journal of physical chemistry letters* **2011**, *2*, 846–851.

(32) Guerrero-Martínez, A.; Auguié, B.; Alonso-Gómez, J. L.; Džolić, Z.; Gómez-Graña, S.; Žinić, M.; Cid, M. M.; Liz-Marzán, L. M. *Angewandte Chemie (International ed. in English)* **2011**, *50*, 5499–5503.

(33) Chen, S.; Reineke, B.; Li, G.; Zentgraf, T.; Zhang, S. *Nano Letters* **2019**, *19*, 6278–6283.

(34) Chen, Y.; Chen, W.; Kong, X.; Wu, D.; Chu, J.; Qiu, C.-W. *Phys. Rev. Lett.* **2022**, *128*, 146102.

(35) Collins, J. T.; Hooper, D. C.; Mark, A. G.; Kuppe, C.; Valev, V. K. *ACS nano* **2018**, *12*, 5445–5451.

(36) TUOVINEN, H.; Kauranen, M.; JEFIMOVS, K.; VAHIMAA, P.; VALLIUS, T.; TURUNEN, J.; TKACHENKO, N. V.; LEMMETYINEN, H. *J. Nonlinear Optic. Phys. Mat.* **2002**, *11*, 421–432.

(37) Yao, K.; Zheng, Y. *The Journal of Physical Chemistry C* **2019**, *123*, 11814–11822.

(38) Yashima, E.; Ousaka, N.; Taura, D.; Shimomura, K.; Ikai, T.; Maeda, K. *Chemical reviews* **2016**, *116*, 13752–13990.

(39) Ben-Moshe, A.; Teitelboim, A.; Oron, D.; Markovich, G. *Nano letters* **2016**, *16*, 7467–7473.

(40) Desmarchelier, A.; Caumes, X.; Raynal, M.; Vidal-Ferran, A.; van Leeuwen, P. W. N. M.; Bouteiller, L. *Journal of the American Chemical Society* **2016**, *138*, 4908–4916.

(41) Kunz, S. *Topics in Catalysis* **2016**, *59*, 1671–1685.

(42) Hollas, J. M., *Modern spectroscopy*, 4. ed., reprinted.; Wiley: Chichester, 2010, %5Curl%7Bhttp://bvbr.bib-bvb.de:8991/F?func=service&doc_library=BVB01&doc_number=020495566&line_number=0002&func_code=DB_RECORDS&service_type=MEDIA%7D.

(43) Parson, W. W., *Modern optical spectroscopy: With exercises and examples from biophysics and biochemistry*, 2. ed.; Springer: Berlin and Heidelberg, 2015.

(44) Wagnière, G. H., *On Chirality and the Universal Asymmetry*; Wiley-VCH: Hoboken, 2008, %5Curl%7Bhttp://search.ebscohost.com/login.aspx?direct=true&scope=site&db=nlebk&db=nlabk&AN=246597%7D.

(45) *Circular dichroism: Principles and applications*; Nakanishi, K., Berova, N., Woody, R. W., Eds.; VCH: New York, NY, 1994.

(46) Albano, G.; Pescitelli, G.; Di Bari, L. *ChemNanoMat* **2022**, *8*, DOI: \url{10.1002/cnma.202200219}.

(47) Shindo, Y. *Optical Engineering* **1995**, *34*, 3369.

(48) Kuroda, R.; Harada, T.; Shindo, Y. *Optical Engineering* **2001**, *72*, 3802–3810.

(49) Von Weber, A.; Hooper, D. C.; Jakob, M.; Valev, V. K.; Kartouzian, A.; Heiz, U. *Chemphyschem : a European journal of chemical physics and physical chemistry* **2019**, *20*, 62–69.

(50) Lakhwani, G.; Meskers, S. C. J.; Janssen, R. A. J. *The journal of physical chemistry. B* **2007**, *111*, 5124–5131.

(51) Crassous, J.; Amon, A.; Crassous, J. *Phys. Rev. A* **2012**, *85*, DOI: \url{10.1103/PhysRevA.85.023806}.

(52) Bustamante, C.; Tinoco, I.; Maestre, M. F. *Proceedings of the National Academy of Sciences of the United States of America* **1983**, *80*, 3568–3572.

(53) Phillips, C. L.; Mickols, W. E.; Maestre, M. F.; Tinoco, I. *Biochemistry* **1986**, *25*, 7803–7811.

(54) Wang, L.-Y.; Smith, K. W.; Dominguez-Medina, S.; Moody, N.; Olson, J. M.; Zhang, H.; Chang, W.-S.; Kotov, N.; Link, S. *ACS Photonics* **2015**, *2*, 1602–1610.

(55) Keller, D.; Bustamante, C. *The Journal of Chemical Physics* **1986**, *84*, 2972–2980.

(56) Shen, Y. R., *Fundamentals of Sum-Frequency Spectroscopy*; Cambridge University Press: Cambridge, 2016.

(57) Boyd, R. W., *Nonlinear Optics*, Fourth edition; Elsevier AP Academic Press: London, 2020, %5Curl%7Bhttps://www.sciencedirect.com/science/book/9780128110027%7D.

(58) Kartouzian, A.; Heister, P.; Heiz, U.; Thämer, M.; Gerlach, S. *J. Opt. Soc. Am. B* **2013**, *30*, 541.

(59) Brevet, P.-F., *Surface second harmonic generation*; Cahies de chimie; Presses polytechniques et universitaires romandes: Lausanne, 1997.

(60) Petralli-Mallow, T.; Wong, T. M.; d. Byers, J.; Yee, H. I.; Hicks, J. M. *J. Phys. Chem.* **1993**, *97*, 1383–1388.

(61) D. Byers, J.; Hicks, J. M. *Chemical Physics Letters* **1994**, *231*, 216–224.

(62) D. Byers, J.; Yee, H. I.; Hicks, J. M. *The Journal of Chemical Physics* **1994**, *101*, 6233–6241.

(63) Byers; Yee; Petralli-Mallow; Hicks *Physical review. B, Condensed matter* **1994**, *49*, 14643–14647.

(64) Persechini, L.; McGilp, J. F. *physica status solidi (b)* **2012**, *249*, 1155–1159.

(65) Persechini, L.; McGilp, J. F. *physica status solidi (b)* **2015**, *252*, 95–99.

(66) Von Weber, A.; Jakob, M.; Kratzer, E.; Kartouzian, A.; Heiz, U. *ChemPhysChem* **2019**, *20*, 134–141.

(67) Heister, P.; Lünskens, T.; Thämer, M.; Kartouzian, A.; Gerlach, S.; Verbiest, T.; Heiz, U. *Physical chemistry chemical physics : PCCP* **2014**, *16*, 7299–7306.

(68) Lopatynskyi, A. M.; Lytvyn, V. K.; Nazarenko, V. I.; Guo, L. J.; Lucas, B. D.; Chegel, V. I. *Nanoscale research letters* **2015**, *10*, 99.

(69) Chegel, V. I.; Naum, O. M.; Lopatynskyi, A. M.; Lytvyn, V. K. In *Nanoplasmonics, Nano-Optics, Nanocomposites, and Surface Studies*, Fesenko, O., Ed.; Springer Proceedings in Physics Ser, Vol. 167; Springer International Publishing AG: Cham, 2015, pp 395–412.

(70) Fehn, N.; Vahidzadeh, E.; Shankar, K.; Heiz, U.; Kartouzian, A. *Applied Surface Science* **2022**, *581*, 152381.

(71) Vahidzadeh, E.; Zeng, S.; Alam, K. M.; Kumar, P.; Riddell, S.; Chaulagain, N.; Gusarov, S.; Kobryn, A. E.; Shankar, K. *ACS Appl. Mater. Interfaces* **2021**, *13*, 42741–42752.

(72) Vahidzadeh, E.; Zeng, S.; Manuel, A. P.; Riddell, S.; Kumar, P.; Alam, K. M.; Shankar, K. *ACS Appl. Mater. Interfaces* **2021**, *13*, 7248–7258.

(73) Golibrzuch, M.; Maier, T. L.; Feil, M. J.; Krischer, K.; Becherer, M. *Journal of Applied Physics* **2022**, *131*, 124301.

(74) Kuroda, R.; Mason, S. F. *J. Chem. Soc., Perkin Trans. 2* **1981**, 167–170.

(75) Moggach, S. A.; Allan, D. R.; Parsons, S.; Sawyer, L.; Warren, J. E. *Journal of synchrotron radiation* **2005**, *12*, 598–607.

(76) Reddy, N. L.; Rao, V. N.; Vijayakumar, M.; Santhosh, R.; Anandan, S.; Karthik, M.; Shankar, M. V.; Reddy, K. R.; Shetti, N. P.; Nadagouda, M. N.; Aminabhavi, T. M. *Int. J. Hydrogen Energy* **2019**, *44*, 10453–10472.

(77) Zeng, S.; Vahidzadeh, E.; VanEssen, C. G.; Kar, P.; Kisslinger, R.; Goswami, A.; Zhang, Y.; Mahdi, N.; Riddell, S.; Kobryn, A. E.; Gusarov, S.; Kumar, P.; Shankar, K. *Appl. Catal. B* **2020**, *267*, 118644.

(78) Eder, M.; Courtois, C.; Kratky, T.; Günther, S.; Tschurl, M.; Heiz, U. *Catalysis Science & Technology* **2020**, *10*, 7630–7639.

(79) Manuel, A. P.; Shankar, K. *Nanomaterials* **2021**, *11*, 1249.

(80) Otor, H. O.; Steiner, J. B.; García-Sancho, C.; Alba-Rubio, A. C. *ACS Catal.* **2020**, *10*, 7630–7656.

(81) Wang, C.; Wang, H.; Yao, Q.; Yan, H.; Li, J.; Lu, J. *J. Phys. Chem. C* **2016**, *120*, 478–486.

(82) Chervinskii, S.; Koskinen, K.; Scherbak, S.; Kauranen, M.; Lipovskii, A. *Phys. Rev. Lett.* **2018**, *120*, 113902.

(83) Pensa, E.; Cortés, E.; Corthey, G.; Carro, P.; Vericat, C.; Fonticelli, M. H.; Benítez, G.; Rubert, A. A.; Salvarezza, R. C. *Acc. Chem. Res.* **2012**, *45*, 1183–1192.

(84) Liu, H.; Li, Z.; Yan, Y.; Zhao, J.; Wang, Y. *Nanoscale* **2019**, *11*, 21990–21998.

(85) Jing, C.; Fang, Y. *Chemical Physics* **2007**, *332*, 27–32.

(86) Longo, E.; Orlandin, A.; Mancin, F.; Scrimin, P.; Moretto, A. *ACS nano* **2013**, *7*, 9933–9939.

(87) Gautier, C.; Bürgi, T. *Journal of the American Chemical Society* **2008**, *130*, 7077–7084.

(88) Bergquist, L.; Hegmann, T. *ChemNanoMat* **2017**, *3*, 863–868.

(89) Acres, R. G.; Feyer, V.; Tsud, N.; Carlino, E.; Prince, K. C. *The Journal of Physical Chemistry C* **2014**, *118*, 10481–10487.

(90) Kühnle, A.; Linderoth, T. R.; Besenbacher, F. *Journal of the American Chemical Society* **2003**, *125*, 14680–14681.

(91) Chapman, C. R. L.; Ting, E. C.; Kereszti, A.; Paci, I. *The Journal of Physical Chemistry C* **2013**, *117*, 19426–19435.

(92) Santos, E.; Avalle, L.; Pötting, K.; Vélez, P.; Jones, H. *Electrochimica Acta* **2008**, *53*, 6807–6817.

(93) Fischer, S.; Papageorgiou, A. C.; Marschall, M.; Reichert, J.; Diller, K.; Klappenberger, F.; Allegretti, F.; Nefedov, A.; Wöll, C.; Barth, J. V. *The Journal of Physical Chemistry C* **2012**, *116*, 20356–20362.

(94) Maul, R.; Preuss, M.; Ortmann, F.; Hannewald, K.; Bechstedt, F. *The journal of physical chemistry. A* **2007**, *111*, 4370–4377.

(95) Dobrowolski, J. C.; Rode, J. E.; Sadlej, J. *Journal of Molecular Structure: THEOCHEM* **2007**, *810*, 129–134.

(96) Kamada, M.; Hideshima, T.; Azuma, J.; Yamamoto, I.; Imamura, M.; Takahashi, K. *AIP Advances* **2016**, *6*, 045306.

(97) Kamada, M.; Hideshima, T.; Azuma, J.; Yamamoto, I.; Imamura, M.; Takahashi, K. *J. Phys. Soc. Jpn.* **2016**, *85*, 124713.

(98) Kamada, M.; Sugiyama, H.; Takahashi, K.; Azuma, J.; Kitajima, S.; Ogawa, K.; Sumimoto, M.; Hori, K.; Fujimoto, H. *J. Phys. Soc. Jpn.* **2010**, *79*, 034709.

(99) Fajín, J. L. C.; Gomes, J. R. B.; Cordeiro, M. N. D. S. *Langmuir* **2013**, *29*, 8856–8864.

(100) Noyori, R.; Takaya, H. *Acc. Chem. Res.* **1990**, *23*, 345–350.

(101) Zhang, W.; Chi, Y.; Zhang, X. *Acc. Chem. Res.* **2007**, *40*, 1278–1290.

(102) Sodeoka, M.; Tokunoh, R.; Miyazaki, F.; Hagiwara, E.; Shibasaki, M. *Synlett* **1997**, *1997*, 463–466.

(103) Eustis, S.; el-Sayed, M. A. *Chem. Soc. Rev.* **2006**, *35*, 209–217.

(104) Liz-Marzán, L. M. *Langmuir* **2006**, *22*, 32–41.

(105) Gargiulo, J.; Berté, R.; Li, Y.; Maier, S. A.; Cortés, E. *Acc. Chem. Res.* **2019**, *52*, 2525–2535.

(106) Cortés, E. *Science* **2018**, *362*, 28–29.

(107) Yu, H.; Peng, Y.; Yang, Y.; Li, Z.-Y. *npj Comput Mater* **2019**, *5*, DOI: `\url{10.1038/s41524-019-0184-1}`.

(108) Schomaker, S.; Holze, R. *Zeitschrift für Physikalische Chemie* **1994**, *185*, 17–32.

(109) González-Rubio, G.; Mosquera, J.; Kumar, V.; Pedrazo-Tardajos, A.; Llombart, P.; Solís, D. M.; Lobato, I.; Noya, E. G.; Guerrero-Martínez, A.; Taboada, J. M.; Obelleiro, F.; MacDowell, L. G.; Bals, S.; Liz-Marzán, L. M. *Science* **2020**, *368*, 1472–1477.

(110) Heyvaert, W.; Pedrazo-Tardajos, A.; Kadu, A.; Claes, N.; González-Rubio, G.; Liz-Marzán, L. M.; Albrecht, W.; Bals, S. *ACS materials letters* **2022**, *4*, 642–649.

(111) Kühnle, A.; Molina, L. M.; Linderoth, T. R.; Hammer, B.; Besenbacher, F. *Physical review letters* **2004**, *93*, 086101.

(112) Bürgi, T. *Nanoscale* **2015**, *7*, 15553–15567.

(113) Shao, X.; Zhang, T.; Li, B.; Zhou, M.; Ma, X.; Wang, J.; Jiang, S. *Inorganic chemistry* **2019**, *58*, 6534–6543.

(114) Russier-Antoine, I.; Bertorelle, F.; Kulesza, A.; Soleilhac, A.; Bensalah-Ledoux, A.; Guy, S.; Dugourd, P.; Brevet, P.-F.; Antoine, R. *Prog. Nat. Sci.: Mater. Int.* **2016**, *26*, 455–460.

(115) Farrag, M.; Tschurl, M.; Heiz, U. *Chemistry of Materials* **2013**, *25*, 862–870.

(116) Liu, H.; Li, Z.; Yan, Y.; Zhao, J.; Wang, Y. *Particle & Particle Systems Characterization* **2020**, *37*, 1900338.

(117) Morales-Vidal, J.; López, N.; Ortuño, M. A. *The Journal of Physical Chemistry C* **2019**, *123*, 13758–13764.

(118) Franz, M.; Fischer, B. M.; Walther, M. *Journal of Molecular Structure* **2011**, *1006*, 34–40.

(119) Scherbak, S.; Kapralov, N.; Reduto, I.; Chervinskii, S.; Svirko, O.; Lipovskii, A. *Plasmonics* **2017**, *12*, 1903–1910.

(120) Schott AG Data Sheet N-BK7, 2014, `%5Curl%7Bhttps://www.schott.com/shop/advanced-optics/en/Optical-Glass/SCHOTT-N-BK7/c/glass-SCHOTT%20N-BK7%C2%AE%7D` (accessed 02/27/2023).

(121) Chen, V. Chiroptical characteristics of organic thin films prepared by spin-coating and evaporation, Bachelor's Thesis, München: Technische Universität München, 2022.

(122) Brandt, V. K. Induced Circular Dichroism in Dyes and Nanoparticles, Master's Thesis, München: Technische Universität München, 2022.

(123) Petzoldt, P.; Eder, M.; Mackewicz, S.; Blum, M.; Kratky, T.; Günther, S.; Tschurl, M.; Heiz, U.; Lechner, B. A. J. *J. Phys. Chem. C* **2022**, *126*, 16127–16139.

(124) Kaiser, S.; Maleki, F.; Zhang, K.; Harbich, W.; Heiz, U.; Tosoni, S.; Lechner, B. A. J.; Pacchioni, G.; Esch, F. *ACS Catal.* **2021**, *11*, 9519–9529.

(125) Luo, Z.; Zhao, G.; Pan, H.; Sun, W. *Advanced Energy Materials* **2022**, *12*, 2201395.

(126) Urata, H.; Suzuki, H.; Moro-oka, Y.; Ikawa, T. *J. Organomet. Chem.* **1989**, *364*, 235–244.

(127) Lindlar, H. *Helv. Chim. Acta* **1952**, *35*, 446–450.

(128) Tietze, L. F.; Ila, H.; Bell, H. P. *Appl. Phys. Lett.* **2004**, *104*, 3453–3516.

(129) Kiso, Y.; Yamamoto, K.; Tamao, K.; Kumada, M. *J. Am. Chem. Soc.* **1972**, *94*, 4373–4374.

(130) Chen, Q.-A.; Ye, Z.-S.; Duan, Y.; Zhou, Y.-G. *Chem. Soc. Rev.* **2013**, *42*, 497–511.

(131) Yamamoto, S.; Matsui, H.; Okajima, T.; Karuppuchamy, S.; Yoshihara, M. *Solid State Commun.* **2008**, *148*, 274–278.

(132) Véron, A. C.; Felber, M.; Blacque, O.; Spingler, B. *Polyhedron* **2013**, *52*, 102–105.

(133) Alcazar-Roman, L. M.; Hartwig, J. F.; Rheingold, A. L.; Liable-Sands, L. M.; Guzei, I. A. *J. Am. Chem. Soc.* **2000**, *122*, 4618–4630.

(134) Gnad, C.; Dachwald, O.; Raudaschl-Sieber, G.; Köhler, K. *J. Catal.* **2019**, *375*, 257–266.

(135) Zhao, C.-Q.; Han, L.-B.; Tanaka, M. *Organometallics* **2000**, *19*, 4196–4198.

(136) Fehn, N.; Strauss, M.; Jandl, C.; Drees, M.; Heiz, U.; Köhler, K.; Kartouzian, A. *New J. Chem., accepted* **2023**.

(137) Strauss, M. Synthese, Struktur und Eigenschaften von Oxid-geträgerten chiralen Palladium-Katalysatoren: Synthesis, Structure and Properties of Oxide Supported Chiral Palladium Catalysts, Masterarbeit, München: Technische Universität München, 2019.

(138) Di Bari, L.; Pescitelli, G.; Salvadori, P. *Journal of the American Chemical Society* **1999**, *121*, 7998–8004.

(139) Górecki, M.; Capozzi, M. A. M.; Albano, G.; Cardellicchio, C.; Di Bari, L.; Pescitelli, G. *Chirality* **2018**, *30*, 29–42.

(140) Torabi Kohlbouni, S.; Sarkar, A.; Zhang, J.; Li, X.; Borhan, B. *Chirality* **2020**, *32*, 817–823.

(141) Tedesco, D.; Bertucci, C. *Journal of Pharmaceutical and Biomedical Analysis* **2015**, *113*, 34–42.

(142) Zhang, L.; Wang, T.; Shen, Z.; Liu, M. *Advanced materials (Deerfield Beach, Fla.)* **2016**, *28*, 1044–1059.

(143) Rajora, M. A.; Lou, J. W. H.; Zheng, G. *Chemical Society reviews* **2017**, *46*, 6433–6469.

(144) Kim, Y.; Kim, H.; Yang, Y.; Badloe, T.; Jeon, N.; Rho, J. *Nanoscale* **2022**, *14*, 3720–3730.

(145) Albano, G.; Pescitelli, G.; Di Bari, L. *Chemical reviews* **2020**, *120*, 10145–10243.

(146) Xue, Y.; Fehn, N.; Brandt, V. K.; Stasi, M.; Boekhoven, J.; Heiz, U.; Kartouzian, A. *Chirality* **2022**, *34*, 550–558.

(147) Von Weber, A.; Stanley, P.; Jakob, M.; Kartouzian, A.; Heiz, U. *J. Phys. Chem. C* **2019**, *123*, 9255–9261.

(148) Tyona, M. D. *Advances in materials Research* **2013**, *2*, 195–208.

(149) Chen, C.; Gao, L.; Gao, W.; Ge, C.; Du, X.; Li, Z.; Yang, Y.; Niu, G.; Tang, J. *Nature communications* **2019**, *10*, 1927.

(150) Di Nuzzo, D.; Cui, L.; Greenfield, J. L.; Zhao, B.; Friend, R. H.; Meskers, S. C. J. *ACS nano* **2020**, *14*, 7610–7616.

(151) Long, G.; Jiang, C.; Sabatini, R.; Yang, Z.; Wei, M.; Quan, L. N.; Liang, Q.; Rasmita, A.; Askerka, M.; Walters, G.; Gong, X.; Xing, J.; Wen, X.; Quintero-Bermudez, R.; Yuan, H.; Xing, G.; Wang, X. R.; Song, D.; Voznyy, O.; Zhang, M.; Hoogland, S.; Gao, W.; Xiong, Q.; Sargent, E. H. *Nature Photonics* **2018**, *12*, 528–533.

(152) Lu, H.; Wang, J.; Xiao, C.; Pan, X.; Chen, X.; Brunecky, R.; Berry, J. J.; Zhu, K.; Beard, M. C.; Vardeny, Z. V. *Science advances* **2019**, *5*, eaay0571.

(153) Kim, Y.-H.; Zhai, Y.; Lu, H.; Pan, X.; Xiao, C.; Gaulding, E. A.; Harvey, S. P.; Berry, J. J.; Vardeny, Z. V.; Luther, J. M.; Beard, M. C. *Science (New York, N.Y.)* **2021**, *371*, 1129–1133.

(154) Wei, Q.; Ning, Z. *ACS Materials Letters* **2021**, *3*, 1266–1275.

(155) Ma, J.; Wang, H.; Li, D. *Advanced materials (Deerfield Beach, Fla.)* **2021**, *33*, e2008785.

(156) Long, G.; Sabatini, R.; Saidaminov, M. I.; Lakhwani, G.; Rasmita, A.; Liu, X.; Sargent, E. H.; Gao, W. *Nature Reviews Materials* **2020**, *5*, 423–439.

(157) Jana, M. K.; Song, R.; Liu, H.; Khanal, D. R.; Janke, S. M.; Zhao, R.; Liu, C.; Valy Vardeny, Z.; Blum, V.; Mitzi, D. B. *Nature communications* **2020**, *11*, 4699.

(158) Kim, Y.-H.; Zhai, Y.; Gaulding, E. A.; Habisreutinger, S. N.; Moot, T.; Rosales, B. A.; Lu, H.; Hazarika, A.; Brunecky, R.; Wheeler, L. M.; Berry, J. J.; Beard, M. C.; Luther, J. M. *ACS nano* **2020**, *14*, 8816–8825.

(159) Shi, Y.; Duan, P.; Huo, S.; Li, Y.; Liu, M. *Advanced materials (Deerfield Beach, Fla.)* **2018**, *30*, e1705011.

(160) Liu, S.; Heindl, M. W.; Fehn, N.; Caicedo-Dávila, S.; Eyre, L.; Kronawitter, S. M.; Zerhoch, J.; Bodnar, S.; Shcherbakov, A.; Stadlbauer, A.; Kieslich, G.; Sharp, I. D.; Egger, D. A.; Kartouzian, A.; Deschler, F. *J. Am. Chem. Soc.* **2022**, *144*, 14079–14089.

(161) Liu, S.; Kepenekian, M.; Bodnar, S.; Feldmann, S.; Heindl, M. W.; Fehn, N.; Zerhoch, J.; Shcherbakov, A.; Pöthig, A.; Kartouzian, A.; Sharp, I. D.; Katan, C.; Even, J.; Deschler, F. *Science Advances, submitted* **2023**.

(162) Heindl, M. W.; Kodalle, T.; Fehn, N.; Reb, L. K.; Liu, S.; Harder, C.; Abdelsamie, M.; Eyre, L.; Sharp, I. D.; Roth, S. V.; Müller–Buschbaum, P.; Kartouzian, A.; Sutter–Fella, C. M.; Deschler, F. *Adv. Opt. Mater.* **2022**, *10*, 2200204.

(163) Ristow, F.; Scheffel, J.; Xu, X.; Fehn, N.; Oberhofer, K. E.; Riemensberger, J.; Mortaheb, F.; Kienberger, R.; Heiz, U.; Kartouzian, A.; Iglev, H. *Chirality* **2020**, 1–12.

(164) Ristow, F.; Liang, K.; Pittrich, J.; Scheffel, J.; Fehn, N.; Kienberger, R.; Heiz, U.; Kartouzian, A.; Iglev, H. *J. Mater. Chem. C* **2022**, *10*, 12715–12723.

(165) Mortaheb, F.; Oberhofer, K.; Riemensberger, J.; Ristow, F.; Kienberger, R.; Heiz, U.; Iglev, H.; Kartouzian, A. *Angewandte Chemie (International ed. in English)* **2019**, *58*, 15685–15689.

A. Appendix

Additional Data

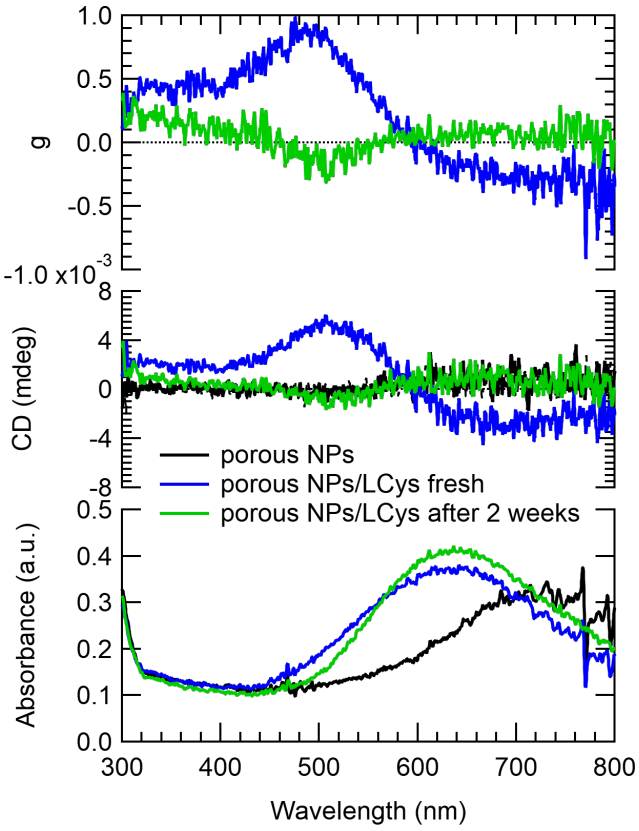

Figure A.1.: Absorbance and CD spectra of porous hemispherical Au NPs on BK7 with 30 nm (60 ML) L-Cysteine shortly after preparation and two weeks later.

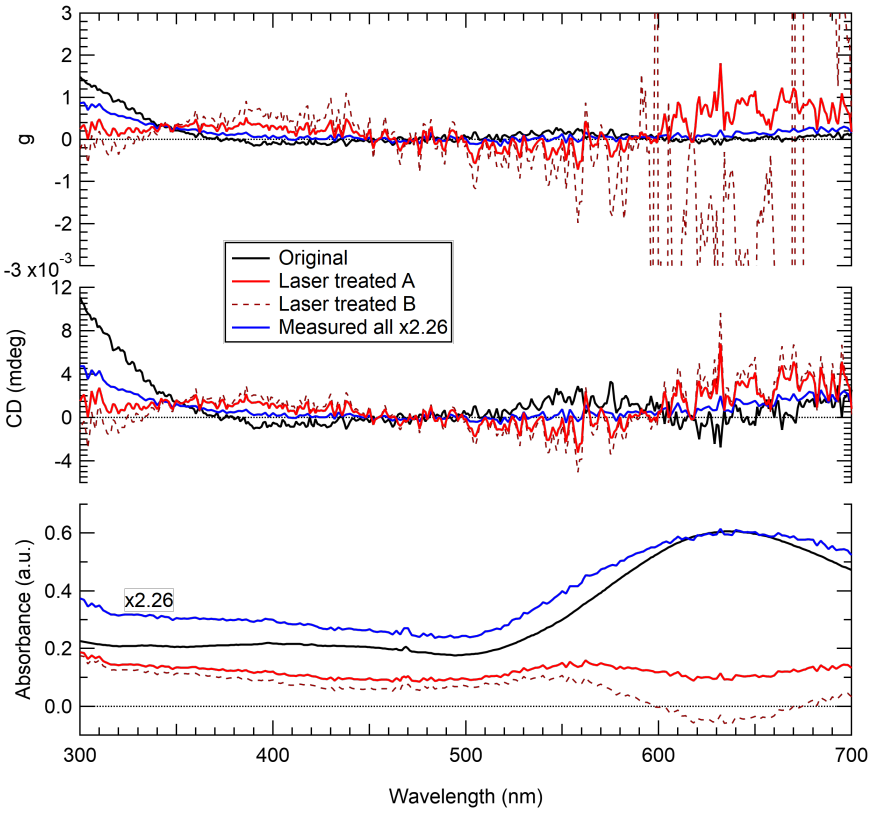

Figure A.2.: Absorbance and CD spectra of spherical Au NPs on borosilicate supports with L-Cysteine after laser treatment.

List of Samples

Table A.1.: Nanoparticles with chiral adsorbates and ICD

Composition Shape	Inducer	fundamental CD	SHG-CD	chapter
Au hemisphere	Binol	yes	no, laser damage	4.1
Au hemisphere	Cysteine	yes	ambiguous, symmetrisation	4.1,5.2
Au hemisphere/porous	Cysteine	yes	ambiguous, symmetrisation	5.2
Au cylinder	Binol	yes	yes	5.1
Au sphere	Cysteine	yes	ambiguous, laser damage	5.3
Au sphere	Thiols	yes	no, laser damage	-
$DMAPbI_3$ thin films	3-ABA	yes	no, laser damage	-
$CHEA_4Bi_2Br_xI_{10-x}$ thin films	CHEA	yes	no, laser damage	-

Table A.2.: Molecules and support materials

Compound	Formula	fundamental CD	SHG-CD	chapter
Allenes CF-3 to -5 1 ML on Ti/SiO_2	$C_{40}H_{29}NO_2S$	no, sensitivity	no, laser damage	-
Cysteine Multilayer on BS, FS	$C_3H_7NO_2S$	yes	yes	4.2
Binol Multilayer on BK7	$C_{20}H_{14}O_2$	yes	yes	3.3
Binol, SiO_2 coating Multilayer on BK7	$C_{20}H_{14}O_2 \cdot xSiO_2$	no, sensitivity	no, laser damage	-
Rhodamine:Binol Multilayer on BK7	$C_{20}H_{15}ClN_2O_3$ $\cdot xC_{20}H_{14}O_2$	yes	no, laser damage	-

List of Publications

- Fehn, N.; Vahidzadeh, E.; Shankar, K.; Heiz, U.; Kartouzian, A. Surface second harmonic generation spectra of titania coated Au NPs. *Appl. Surf. Sci.* **2022**, *581*, 152381. DOI: 10.1016/j.apsusc.2021.152381.

- Fehn, N.; Strauss, M.; Jandl, C.; Drees, M.; Heiz, U.; Köhler, K.; Kartouzian, A. On the nature of optical acitivity in chiral transition metal complexes: [Pd(Me2)BINAP]. *New J. Chem., accepted* **2023**.

- Xue, Y.; Fehn, N.; Brandt, V. K.; Stasi, M.; Boekhoven, J.; Heiz, U.; Kartouzian, A. Tunable induced circular dichroism in gels. *Chirality* **2022**. DOI: 10.1002/chir.23409.

- Heindl, M. W.; Kodalle, T.; Fehn, N.; Reb, L. K.; Liu, S.; Harder, C.; Abdelsamie, M.; Eyre, L.; Sharp, I. D.; Roth, S. V.; Muller-Buschbaum, P.; Kartouzian, A.; Sutter-Fella, C. M.; Deschler, F. Strong Induced Circular Dichroism in a Hybrid Lead-Halide Semiconductor Using Chiral Amino Acids for Crystallite Surface Functionalization. *Adv. Opt. Mater.* **2022**, *10* (14), 2200204. DOI: 10.1002/adom.202200204.

- Liu, S.; Heindl, M. W.; Fehn, N.; Caicedo-Dávila, S.; Eyre, L.; Kronawitter, S. M.; Zerhoch, J.; Bodnar, S.; Shcherbakov, A.; Stadlbauer, A.; Kieslich, G.; Sharp, I. D.; Egger, D. A.; Kartouzian, A.; Deschler, F. Optically Induced Long-Lived Chirality Memory in the Color-Tunable Chiral Lead-Free Semiconductor (R)/(S)-CHEA$_4$Bi$_2$BrxI$_{10-x}$ ($x = 0 - 10$). *J. Am. Chem. Soc.* **2022**, *144* (31), 14079–14089. DOI: 10.1021/jacs.2c01994.

- Liu, S.; Kepenekian, M.; Bodnar, S.; Feldmann, S.; Heindl, M. W.; Fehn, N.; Zerhoch, J.; Shcherbakov, A.; Pöthig, A.; Kartouzian, A.; Sharp, I. D.; Katan, C.; Even, J.; Deschler, F. Bright Room-Temperature Circularly-Polarized Photoluminescence in 2D Chiral Lead-Halide Perovskites. *Science, submitted* **2023**.

- Ristow, F.; Scheffel, J.; Xu, X.; Fehn, N.; Oberhofer, K. E.; Riemensberger, J.; Mortaheb, F.; Kienberger, R.; Heiz, U.; Kartouzian, A.; Iglev, H. Understanding laser desorption with circularly polarized light. *Chirality* **2020**, *1-12*. DOI: 10.1002/chir.23279.

- Ristow, F.; Liang, K.; Pittrich, J.; Scheffel, J.; Fehn, N.; Kienberger, R.; Heiz, U.; Kartouzian, A.; Iglev, H. Large-area SHG-CD probe intrinsic chirality in polycrystalline films. *J. Mater. Chem. C* **2022**, *10* (35), 12715-12723. DOI: 10.1039/D2TC01700H.

Print Permissions

AIP PUBLISHING LICENSE
TERMS AND CONDITIONS

Mar 10, 2023

This Agreement between Natalie Fehn ("You") and AIP Publishing ("AIP Publishing") consists of your license details and the terms and conditions provided by AIP Publishing and Copyright Clearance Center.

License Number	5505441393962
License date	Mar 10, 2023
Licensed Content Publisher	AIP Publishing
Licensed Content Publication	Journal of Applied Physics
Licensed Content Title	Tuning the feature size of nanoimprinting stamps: A method to enhance the flexibility of nanoimprint lithography
Licensed Content Author	Matthias Golibrzuch, Thomas L. Maier, Moritz J. Feil, et al
Licensed Content Date	Mar 28, 2022
Licensed Content Volume	131
Licensed Content Issue	12
Type of Use	Thesis/Dissertation
Requestor type	Student

Format	Print and electronic
Portion	Figure/Table
Number of figures/tables	1
Will you be translating?	No
Title	Linear and Nonlinear Chiroptical Spectroscopy with the Aim of Asymmetric Heterogeneous Catalysis
Institution name	PC1, School of Natural Sciences, Technical University Munich
Expected presentation date	Mar 2023
Portions	Figure 6
Requestor Location	Natalie Fehn Lichtenbergstr. 4 Lehrstuhl PC1 Garching bei München, 85748 Germany Attn: Natalie Fehn
Total	0.00 EUR

Terms and Conditions

AIP Publishing -- Terms and Conditions: Permissions Uses

AIP Publishing hereby grants to you the non-exclusive right and license to use and/or distribute the Material according to the use specified in your order, on a one-time basis, for the specified term, with a maximum distribution equal to the number that you have ordered. Any links or other content accompanying the Material are not the subject of this license.

1. You agree to include the following copyright and permission notice with the reproduction of the Material:"Reprinted from [FULL CITATION], with the permission of AIP Publishing." For an article, the credit line and permission notice must be

printed on the first page of the article or book chapter. For photographs, covers, or tables, the notice may appear with the Material, in a footnote, or in the reference list.

2. If you have licensed reuse of a figure, photograph, cover, or table, it is your responsibility to ensure that the material is original to AIP Publishing and does not contain the copyright of another entity, and that the copyright notice of the figure, photograph, cover, or table does not indicate that it was reprinted by AIP Publishing, with permission, from another source. Under no circumstances does AIP Publishing purport or intend to grant permission to reuse material to which it does not hold appropriate rights.
   You may not alter or modify the Material in any manner. You may translate the Material into another language only if you have licensed translation rights. You may not use the Material for promotional purposes.
3. The foregoing license shall not take effect unless and until AIP Publishing or its agent, Copyright Clearance Center, receives the Payment in accordance with Copyright Clearance Center Billing and Payment Terms and Conditions, which are incorporated herein by reference.
4. AIP Publishing or Copyright Clearance Center may, within two business days of granting this license, revoke the license for any reason whatsoever, with a full refund payable to you. Should you violate the terms of this license at any time, AIP Publishing, or Copyright Clearance Center may revoke the license with no refund to you. Notice of such revocation will be made using the contact information provided by you. Failure to receive such notice will not nullify the revocation.
5. AIP Publishing makes no representations or warranties with respect to the Material. You agree to indemnify and hold harmless AIP Publishing, and their officers, directors, employees or agents from and against any and all claims arising out of your use of the Material other than as specifically authorized herein.
6. The permission granted herein is personal to you and is not transferable or assignable without the prior written permission of AIP Publishing. This license may not be amended except in a writing signed by the party to be charged.
7. If purchase orders, acknowledgments or check endorsements are issued on any forms containing terms and conditions which are inconsistent with these provisions, such inconsistent terms and conditions shall be of no force and effect. This document, including the CCC Billing and Payment Terms and Conditions, shall be the entire agreement between the parties relating to the subject matter hereof.

This Agreement shall be governed by and construed in accordance with the laws of the State of New York. Both parties hereby submit to the jurisdiction of the courts of New York County for purposes of resolving any disputes that may arise hereunder.

V1.2

Questions? customercare@copyright.com.

JOHN WILEY AND SONS LICENSE
TERMS AND CONDITIONS

Mar 10, 2023

This Agreement between Natalie Fehn ("You") and John Wiley and Sons ("John Wiley and Sons") consists of your license details and the terms and conditions provided by John Wiley and Sons and Copyright Clearance Center.

License Number	5505450397799
License date	Mar 10, 2023
Licensed Content Publisher	John Wiley and Sons
Licensed Content Publication	ChemPhysChem
Licensed Content Title	In situ Second-Harmonic Generation Circular Dichroism with Submonolayer Sensitivity
Licensed Content Author	Ueli Heiz, Aras Kartouzian, Eva Kratzer, et al
Licensed Content Date	Nov 30, 2018
Licensed Content Volume	20
Licensed Content Issue	1
Licensed Content Pages	8
Type of use	Dissertation/Thesis

Requestor type	University/Academic
Format	Print and electronic
Portion	Figure/table
Number of figures/tables	1
Will you be translating?	No
Title	Linear and Nonlinear Chiroptical Spectroscopy with the Aim of Asymmetric Heterogeneous Catalysis
Institution name	PC1, School of Natural Sciences, Technical University Munich
Expected presentation date	Mar 2023
Portions	Figure 1
Requestor Location	Natalie Fehn Lichtenbergstr. 4 Lehrstuhl PC1 Garching bei München, 85748 Germany Attn: Natalie Fehn
Publisher Tax ID	EU826007151
Total	0.00 EUR
Terms and Conditions	

TERMS AND CONDITIONS

This copyrighted material is owned by or exclusively licensed to John Wiley & Sons, Inc. or one of its group companies (each a"Wiley Company") or handled on behalf of a society with

which a Wiley Company has exclusive publishing rights in relation to a particular work (collectively "WILEY"). By clicking "accept" in connection with completing this licensing transaction, you agree that the following terms and conditions apply to this transaction (along with the billing and payment terms and conditions established by the Copyright Clearance Center Inc., ("CCC's Billing and Payment terms and conditions"), at the time that you opened your RightsLink account (these are available at any time at http://myaccount.copyright.com).

Terms and Conditions

- The materials you have requested permission to reproduce or reuse (the "Wiley Materials") are protected by copyright.
- You are hereby granted a personal, non-exclusive, non-sub licensable (on a stand-alone basis), non-transferable, worldwide, limited license to reproduce the Wiley Materials for the purpose specified in the licensing process. This license, **and any CONTENT (PDF or image file) purchased as part of your order,** is for a one-time use only and limited to any maximum distribution number specified in the license. The first instance of republication or reuse granted by this license must be completed within two years of the date of the grant of this license (although copies prepared before the end date may be distributed thereafter). The Wiley Materials shall not be used in any other manner or for any other purpose, beyond what is granted in the license. Permission is granted subject to an appropriate acknowledgement given to the author, title of the material/book/journal and the publisher. You shall also duplicate the copyright notice that appears in the Wiley publication in your use of the Wiley Material. Permission is also granted on the understanding that nowhere in the text is a previously published source acknowledged for all or part of this Wiley Material. Any third party content is expressly excluded from this permission.
- With respect to the Wiley Materials, all rights are reserved. Except as expressly granted by the terms of the license, no part of the Wiley Materials may be copied, modified, adapted (except for minor reformatting required by the new Publication), translated, reproduced, transferred or distributed, in any form or by any means, and no derivative works may be made based on the Wiley Materials without the prior permission of the respective copyright owner.**For STM Signatory Publishers clearing permission under the terms of the STM Permissions Guidelines only, the terms of the license are extended to include subsequent editions and for editions in other languages, provided such editions are for the work as a whole in situ and does not involve the separate exploitation of the permitted figures or extracts,** You may not alter, remove or suppress in any manner any copyright, trademark or other notices displayed by the Wiley Materials. You may not license, rent, sell, loan, lease, pledge, offer as security, transfer or assign the Wiley Materials on a stand-alone basis, or any of the rights granted to you hereunder to any other person.
- The Wiley Materials and all of the intellectual property rights therein shall at all times remain the exclusive property of John Wiley & Sons Inc, the Wiley Companies, or their respective licensors, and your interest therein is only that of having possession of and the right to reproduce the Wiley Materials pursuant to Section 2 herein during the continuance of this Agreement. You agree that you own no right, title or interest in or to the Wiley Materials or any of the intellectual property rights therein. You shall have

no rights hereunder other than the license as provided for above in Section 2. No right, license or interest to any trademark, trade name, service mark or other branding ("Marks") of WILEY or its licensors is granted hereunder, and you agree that you shall not assert any such right, license or interest with respect thereto

- NEITHER WILEY NOR ITS LICENSORS MAKES ANY WARRANTY OR REPRESENTATION OF ANY KIND TO YOU OR ANY THIRD PARTY, EXPRESS, IMPLIED OR STATUTORY, WITH RESPECT TO THE MATERIALS OR THE ACCURACY OF ANY INFORMATION CONTAINED IN THE MATERIALS, INCLUDING, WITHOUT LIMITATION, ANY IMPLIED WARRANTY OF MERCHANTABILITY, ACCURACY, SATISFACTORY QUALITY, FITNESS FOR A PARTICULAR PURPOSE, USABILITY, INTEGRATION OR NON-INFRINGEMENT AND ALL SUCH WARRANTIES ARE HEREBY EXCLUDED BY WILEY AND ITS LICENSORS AND WAIVED BY YOU.

- WILEY shall have the right to terminate this Agreement immediately upon breach of this Agreement by you.

- You shall indemnify, defend and hold harmless WILEY, its Licensors and their respective directors, officers, agents and employees, from and against any actual or threatened claims, demands, causes of action or proceedings arising from any breach of this Agreement by you.

- IN NO EVENT SHALL WILEY OR ITS LICENSORS BE LIABLE TO YOU OR ANY OTHER PARTY OR ANY OTHER PERSON OR ENTITY FOR ANY SPECIAL, CONSEQUENTIAL, INCIDENTAL, INDIRECT, EXEMPLARY OR PUNITIVE DAMAGES, HOWEVER CAUSED, ARISING OUT OF OR IN CONNECTION WITH THE DOWNLOADING, PROVISIONING, VIEWING OR USE OF THE MATERIALS REGARDLESS OF THE FORM OF ACTION, WHETHER FOR BREACH OF CONTRACT, BREACH OF WARRANTY, TORT, NEGLIGENCE, INFRINGEMENT OR OTHERWISE (INCLUDING, WITHOUT LIMITATION, DAMAGES BASED ON LOSS OF PROFITS, DATA, FILES, USE, BUSINESS OPPORTUNITY OR CLAIMS OF THIRD PARTIES), AND WHETHER OR NOT THE PARTY HAS BEEN ADVISED OF THE POSSIBILITY OF SUCH DAMAGES. THIS LIMITATION SHALL APPLY NOTWITHSTANDING ANY FAILURE OF ESSENTIAL PURPOSE OF ANY LIMITED REMEDY PROVIDED HEREIN.

- Should any provision of this Agreement be held by a court of competent jurisdiction to be illegal, invalid, or unenforceable, that provision shall be deemed amended to achieve as nearly as possible the same economic effect as the original provision, and the legality, validity and enforceability of the remaining provisions of this Agreement shall not be affected or impaired thereby.

- The failure of either party to enforce any term or condition of this Agreement shall not constitute a waiver of either party's right to enforce each and every term and condition of this Agreement. No breach under this agreement shall be deemed waived or excused by either party unless such waiver or consent is in writing signed by the party granting such waiver or consent. The waiver by or consent of a party to a breach of any provision of this Agreement shall not operate or be construed as a waiver of or

consent to any other or subsequent breach by such other party.

- This Agreement may not be assigned (including by operation of law or otherwise) by you without WILEY's prior written consent.
- Any fee required for this permission shall be non-refundable after thirty (30) days from receipt by the CCC.
- These terms and conditions together with CCC's Billing and Payment terms and conditions (which are incorporated herein) form the entire agreement between you and WILEY concerning this licensing transaction and (in the absence of fraud) supersedes all prior agreements and representations of the parties, oral or written. This Agreement may not be amended except in writing signed by both parties. This Agreement shall be binding upon and inure to the benefit of the parties' successors, legal representatives, and authorized assigns.
- In the event of any conflict between your obligations established by these terms and conditions and those established by CCC's Billing and Payment terms and conditions, these terms and conditions shall prevail.
- WILEY expressly reserves all rights not specifically granted in the combination of (i) the license details provided by you and accepted in the course of this licensing transaction, (ii) these terms and conditions and (iii) CCC's Billing and Payment terms and conditions.
- This Agreement will be void if the Type of Use, Format, Circulation, or Requestor Type was misrepresented during the licensing process.
- This Agreement shall be governed by and construed in accordance with the laws of the State of New York, USA, without regards to such state's conflict of law rules. Any legal action, suit or proceeding arising out of or relating to these Terms and Conditions or the breach thereof shall be instituted in a court of competent jurisdiction in New York County in the State of New York in the United States of America and each party hereby consents and submits to the personal jurisdiction of such court, waives any objection to venue in such court and consents to service of process by registered or certified mail, return receipt requested, at the last known address of such party.

WILEY OPEN ACCESS TERMS AND CONDITIONS

Wiley Publishes Open Access Articles in fully Open Access Journals and in Subscription journals offering Online Open. Although most of the fully Open Access journals publish open access articles under the terms of the Creative Commons Attribution (CC BY) License only, the subscription journals and a few of the Open Access Journals offer a choice of Creative Commons Licenses. The license type is clearly identified on the article.

The Creative Commons Attribution License

The Creative Commons Attribution License (CC-BY) allows users to copy, distribute and transmit an article, adapt the article and make commercial use of the article. The CC-BY license permits commercial and non-

Creative Commons Attribution Non-Commercial License

The Creative Commons Attribution Non-Commercial (CC-BY-NC)License permits use, distribution and reproduction in any medium, provided the original work is properly cited and is not used for commercial purposes.(see below)

Creative Commons Attribution-Non-Commercial-NoDerivs License

The Creative Commons Attribution Non-Commercial-NoDerivs License (CC-BY-NC-ND) permits use, distribution and reproduction in any medium, provided the original work is properly cited, is not used for commercial purposes and no modifications or adaptations are made. (see below)

Use by commercial "for-profit" organizations

Use of Wiley Open Access articles for commercial, promotional, or marketing purposes requires further explicit permission from Wiley and will be subject to a fee.

Further details can be found on Wiley Online Library http://olabout.wiley.com/WileyCDA/Section/id-410895.html

Other Terms and Conditions:

v1.10 Last updated September 2015

Questions? customercare@copyright.com.